Modeling of Complex Ionic Dissociation Reactions

Observed by TPEPICO Spectroscopy

William R. Stevens

A dissertation submitted to the faculty of the University of North Carolina at

Chapel Hill in partial fulfillment of the requirements for the degree

of Doctor of Philosophy in the Department of Chemistry.

Chapel Hill

2010

Approved by,

Dr. Tomas Baer
Dr. John Papanikolas
Dr. Max Berkowitz
Dr. Cynthia Schauer
Dr. Maurice Brookhart

ABSTRACT

WILLIAM R. STEVENS:

Modeling of Complex Ionic Dissociation Reactions Observed by TPEPICO Spectroscopy

(Under the direction of Prof. Tomas Baer)

TPEPICO spectra of dissociatively ionized chlorobenzene, bromobenzene, and iodobenzene have been measured to test the ability of different statistical rate theories to accurately calculate rate constants of homolytic bond cleavages of ions. For this purpose we have developed a method for extracting experimental rate constants at a single internal energy from TPEPICO spectra of thermal ions. It was determined that, of the theories tested, simplified versions of variational transition state theory (VTST) and statistical adiabatic channel model (SACM) were both capable of fitting the rate constants and predicting the known bond energies of all three halobenzenes. RRKM theory was capable of fitting the rate constants but predicted a bond energy that was too low. PST could neither fit the data nor predict the correct E_0. The much simpler to employ

simplified SACM (SSACM) was applied in the dissociations of nitrosobenzene and neopentane.

Chapter 1 is an introduction to the following chapters, dealing with the motivation to determine high precision bond energies of complex dissociations. Chapter 2 is a discussion of the experimental methods employed to observe photoionization and photodissociation processes. Chapter 3 describes the study of the simple isopropyl halide dissociation to determine the isopropyl ion heat of formation. In Chapter 4 we discuss the measurement of rate constants at specific ion internal energies for the dissociation of the halobenzenes in order to compare the ability of different rate theories to model homolytic bond cleavages. Chapters 5 and 6 are applications of the SSACM described in Chapter 4 to the dissociations of the nitrosobenzene and neopentane ions. Like the halobenzenes in chapter 4, the nitrosobenzene ion dissociation is slow and requires rate theories to determine the bond energy. The thermochemistry of the dissociation of both ionic and neutral dissociations of nitrosobenzene are improved using active thermochemical tables. In chapter 6 the bond energy for the methyl loss of neopentane is determined. Although this reaction occurs rapidly, there is a lower energy dissociation pathway that masks the methyl loss channel at threshold thus requiring extrapolation to determine the bond energy.

DEDICATION

This work is dedicated to my parents, Bruce and Janie Stevens, and to my wife, Vanessa Stevens; they have acted selflessly, as if by instinct, to provide me every opportunity possible.   My achievements are a direct result of your support**.**

ACKNOWLEDGEMENT

TABLE OF CONTENTS

LIST OF TABLES

LIST OF FIGURES

LIST OF ABBREVIATIONS

AE: Appearance Energy

BDE: Bond Dissociation Energy

IE: Ionization Energy

iPEPICO: Imaging Photoelectron-Photoion Coincidence

KE :   Kinetic Energy

MCP: Multichannel Plate

PA: Proton Affinity

PES: Photoelectron Spectroscopy

PIMS: Photoionization Mass Spectrometry

TOF: Time of Flight

TPEPICO: Threshold Photoelectron-Photoion Coincidence

VUV: Vacuum Ultraviolet

LIST OF SYMBOLS

$\Delta_f H$:   Heat of formation

E_0:   0 K Dissociation Onset measured relative to neutral ground state

E_{int}:   Ion Internal Energy measured relative to ion ground state

CHAPTER 1: Introduction

1.1 Motivation for studying complex dissociations

The current state of the art theoretical thermochemical methods such as HEAT[1] or W4[2] theory are able to reliably determine the energetics of smaller molecules to within 1 kJ•mol^{-1}. In order to produce relevant results and to help theoreticians improve their models, we must look to larger systems with heavier atoms. However, dissociations of interest from larger molecules tend to be more complex, *i.e.* they are more prone to dissociate at rates that are too slow to be measured and/or dissociate via multiple pathways at lower energies, both of which can shift the observed dissociation threshold to significantly higher energies. Additionally, large molecules with heavier atoms often have poorly defined heats of formation, which makes it difficult to derive reaction thermochemistry unless the thermochemistry of the fragments is well known.

Traditional calorimetric methods have providee high precision values for many hydrocarbons but are limited as molecular size increases and especially as functional groups with heavier atoms are substituted. Reported uncertainties in the alkanes range from ±0.4 kJ•mol^{-1} for methane to ± 1.3 kJ•mol^{-1} for octane.[3] The chloro-, bromo-, and iodobenzene are known to 1.3, 4.1 and 5.9 kJ•mol^{-1} respectively. As the size of the molecule increases, the heats of combustion typically become higher, requiring higher precision in temperature measurement to obtain the same precision thermochemistry. Additionally these measurements rely upon complete reaction of the

species which becomes less likely with larger molecules and heavier atoms. For heavier atoms, especially metal atoms, multiple oxidation states can be formed, which greatly complicates the extraction of reliable thermochemistry.

Previously overlooked factors also become significant when determining high precision thermochemical values. Theoretical methods, as well as photoionization techniques (*e.g.* photoionization mass spectrometry (PIMS) and photoelectron-photoion coincidence (PEPICO)) rely upon heat capacity functions to convert the 0K to 298 K thermochemistry. Uncertainty in the heat capacity, becomes significant when dealing with sub kJ/mol precision because of uncertainties in the calculated vibrational frequencies, their anharmonic corrections, and the treatment of multiple internal rotations to determine the heat capacity function. There are several models[4-7] for treating internal rotations however most deal with only a single rotor and, depending on which one is used, results for the H_{298}-H_0 can differ by 1 kJ•mol^{-1}.

1.1.1 Active Thermochemical Tables (ATcT)

The ATcT currently in development by Ruscic et al[8,9] are a network of experimentally measured bond energies, heats of combustion, heats of hydrogenation, electron affinities, etc. for neutral and ionic species. By minimizing the error in the network, uncertainties in thermochemical values are significantly reduced. Measuring accurate bond dissociation energies of larger molecules to common fragments links these molecules into the thermochemical network. It is especially important to determine accurate energetics for stable ions for which the heats of formation have been elusive such as the ones studied here: $C_6H_5^+$, i-$C_3H_7^+$, and t-$C_4H_9^+$.

1.1.2 Useful values derived from the E_0

1.1.2.1 Heats of formation of Ions

Mass spectrometry provides a direct route to the heats of formation of gas phase ions. The E_0 is related to the thermochemistry of the reaction constituents by the equation below.

$$\text{HAB} \xrightarrow{h\nu} HA^+ + B + e^- \qquad E_0(HA^+) = \Delta_{rxn}H \qquad\qquad 1.1$$
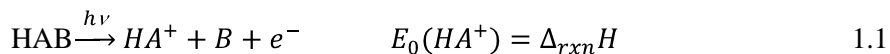
Therefore, if the thermochemistry of any two of the reaction participants, HAB, B and HA$^+$, are known, the heat of formation of the third species can be determined from the measured E$_0$. Related thermochemistry can then be derived from $\Delta_f H$(HA+). If the $\Delta_f H$(A) is known, then the proton affinity of A can be determined by the following reaction.

$$A + H^+ \rightarrow HA^+ \qquad PA(A) = -\Delta_{rxn}H \qquad\qquad 1.2$$
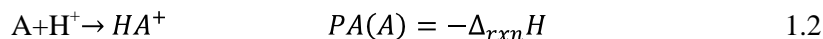
In Ch. 4 a new value for $PA(i\text{-}C_4H_{10})$, which is an important value for the anchoring the proton affinity scale, is determined from $\Delta_f H(t\text{-}C_4H_9{}^+)$

1.1.2.2 Neutral bond dissociation energies and radical ionization energies

Neutral thermochemistry can be linked to more easily measured ionic onset energies by the ionization energy of the radical product of the neutral dissociation. The neutral bond dissociation energy can be derived from the E_0 using Eqn. 1.3.

$$BDE = E_0 - IE_{rad} \qquad\qquad 1.3$$

However, radical ionization energies are often difficult to determine by conventional methods such as PIMS or photoelectron spectroscopy (PES). First, it is often difficult to cool radicals sufficiently in a molecular beam, which for large molecules often results in significant population of vibrationally excited radicals that ionize at photon energies lower than the ionization energy (*i.e.* hot bands). Second, it is common for removal of the lone electron of the radical to result in a geometry change which will result in poor Franck-Condon factors for the $v_0 \rightarrow v'_0$ transition. These factors respectively cause underestimation and overestimation of the ionization energy, obscuring direct measurement of the adiabatic *IE*. Measuring the E_0 for systems where the neutral BDE is known will yield the IE_{rad}. The IE_{rad} can then be used in similar systems where the BDE is unknown.

1.2 Measurement of Ionic Dissociations

1.2.1 Photoionization Mass Spectrometry (PIMS)

In PIMS, the mass analyzed ion signal is measured as the photon energy is scanned. The resulting spectrum is called the photoionization efficiency (PIE) curve. Figure 1- 1 shows that, as the photon energy is increased, fragment ions of a particular mass are formed and the mass selected signal for that ion will increases. The energy at which this begins to occur is called the appearance energy (*AE*).[10] Figure 1- 1 also shows that the appearance energy is related to the dissociation onset E_0 by the internal energy ($<E_{vib}>+<E_{rot}>$) of the neutral precursor. The *AE* is determined by drawing a line through a linear portion of the PIE curve to the baseline. The point where this line and the baseline intersect is then defined as the *AE*. The PIE curve is dependent upon experimental conditions such as photon intensity, sample pressure, or a broad internal energy distribution as well as Franck-Condon factors and competition from lower energy channels. Often these factors make determining the "linear portion" of the PIE curve somewhat subjective and results in impractically large uncertainties that are underestimated.

1.2.2 Photoelectron-Photoion Coincidence (PEPICO)

PEPICO experiments measure ions in coincidence with their emitted electron. This allows energy selection of ions by use of energy conservation. The excess photon energy, $h\nu$-IE_{ad}, is partitioned between the internal energy of the ion and the kinetic energies of the electron and ion.

$$h\nu = IE_{ad} + E_{int} + KE_{e^-} \qquad\qquad 1.4$$
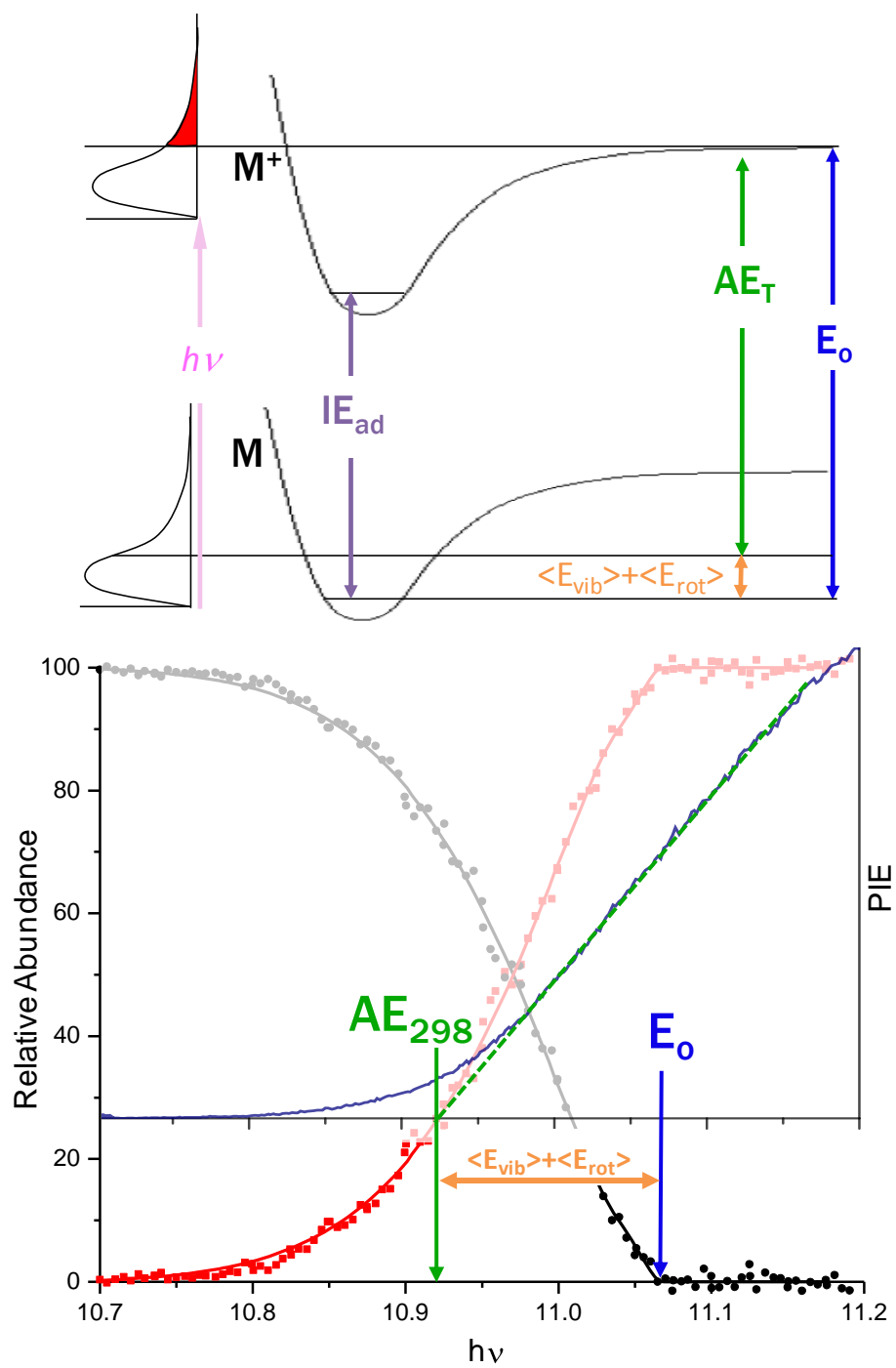
Figure 1- 1 Experimental and Theoretical Definitions of E_0 and AE_T.

Due to conservation of momentum, the KE_{ion} term is negligible and can be excluded. For a given photon energy, there will be a distribution of electron kinetic energies (*i.e.* the photoelectron spectrum) and therefore a distribution of ion internal energies. This means that even at photon energies well above the E_0, some parent ions will be generated because most of the excess energy is partitioned into the kinetic energy of the electron. We can simplify the equation above by only collecting ions that are in coincidence with zero kinetic energy electrons (ZEKE). This eliminates the last term in eq. 1.7 making the total ion internal energy:

$$E_{int} = h\nu - IE_{ad} + E_{Th} \qquad\qquad 1.5$$

where E_{Th} is the thermal energy of the neutral molecule which is determined from the experimental sample temperature and calculated vibrational frequencies and rotational constants. The degree to which we know the ion internal energy corresponds directly to the photon energy resolution and how effectively we can discriminate against energetic (hot) electrons.

PEPICO spectra are TOF spectra consisting of energy selected ions. These spectra are acquired at different photon energies and therefore different ion internal energies. Relative abundances of the observed ion from each spectrum are plotted as a function of the photon energy to generate a breakdown diagram (see Figure 1- 1). Unlike a PIE curve, the breakdown diagram has the advantage of being independent of Franck-Condon factors and experimental conditions such as light intensity and sample pressure. For simple rapid dissociations, Figure 1- 1 also shows that the relative abundances in the breakdown diagram are determined by the fraction of the ion internal energy distribution that lies above the dissociation threshold (red portion of the thermal energy distribution in Figure 1-1) and that the photon energy at which the parent ion abundance disappears is equal to the observed E_0. There is, thus, no arbitrariness in establishing the dissociation limit.

1.3 Kinetic and Competitive Shifts

According to unimolecular statistical theory, the dissociation rate is directly proportional to the probability that the ion will "find" a dissociative state. The Rice, Ramsperger, Kassel, Marcus (RRKM) equation is an improved version of the RRK equation,which assumes incorrectly that the molecule is composed of identical oscillators and that internal energy is large enough to treat these oscillators classically.   R. A. Marcus (then a post doctoral fellow with O.K. Rice at the University of North Carolina) modified the theory to consider individual oscillators using quantum mechanics. The RRKM equation defines the dissociation rate as

$$k(E) = \frac{\sigma N^{\ddagger}(E - E_0 + IE_{ad})}{h \rho(E)} \qquad 1.6$$

where σ is the reaction degeneracy, E is the ion internal energy measured relative to the ion ground state, E_0 and IE are measured from the neutral ground state, $N^{\ddagger}(E-E_0+IE_{ad})$ is the transition state sum of states (the number of states that will lead to dissociation), h is Planck's constant, and $\rho(E)$ is the ion density of states (the total number of states for an ion of a given internal energy). The minimum rate constant is located at the ion internal energy, $E = E_0 - IE_{ad}$. Thus the minimum rate constant, k_{min}, is

$$k_{min} = \frac{1}{h \rho(E_0 - IE)} \qquad 1.7$$

The minimum rate constant is dependent upon the height of the barrier and the energy dependence of $\rho(E)$. The latter depends upon the number of vibrational degrees of freedom of the molecule. If k_{min} is too slow to be measured by a particular experiment, as is shown by the experimental window in Figure 1- 2, then ions with enough energy to dissociate will not have enough time to do so before detection and a false threshold that is dependent upon experimental conditions will be observed. It should be noted the experimental window is determiend by the ion residence time and that trapping experiments could extend this indefinitely. However if k_{min} is low enough ($\sim 10^2$ s^{-1}), then radiative cooling by emission of infrared photons eventually becomes competitive with the dissociation rate and fragmentation at threshold will be impossible
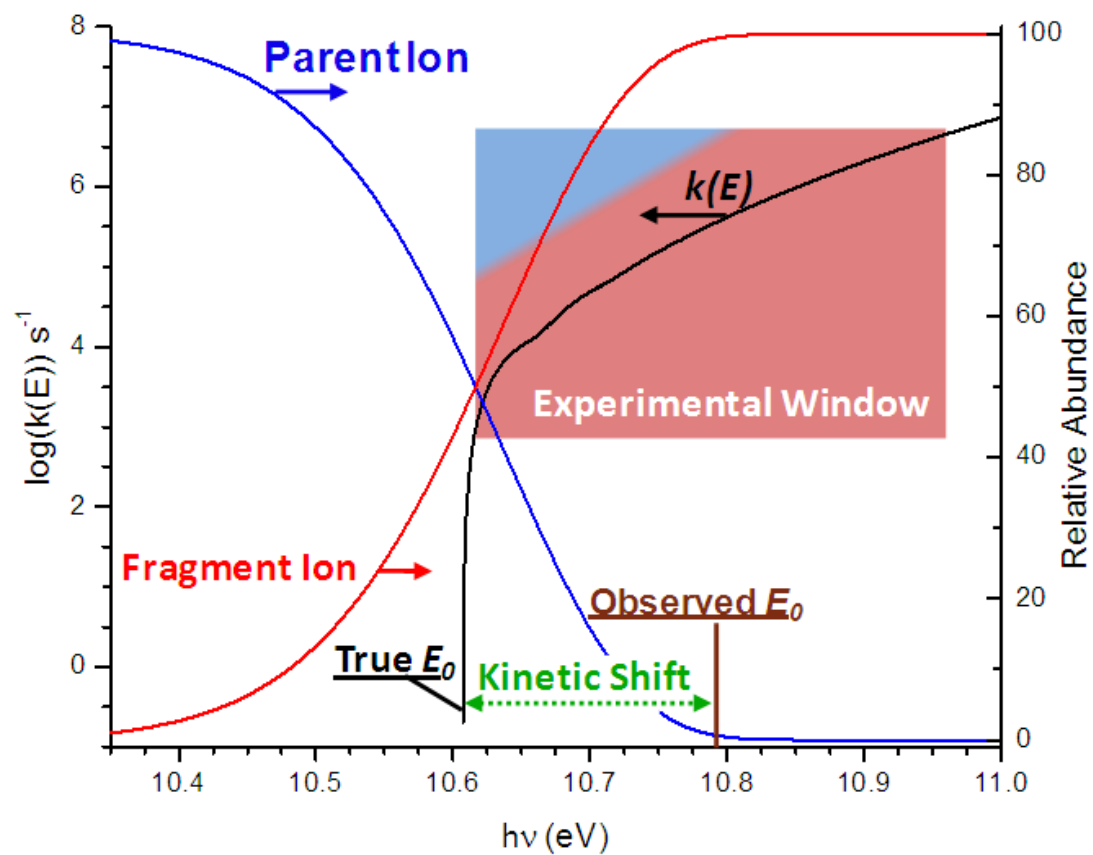
Figure 1- 2 Definition of Kinetic Shift.

to observe experimentally.[11] The use of eq. 1.6 to extrapolate to the true E_0 is thus required for slow dissociations. Figure 1- 2 shows the kinetic shift as the difference in energy between the observed and the true threshold.

When a dissociation of interest competes with a lower energy dissociation pathway, the branching ratios are determined by the ratio of the rate constants of the dissociating channels.

$$\frac{[A]}{[B]} = \frac{k_A(E)}{k_B(E)} = \frac{\sigma_A N^{\ddagger}(E - E_A + IE)}{\sigma_B N^{\ddagger}(E - E_B + IE)}$$ 1.8

Higher energy channels only become visible when they are within about 2 orders of magnitude of the fastest dissociation pathway. This results in fragments not being observable at their dissociation threshold due to a competitive shift. For dissociations of interest with a competitive shift, the only way to extract energetic information is by modeling the data using eq. 1.3 and statistical rate theories to model the experimental data.

1.3.1 The Various Unimolecular Reaction Rate theories

In the presence of a shift, either competitive or kinetic, unimolecular rate theories are required to extrapolate to the dissociation threshold. These theories differ in their models of the transition state (TS), which determine the energy dependence of $N^{\ddagger}(E)$ and $k(E)$. Using different rate theories will result in different values determined for E_0.

Phase space theory (PST)[12-16] assumes that (in absence of a centrifugal barrier) the transition state is fixed at infinity along the reaction coordinate. As the molecule dissociates, energy in the vibrational modes corresponding to the bending and (if applicable) torsional motion of the broken bonds is converted into rotational motion of the fragments. Thus by placing the transition state at infinity, PST assumes that the transitional modes have completely converted into rotations. For a polyatomic ion dissociating to non-linear polyatomic fragments, one vibrational mode is converted into the reaction coordinate, and five vibrational modes are converted into

product rotations. Because of these free rotors, the energy dependence of $N^{\ddagger}(E)$ is very strong.. As a result, PST represents the upper limit to $k(E)$ and therefore the extrapolated E_0.

RRKM theory[17] assumes that the TS is composed entirely of n-1 vibrational oscillators (compared to n-6 for PST), where n is the number of vibrational modes in the ion. The RRKM TS is therefore located further inward on the reaction coordinate (where the ion is still intact) than the PST TS. RRKM theory works best for dissociations with an energetic barrier along the reaction coordinate, usually associated with a rearrangement process Often, this energetic barrier corresponds to a transition state geometry that is tighter (*i.e.* the vibrational frequencies of the TS are higher) than for the ion equilibrium geometry. Because of these higher vibrational frequencies, the energy dependence of $N^{\ddagger}(E)$ is weaker, and $k(E)$ rises more slowly with E..

The two rate theories, which assume that the transition state is located close in (RRKM) and at infinite product separation (PST), assume that the TS is independent of the ion internal energy. This is often not true for dissociations that occur homolytically. For such dissociations, the potential energy increases monotonically along the reaction coordinate without an energetic barrier. As a result, the TS is determined by an entropic bottleneck which, at low energies, is located at infinite bond distances and moves inward as the ion internal energy is increased.[17]

Variational transition state theory (VTST)[18-20] locates the transition state by determining the minimum in $N^{\ddagger}(E-V(R))$ as the molecule moves on the potential energy curve $V(R)$ along the reaction coordinate (R). This minimum results from competing trends in $N^{\ddagger}(E-V(R))$. Increasing the bond distance causes $E-V(R)$ and $N^{\ddagger}(E-V(R)$ to decrease. At the same time, the disappearing vibrational modes, which turn into rotations, cause the $N^{\ddagger}(E-V(R))$ to increase. Determining this minimum requires $V(R)$ to be determined, as well as the vibrational frequencies as a function of the reaction coordinate. However, there is considerable uncertainty in the calculated potential and vibrational frequencies at large R. Several models have been proposed that use analytical functions to describe $V(R)$ and the changing vibrational modes.[18-20] Depending on which model is used, one

or two minima may be observed in $N^{\ddagger}(E\text{-}V(R))$, a tight transition state (TTS) at shorter R and an outer orbiting transition state (OTS).[21] At low energies, the OTS is the global minimum but as the internal energy is increased, the tight transition state becomes the global minimum. It is not clear whether this transition state switching is an artifact of particular approximations used in the model.[22]

Another model is the statistical adiabatic channel model (SACM) in which the quantum states of the reactant are assumed not to change (although their energies change as the vibrational frequency changes during the reaction) throughout the dissociation. For a given quantum state dissociation is assumed to proceed by an adiabatic potential energy curve that links reactant and product. Each potential curve has a barrier, the maximum of which moves inward along the reaction coordinate as the energy and angular momentum of the channel increase. If the molecule has enough energy to dissociate along a particular curve then the rate constant for that quantum state is determined using eqn. 1.2. A total rate constant is obtained by summing these rates over a statistical distribution of quantum states. [17]

A full implementation of either VTST or SACM requires significant computational effort. It is shown in Ch. 4 that both a parameterized version of VTST as well as a simplified SACM (SSACM), which calculates $k(E)$ using the much simpler PST with suitable scaling factors, are capable of extrapolating the $k(E)$ function to within the uncertainty of the correct E_0 over nearly 500 meV.[23] Additionally, SSACM, has been shown to reproduce rate constants derived from a full SACM-classical trajectory (SACM-CT) treatment. [24] It is also shown in Chapter 4 that using PST and RRKM theory to extrapolate to the E_0 for the halogen loss of the halobenzenes disagree by as much as 200 meV, with PST over estimating, and RRKM underestimating the E_0.[23,24]

1.3.2 Synchrotron based studies (iPEPICO)

Synchrotron radiation is tunable over, for our purposes, an essentially unlimited range ($<8\rightarrow>4000$ eV). Additionally the photon flux of synchrotron radiation (10^{11}-10^{12} photons/s at 10

11

eV[25]) is significantly higher than those achieved by tunable monochromatized laboratory emission sources. Because of this high flux, higher photon energy resolution is possible for coincidence experiments which are often limited by low signal intensity. Several new PEPICO apparatuses have been built at synchrotrons around the world. Two have been built in Europe, DELICIOUS II[26] at the French Synchrotron Soleil and the iPEPICO apparatus[27] at the Swiss Light Source (SLS) synchrotron and a third in China at the Beijing Synchrotron Radiation Facility.

Reference List

1. Tajti, A.; Szalay, P. G.; Csaszar, A. G.; Kallay, M.; Gauss, J.; Valeev, E. F.; Flowers, B. A.; Vazquez, J.; Stanton, J. F. HEAT: high accuracy extrapolated ab initio thermochemistry, *J. Chem. Phys.* **2004,** *121* , 11599-11613.

2. Karton, A.; Rabinovich, E.; Martin, J. M. L.; Ruscic, B. W4 theory for computational thermochemistry: In pursuit of confident sub-kJ/mol predictions, *J. Chem. Phys.* **2006,** *125* , 144108-1-144108/17.

3. Pedley, J. B. *Thermochemical Data and Structures of Organic Compounds;* Thermodynamics Research Center: College Station, 1994.

4. Pitzer, K. S.; Gwinn, W. D. Energy levels and thermodynamic functions for molecules with internal rotation I. Rigid frame with attached tops, *J. Chem. Phys.* **1942,** *10* , 428-440.

5. McClurg, R. B.; Flagan, R. C.; Goddard, W. A. I. The hindered rotor density-of-states interpolation function, *J. Chem. Phys* **1997,** *106* , 6675-6680.

6. Knyazev, V. Comment on "Hindered rotor density-of-states interpolation function" [J. Chem. Phys. 106, 6675 (1997)] and "The hindered rotor density-of-states" [J. Chem. Phys. 108, 1748 (1998)], *J. Chem. Phys* **1999,** *111* , 7161-7162.

7. Ayala, P. Y.; Schlegel, H. B. Identification and treatment of internal rotation in normal mode vibrational analysis, *J. Chem. Phys.* **1998,** *108* , 2314-2325.

8. Ruscic, B.; Pinzon, R. E.; Morton, M. L.; Laszevski, G.; Bittner, S. J.; Nijsure, S. G.; Amin, K. A.; Minkoff, M.; Wagner, A. F. Introduction to Active Thermochemical Tables: Several "Key" Enthalpies of Formation Revisited, *J. Phys. Chem. A* **2004,** *108* , 9979-9997.

9. Ruscic, B.; Pinzon, R. E.; Morton, M. L.; Laszevski, G.; Bittner, S. J.; Nijsure, S. G.; Amin, K. A.; Minkoff, M.; Leahy, D.; Montoya, D.; Wagner, A. F. Active Thermochemical Tables: thermochemistry for the 21st century, *J. Phys. Conf. Ser.* **2005,** *16* , 561-570.

10. Traeger, J. C.; McLoughlin, R. G. Absolute heats of formation for gas phase cations, *J. Am. Chem. Soc.* **1981,** *103* , 3647-3652.

11. Dunbar, R. C. Infrared Radiative Cooling of Gas-Phase Ions, *Mass Spectrom. Rev.* **1992,** *11* , 309-339.

12. Light, J. C. Phase space theory of chemical kinetics, *J. Chem. Phys.* **1964,** *40* , 3221-3229.

13. Pechukas, P*.;* Light, J. C. On detailed balancing and statistical theories of chemical kinetics, *J. Chem. Phys.* **1965,** *42* , 3281-3291.

14. Nikitin, E. E. Statistical theory of endothermic reactions: Part 2. Monomolecular reactions, *Theor. Exp. Chem.* **1965,** *1* , 90-94.

15. Klots, C. E. Reformulation of the quasiequilibrium theory of ionic fragmentation, *J. Phys. Chem.* **1971,** *75* , 1526-1532.

16. Chesnavich, W. J.; Bowers, M. T. Statistical phase space theory of polyatomic systems: Rigorous energy and angular momentum conservation in reactions involving symmetric polyatomic species., *J. Chem. Phys.* **1977,** *66* , 2306-2315.

17. Baer, T.; Hase, W. L. *Unimolecular Reaction Dynamics: Theory and Experiments;* Oxford University Press: New York, 1996.

18. Chesnavich, W. J. Multiple transition states in unimolecular reactions, *J. Chem. Phys.* **1986,** *84* , 2615-2619.

19. Hase, W. L. The criterion of minimum state density in unimolecular rate theory. An application to ethane dissociation, *J. Chem. Phys.* **1976,** *64* , 2442-2449.

20. Klippenstein, S. J.; Marcus, R. A. Application of unimolecular reaction theory for highly flexible transition states to the dissociation of CH_2CO into CH_2 and CO, *J. Chem. Phys.* **1989,** *91* , 2280-2292.

21. Chesnavich, W. J.; Bass, L.; Su, T.; Bowers, M. T. Multiple transition states in unimolecular reactions: A transition state switching model. Application to the $C_4H_8^+$ system, *J. Chem. Phys.* **1981,** *74* , 2228-2246.

22. Hu, X.; Hase, W. L. Properties of canonical variational transition state theory for association reactions without potential energy barriers, *J. Phys. Chem.* **1989,** *93* , 6029-6038.

23. Stevens, W.; Sztáray, B.; Shuman, N.; Baer, T.; Troe, J. Specific Rate Constants k(E) of the Dissociation of the Halobenzene Ions: Analysis by Statistical Unimolecular Rate Theories, *J. Phys. Chem. A* **2009,** *113* , 573-582.

24. Troe, J.; Ushakov, V. G.; Viggiano, A. A. On the Model Dependence of Kinetic Shifts in Unimolecular Reactions: The Dissociation of the Cations of Benzene and n-Butylbenzene, *J. Phys. Chem. A* **2006,** *110* , 1491-1499.

25. Johnson, M.; Bodi, A.; Schulz, L.; Gerber, T. New vacuum ultraviolet beamline at the Swiss Light Source for chemical dynamics studies, *Nucl. Instrum. Methods Phys. Res. A* **2009,** *610* , 597-603.

26. Garcia, G. A.; Soldi-Lose, H.; Nahon, L. A versatile electron-ion coincidence spectrometer for photoelectron momentum imaging and threshold spectroscopy on mass selected ions using synchrotron radiation, *Rev. Sci. Instrum.* **2009,** *80* , 023102-1-023102/12.

27. Bodi, A.; Johnson, M.; Gerber, T.; Gengeliczki, Z.; Sztáray, B.; Baer, T. Imaging photoelectron photoion coincidence spectroscopy with velocity focusing electron optics, *Rev. Sci. Instrum.* **2009,** *80* , 034101-1-034101/7.

CHAPTER 2: Experimental Description

2.1 TPEPICO Description

The TPEPICO apparatus, which has been described in several publications, [1-3] consists of a VUV light source, a temperature controlled inlet, an electron energy analyzer, either a linear or reflectron time of flight (TOF) analyzer, and electronics to correlate the ion and electron signals. The sample gas enters the chamber effusively through a stainless steel needle. A needle valve regulates the flow of gas into the chamber so that the chamber pressure is about 10^{-5} mbar (base pressure = 10^{-7} mbar). Vacuum ultraviolet (VUV) light emitted from a H_2 discharge lamp dispersed by a 1 m normal incidence monochromator ionizes the sample gas in a temperature controlled ionization region. The width of the entrance and exit slits of the monochromator were set to 100 μm, providing a resolution of 1 Å. The wavelength was calibrated using the Lyman-α emission line.

Upon ionization, an extraction field of 20 V•cm^{-1} accelerates the electrons and ions in opposite directions. Ions travel through either a linear or reflectron TOF analyzer before impacting a tandem MCP detector. Velocity focusing optics direct both threshold electrons and hot electrons that have zero velocity perpendicular to the extraction axis onto a 1.3 mm circular aperture at the end of a 12 cm electron drift region where they are detected by a Burle channeltron detector (see Figure 2-1). A second off-axis channeltron detector behind a 3x5 mm rectangular aperture collects the background signal of

energetic or hot electrons. We assume that this hot electron signal is representative of the hot electron signal at the center detector. The hot electron signal is used to correct the contaminated center threshold signal for hot electrons whose initial velocity vector is perpendicular to the extraction axis. (See Section 2.1.3.3)

A time-to-pulse height converter (TPHC) converts the time difference between the center or cold electron detector signal and ion MCP signal (*i.e.* the ion TOF) to pulse height. A multichannel pulse height analyzer (MCPHA) generates the center TOF spectrum from the TPHC pulses. A second TPHC and MCPHA generate the hot electron TOF spectrum using the off-axis electron detector signal as a start and the ion signal as a stop.

2.1.1 Linear Time of Flight Mass Configuration

In the linear time of flight configuration, a field voltage of 20 V•cm^{-1} is used to accelerate the ions over 5 cm to 100 eV. The ions are accelerated again from 100 eV to 250 eV over 2 mm before entering a 25 cm drift region. The ions then enter a second shorter drift region of 8 cm, the voltage of which can be varied to separate fragment ions formed in the first drift region before impacting a tandem MCP detector. When the voltage applied to the second drift region is 250 V, the same as the first drift region, the voltages meet the Wiley-McLaren space focusing condition.[4] The peak width is This means that all ions of the same mass will have the same time of flight regardless of starting position and therefore determined by the sample's thermal translational energy.

Figure 2-1 shows the dependence of the total time of flight of a fragment ion upon the position in the spectrometer where it was formed as well as the kinetic information available from its TOF spectrum. Dissociations with *k(E)* greater than 10^7 s^{-1}

occur essentially instantaneously. For instance, an ion with an m/z of 50 travels only

0.02 mm in the first 10^{-7} s in a 20 V/cm field.   As a result these rapidly formed fragment

ions appear at the time of flight corresponding to the mass of the fragment ion. Fragment

ions that are formed in the first acceleration region have a time of flight that corresponds

to the position in the acceleration region at which they were formed. Ions that dissociate

sooner have shorter times of flight than those that dissociate later in the acceleration

region. This dependence results in an asymmetric fragment peak (peak a, Figure 2-1).

The shape of the fragment peak corresponds to the decay of the parent ion abundance. If

fragments are formed in the first drift region of the spectrometer then the lighter ions will

have the same velocity as the parent ion and therefore less kinetic energy. These slow

moving fragment ions can be separated from the parent ions by setting the second drift

region to a higher potential than the first drift region.   The potential difference between

the two drift regions provides a barrier over which the slow moving fragment ions must

cross. Because the fragment ions are lighter, they are decelerated more and thus have a

longer time of flight than the parent ion (peak b, Figure 2-1). The drift peak area

provides a point significantly further along parent ion decay curve than the asymmetric

fragment peak. This extends the window over which we can determine kinetic

information to rates below 10^3 s^{-1} for m/z=100. Decelerating the ions between the first

and second drift region moves the Wiley-McLaren focal point away from the detector

and therefore causes an increase in the TOF peak widths. However, this was not a

problem for the metastable systems studied because the mass difference between the

Figure 2-1 TPEPICO experimental apparatus with linear TOF analyzer. The fragment ion time of flight is dependent upon the location at which it dissociates. (a) If the fragment is formed in the first acceleration region (blue) then the fragment ion will appear as part of the asymmetric fragment peak. (b) if the fragment ion is formed int the first drift region (green) then the fragment will appear as a drift peak at longer times of flight than the parent ion. (c) Lastly if the fragment ion does not dissociate before the end of the first drift region, then the fragment ions will appear as parent. (red)

the fragment peak corresponds to the decay of the parent ion abundance. If fragments are formed in the first drift region of the spectrometer then the lighter ions will have the same parent and fragment ions was large. Lastly the peak area of the parent ion (peak c, Figure 2-1) corresponds to ions that either dissociated in the second drift region or did not dissociate at all. The peak area of the parent allows normalization of the parent ion decay curve.

2.1.2 Reflectron TOF Configuration

Figure 2- 2 shows the PEPICO apparatus with the reflectron TOF configuration. As in the linear TOF configuration, ions are accelerated to 100 eV over 5 cm before entering the 40 cm long drift region without a second acceleration. Ions starting from different points in the ionization region come into focus near the front of the reflectron. The ions then travel through a 35 cm drift region before coming back into focus as they are detected on a tandem MCP detector. Voltages are once again determined using the Wiley-McLaren space focusing conditions. Similar to the linear TOF configuration, kinetic information is present in the TOF spectra of metastable ions in the form of an asymmetric fragment peak. However lower velocities and longer flight paths in the drift region mean that the metastable ions have more time to dissociate and that slower rate constants can therefore be determined from the reflectron drift peak.

The primary advantage the reflectron TOF configuration is its mass resolution of 350 which is better than the linear TOF by a factor of about 3.5. This is due to the longer flight times of the ions in the reflectron. These longer flight times result in a disadvantage due to the fact that fragment ions formed in the drift region that are significantly lighter than the parent ion have much less kinetic energy. These ions are not efficiently reflected toward the detector and can be lost.
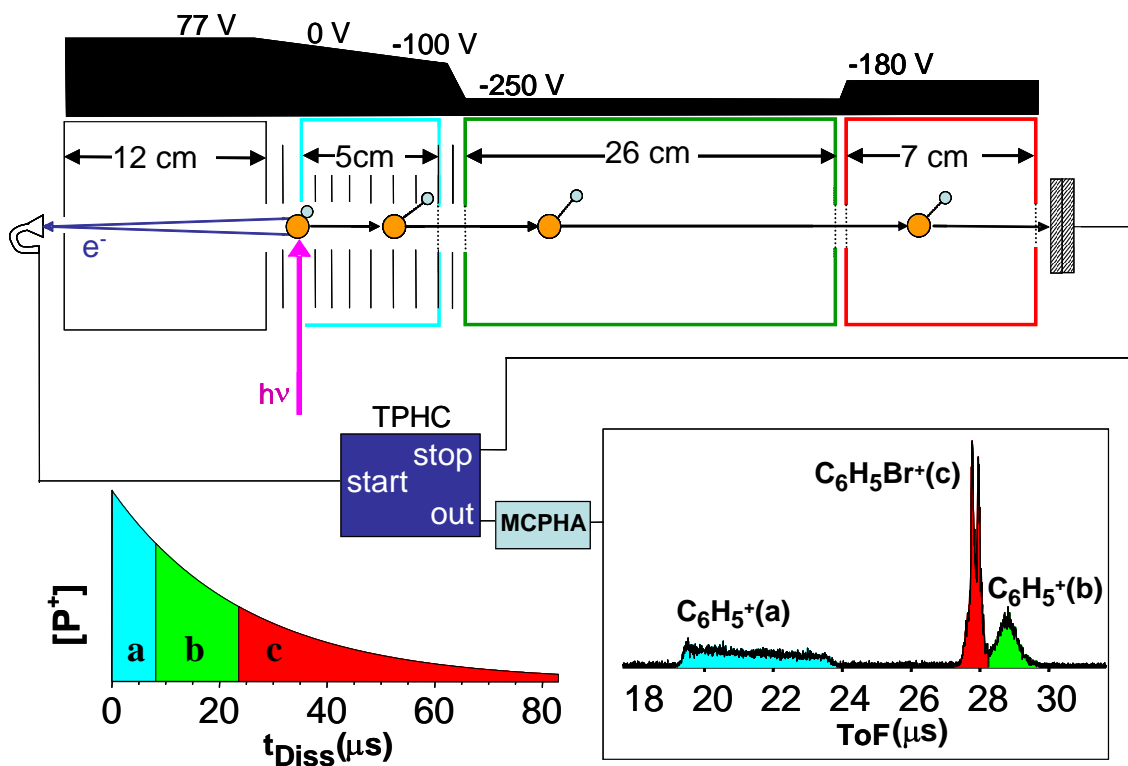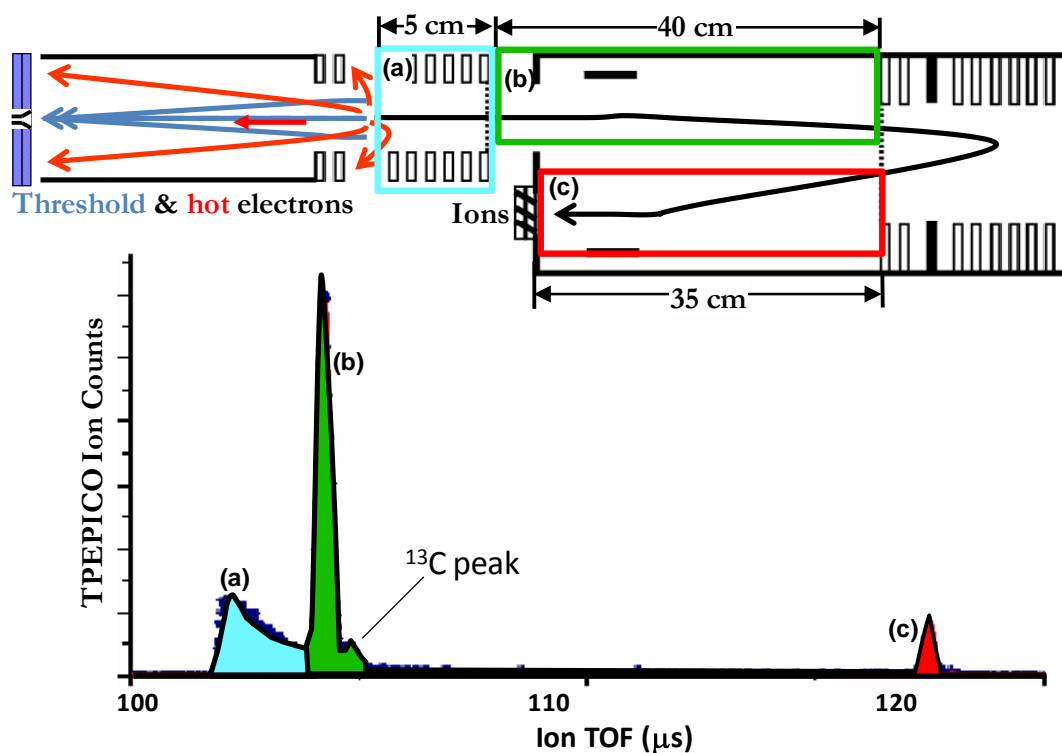
Figure 2- 2 TPEPICO experimental apparatus with reflectron TOF analyzer. The fragment ion time of flight is dependent upon the location at which it dissociates. (a) If the fragment is formed in the first acceleration region (blue) then the fragment ion will appear as part of the asymmetric fragment peak. (b) if the fragment ion is formed in the first drift region (green) then the fragment will appear as a drift peak at the end of the fragment peak. (c) Lastly if the fragment ion does not dissociate before the end of the first drift region, then the fragment ions will appear as parent. (red)

2.1.3 Detailed Experimental information

2.1.3.1 Temperature Controlled Inlet

A temperature controlled inlet is used to control the temperature of the neutral sample gas flowing into the chamber. The inlet consists of a 1.5" x 1.5" x 5" copper block housing which contains a sample line, cooling line, and cartridge heater. The sample line runs through the center of the block and terminates in a stainless steel capillary just above the ionization region. The first extraction plates of both the electrons and the ions are located 6 mm away from the ionization spot. They are each copper plates with a central hole 0.5" in diameter. These plates are in thermal contact with the copper block so that the entire ionization region is isothermal, however Teflon spacers serve as electrical insulators so that voltages can be applied. A thermocouple placed between the Teflon sheet and copper block allows direct monitoring of the sample temperature. Temperatures below room temperature are maintained by a Neslab ULT-80 ultralow temperature circulating bath containing denatured ethanol which is capable of maintaining constant temperatures at the copper block over a range from 240 K to 300 K. Using this method, the temperature drift was less than 1° over the course of an experiment.

2.1.3.2 Velocity Focusing

Threshold PEPICO experiments must compromise between electron energy resolution, which increases with decreasing electric field, and mass resolution, which increases with increasing electric field. Traditionally, fields of about 1 V/cm were used for adequate electron energy resolution while typical fields for mass spectrometry were at least an order of magnitude greater. A major breakthrough for PEPICO techniques has been the use of velocity focusing
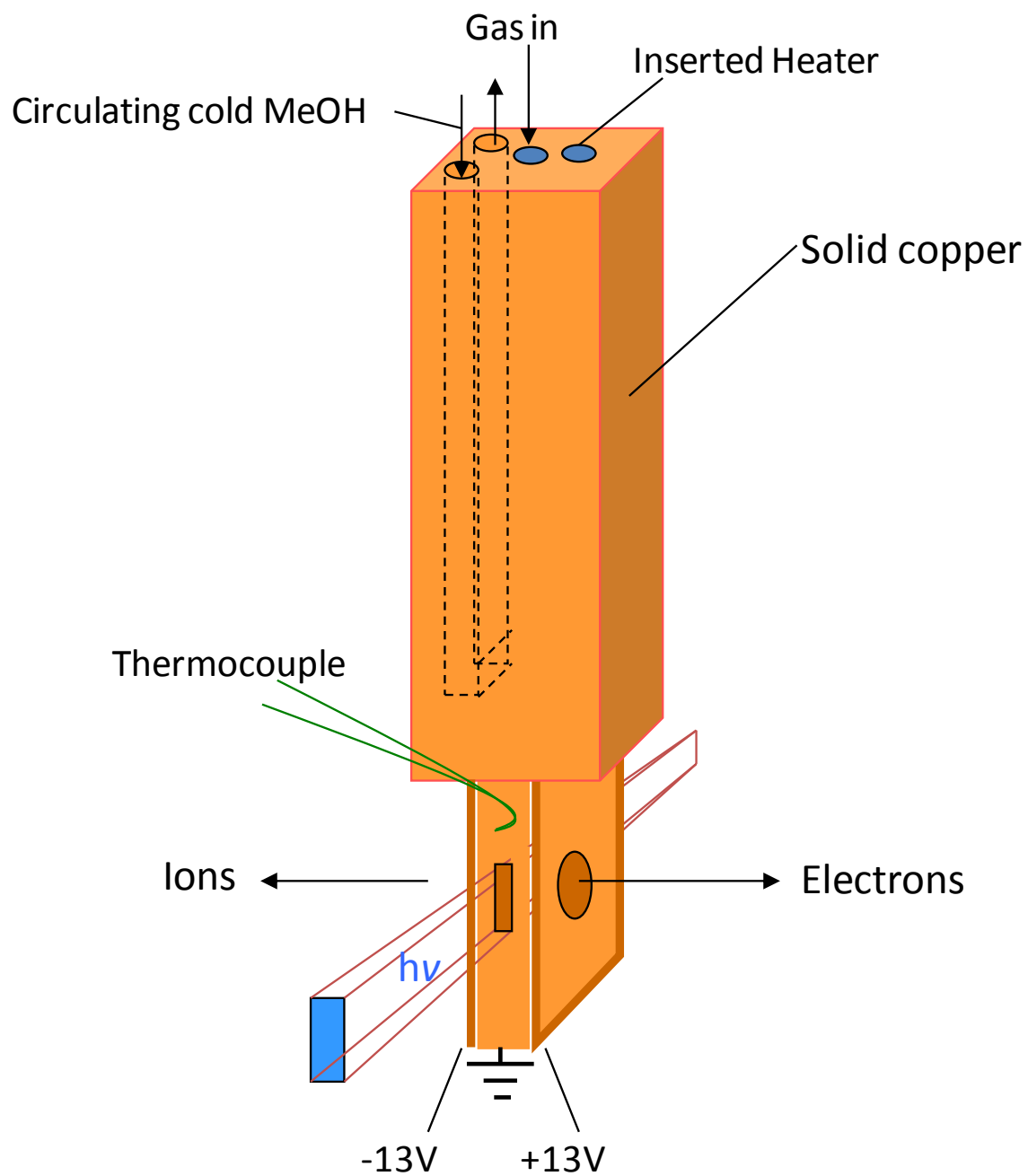
Figure 2- 3 Schematic of temperature controlled inlet.

optics for the energy analysis of electrons. Velocity focusing of the electrons is accomplished by extracting them from the ionization region through an electrostatic lens, consisting of extraction plates with no grids. Figure 2- 4 shows that by properly adjusting the voltages, threshold electrons are focused to a central spot at the end of the flight tube while energetic or hot electrons are focused to concentric rings around the central spot. The radius of the rings is determined by their velocity perpendicular to the extraction axis. Velocity focusing allows for the use of larger extraction fields without sacrificing electron energy resolution. Velocity focusing optics permits threshold electrons to be focused from a much larger ionization region than was previously possible with an electrostatic analyzer and gridded extraction plates which do not focus the electrons. Additionally it allows for extraction fields as high as 40 V/cm. Electron and ion collection efficiencies are often 35% and 25% respectively.

2.1.3.3 Correction for energetic electron contamination in TOF spectra.

PEPICO spectra consist of TOF spectra from energy selected ions. These spectra must be corrected for contamination from ions with lower internal energy due to emitting an energetic electron directly toward the detector. This is done by subtracting a fraction of the off-axis TOF spectrum from the center TOF spectrum. The peak areas in the spectra are corrected using eq. 2.1

$$T_i = C_i - f\,H_i \qquad\qquad 2.1$$

Where T_i is the true threshold peak area of ion i, C_i is the peak area of ion i in the center spectrum, f is an experimentally determined factor, and H_i is the peak area of ion i in the off-axis (hot electron) spectrum. The magnitude of f depends upon both the relative
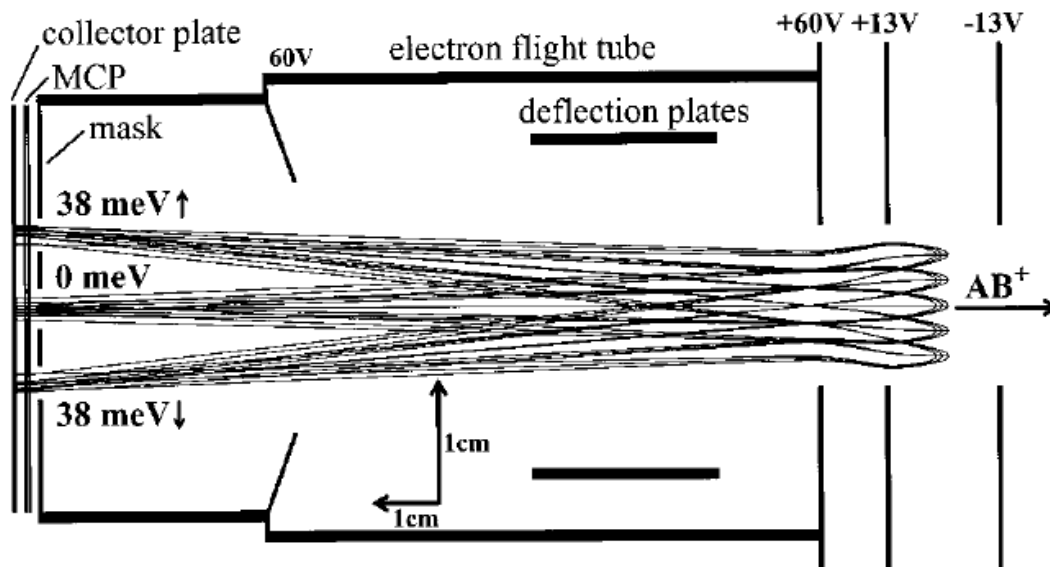
Figure 2- 4 Velocity focusing of electrons. When the velocity focusing condition is met, electrons without velocity perpendicular to the extraction axis are focused onto a central spot. Electrons with velocity perpendicular to the extraction axis are focused into concentric rings with radius corresponding to their velocity in this direction.

areas of the electron detectors, which is determined by the apertures through which electrons must travel to be detected, and the efficiencies of the two detectors. These efficiencies are hard to determine *a priori* therefore *f* is determined empirically. At high photon energies, well above the dissociation limit, the parent ion abundance in the center TOF spectrum must be due to hot electrons. *f* is thus determined by setting $fH_i = C_i$. Figure 2- 5 shows adequate hot electron correction by the dissapearnce of the parent at 13.6 eV, 4.5 eV above the ionization energy. This photon energy also corresponds to a region of low intensity in the PES *(i.e.* a Franck-Condon gap) where few threshold electrons are formed thereby causing hot electrons signal to be significant. Figure 2- 5 demonstrates the effect of the factor *f* on the breakdown diagram for chlorobenzene. The red curve indicates *f* =0 or no correction and the blue curve represents adequate correction for the hot electrons. If rate information is present in the TOF distribution, *(i.e.* $10^3 < k(E) < 10^7$) then the asymmetric peak shape must be preserved during correction of the center spectrum for hot electrons. In order to do this, the spectra are subtracted channel by channel. Because two different TPHCs and MCPHAs are used to collect the center and hot electron TOF spectra, the time width of a single channel is different for the two TOF spectra. As a result, the off-axis spectrum must be scaled to align with the center spectrum using the equation below.

$$i'_H = \sum_{n=1}^{s} a_i i_c^{n-1} \qquad\qquad 2.2$$

Where *s* is the number of peaks used to align the two spectra and is usually 2 or 3, i'_H is the channel number of the hot electron (H) TOF spectrum that corresponds to the channel number of the cold electron (C) TOF spectrum i_c, and a_i are fitting parameters used to align the two spectra. The scaled off axis channel numbers i'_c will be non-integer
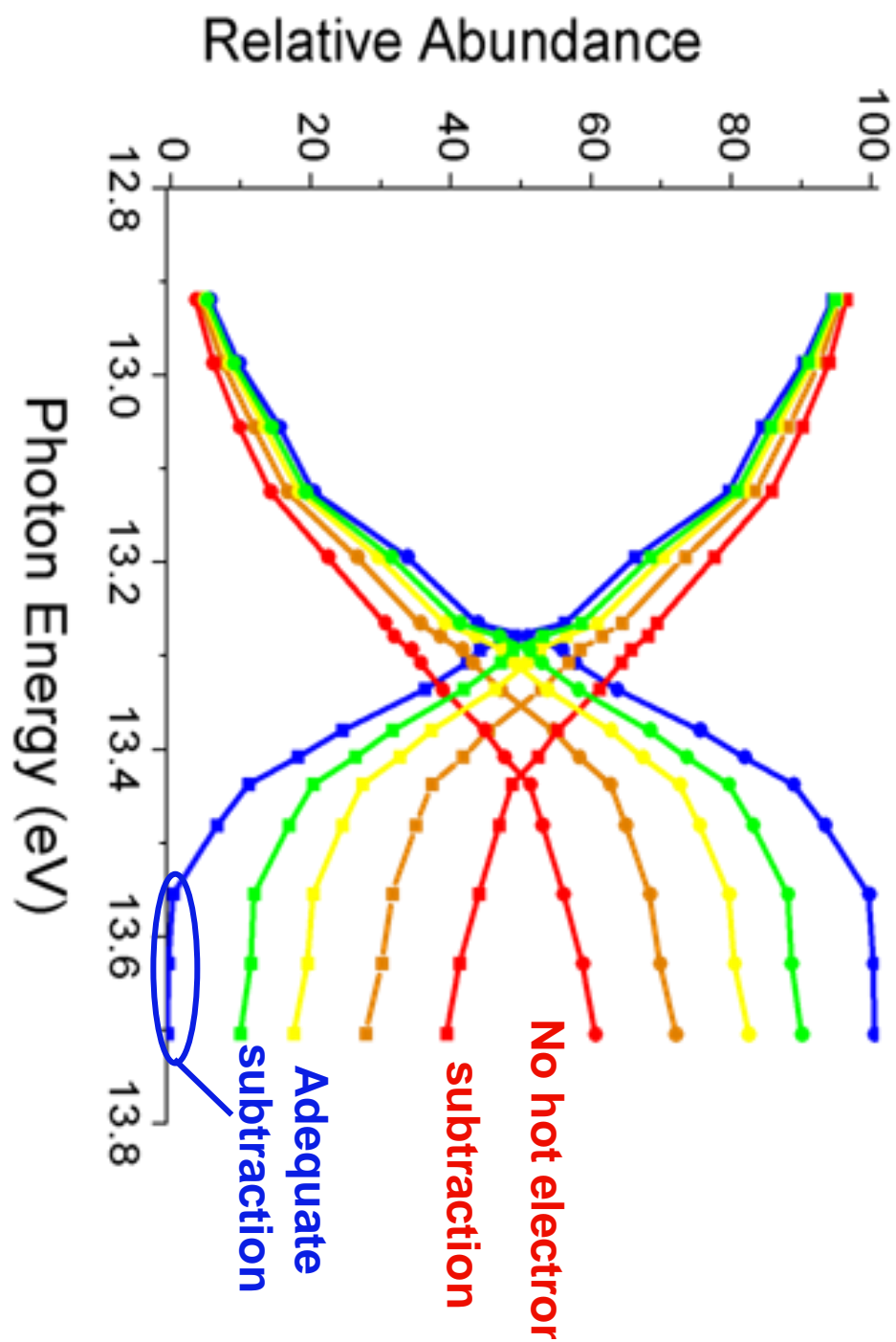
Figure 2- 5 Effect of hot electron correction in breakdown diagram of chlorobenzene.

channel numbers. To determine these intensities the ring spectrum is interpolated using a cubic spline algorithm. The scaled and interpolated hot electron spectrum can be subtracted from the center spectrum using eq. 2.1 where i now refers to center spectrum channel number.

2.2   iPEPICO Apparatus

The recently built imaging photoelectron-photoion coincidence (iPEPICO) spectrometer located at the X04DB VUV beam line at the Swiss Light Source Synchrotron of the Paul Scherrer Institute has been described in detail recently.[5,6]   Pure sample is effusively introduced at room temperature into the ionization region through a Teflon tube.   A needle valve is used to control the flow of sample gas into the experimental chamber so that the pressure was between $5x10^{-6}$ and $1x10^{-5}$ mbar. Synchrotron radiation ionizes the sample in a 2 x 4 mm interaction region after passing through an inline monochromator and gas filter which filters higher order harmonics. The well known Ar 11s´-14s´ and Ne 13s´,14s´, 12d´, and   13 d' autoionization lines are used to calibrate the photon energy. Upon ionization, a 40-80 $V \cdot cm^{-1}$ electric field accelerates the electrons and ions in opposite directions. The electrons travel vertically into a 26.5 cm flight tube. Velocity map imaging is used to focus the electrons onto a 40 mm diameter DLD40 Roentdek position sensitive delay-line detector. At 80 $V \cdot cm^{-1}$, threshold electrons were focused to a spot size of 0.9 mm x 0.4 mm which corresponds to 0.2 meV , much less than the photon resolution of 1 meV at 10 eV.   After acceleration, the ions pass through a second acceleration region followed by a linear time of flight mass analyzer and are space focused onto a Jordan TOF C-726 MCP detector.

Electron and ion signals as well as electron positions are recorded in the triggerless mode of a high performance time to digital converter card. The electron and ion hit times are measured relative to a master clock. All ions detected within a defined time window of an electron are correlated to obtain time-of-flight distributions This multiple start/multiple stop data acquisition scheme[7] enables data acquisition at ionization rates in excess of 100 kHz, which is beneficial at a high intensity light source, such as the synchrotron.

 The experimental data may be analyzed and plotted in many ways: at a single photon energy, the radial distribution of electrons positions on the image in Figure 2- 6 yields a portion of the photoelectron spectrum (PES); the threshold electron signal as a function of the photon energy yields a TPES; the threshold electron signal detected in coincidence with an ion in a particular TOF range yields a mass-selected TPES; the total ions in coincidence with all electrons as a function of photon energy yields the total ion curve; and the fractional ion abundances in the TOF spectra as a function of the photon energy yield the breakdown diagram.

Similar to TPEPICO, contamination of the threshold electron signal from hot electrons must be subtracted. Figure 2- 6 shows the regions on the electron image that are defined as the center and energetic electron background or 'ring'. The TPES is corrected for hot electrons by subtracting the number of counts in the ring region of the image multiplied by the same factor discussed in section 2.1.3.3 from the number of electron counts in the center region. With the imaging detector however, the efficiencies of the threshold and background regions are identical and therefore f is determined exclusively by the ratio of the center and ring areas. The ions that are in coincidence with

28

the electrons defined as either center or ring are used to generate center and ring TOF spectra. Threshold TOF spectra can then be generated using eq. 2.1 where i corresponds to channel number. Because hit times for both the ring and center electrons are recorded on a master clock and corresponding TOF spectra from these data post acquisition using software, the channel/TOF calibrations are the same for the center and ring TOF spectra and therefore do not require alignment prior to correction as described in section 2.1.3.3. Using this scheme, the energy resolution was ultimately limited by the photon energy resolution of 2.5 meV.

2.3 Modeling of experimental data

In order to determine reaction energetics and kinetics as precisely as possible, we model the experimental PEPICO data. Our approach to determining reaction energetics depends upon whether the ions dissociate rapidly on the timescale of our apparatus ($k(E)>10^7$ s^{-1}) or the ions dissociate slowly ($k(E)<10^7$ s^{-1}). If the dissociation is fast, then only the breakdown diagram is required to determine E_0. For slow dissociations, the individual TOF distributions are modeled to determine the $k(E)$ curve. In both cases, ions are produced from a room temperature sample of neutral molecules and therefore have a distribution of internal energies. It is approximated that the neutral internal energy distribution is transposed to the ionic manifold. To determine the ion internal energy distribution, the electron energy resolution, the spectral width of our light source (*ca* 12 meV) and the energy distribution of our room temperature sample (30 to more than140 meV depending on the number of degrees of freedom of the molecule) were convoluted with the thermal energy distribution.

2.3.1   Fast dissociation

When the dissociation rate is fast, the E_0 for the lowest energy dissociation pathway is located at the energy at which the parent ion disappears. (See Figure 1-1)
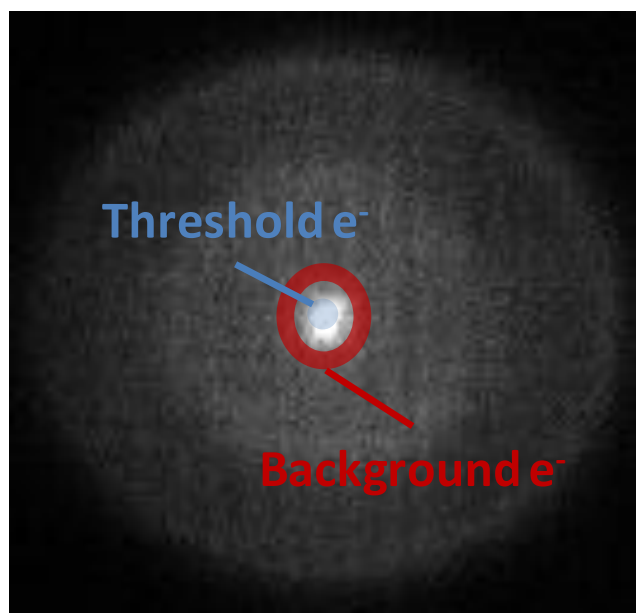
Figure 2- 6 Electron image with defined threshold (blue, center) and energetic background (red, ring) regions.

However, for large ions with many vibrational degrees of freedom, the internal energy distribution is broad and the precise energy at which the parent ion disappears is poorly defined. As a result, modeling is necessary to determine this 0 K dissociation energy. The ion internal energy, relative to the ground state of the ion, is given by $E_{ion}(h\nu) = h\nu - IE + E_{th}$, where IE is the adiabatic ionization energy and $h\nu$ is the photon energy. If $f_{Th}(E)$ is the normalized internal energy distribution of the ion, then the relative abundance of the parent ion, $BD_{parent}(h\nu)$, is determined by the portion of the ion internal energy distribution that lies below the 0 K dissociation threshold E_0:

$$BD_{parent}(h\nu) = \int_{0}^{E_o - h\nu} f_{Th}(E)dE \quad for\ h\nu < E_0$$

(2.3)

The relative fragment ion abundance is then

$$BD_{fragment}((h\nu) = 1 - BD_{parent}(h\nu)$$

(2.4)

When the photon energy exceeds E_0, the fractional parent and daughter ion signals remain 0 and 1, respectively. The neutral sample temperature is measured at the ionization region by a thermocouple. Thus, the E_0 can be determined by varying only a single parameter

2.3.2 Slow dissociation

For slow dissociations, kinetic information available in the TOF spectra, (see Figure 2-1 and Figure 2- 2) is modeled to determine the E_0. The ion internal energy distribution $f_{Th}(E_{Th})$ is taken into account when determining the relative abundances of the peaks in the TOF spectra as well as the asymmetric shape of the fragment peak. Figure 2- **7** shows that at a given photon energy the amount of parent detected slowly decreases as the ion internal energy, E_{Th}, and therefore $k(E)$, increases. The fractional

31
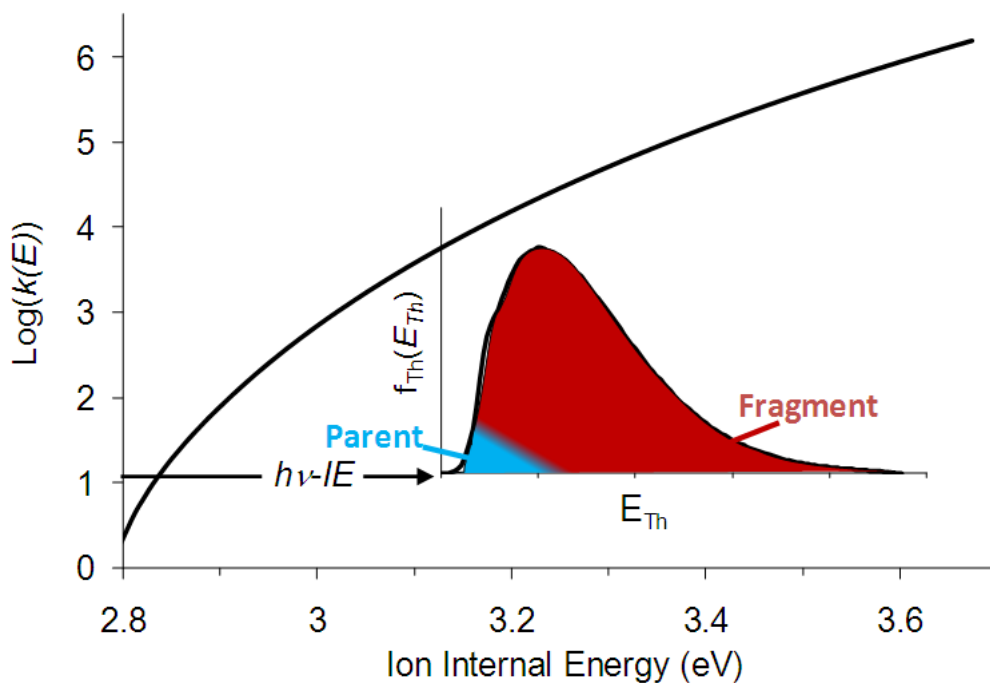
Figure 2- 7 The relative abundances of parent and fragment ion are determined by both the ion internal energy distribution f_{Th} and the rate curve $k(E)$. At a specific ion internal energy the parent abundance is determined by $k(E)$. To determine the $k(E)$ and relative abundances for all ion internal energies at a certain photon energy, these abundances are weighted by the internal energy distribution and summed. (eq. 2.6)

abundances, *A*, are determined by summing the parent ion decay and fragment ion growth over E_{Th}, weighted by $f_{Th}(E_{Th})$ as is shown by eq. 2.5 and 2.6.

$$A_{parent}(\tau) = \int_0^\infty f_{Th}(E_{Th})\exp[-k(h\nu + E_{Th} - IE)\tau]dE_{Th} \tag{2.5}$$

$$A_{fragment} = 1 - A_{parent} = \int_0^\infty f_{Th}(E_{Th})(1 - \exp[-k(h\nu + E_{Th} - IE)\tau])dE_{Th} \tag{2.6}$$

Where *k(E)* is the dissociation rate as a function of the ion internal energy measured relative to the ground state of the ion and τ *is* the time that the parent ion, after being formed, has to dissociate and still be detected as a fragment (*i.e.* the time required for the parent ion to travel from the ionization region to the end of the first drift region).

In the TOF spectra, the asymmetric fragment peak is modeled by calculating the TOF spectrum denoted by *F(E,t)*, for each *k(E)* over range of $f_{Th}(E_{Th})$ and summing these spectra weighted by $f_{Th}(E_{Th})$. The summed TOF spectrum, $F_{eff}(h\nu,t)$, is given by

$$F_{eff}(h\nu,t) = \int_0^\infty f_{Th}(E_{Th})F(h\nu + E_{Th} - IE,t)dE_{Th} \tag{2.7}$$

The E_0 is determined by adjusting the parameters that determine *k(E)* which, as is discussed in detail in chapter 4 depend upon the rate theory employed, to fit the experimental TOF distributions and breakdown diagram.

2.4 Computational Methods

2.4.1 Modeling

Molecular parameters used in the modeling of experimental data such as vibrational frequencies, rotational constants and geometries used in this paper were determined using the Gaussian 03[8] computer software. Geometry optimizations and

normal mode analyses, unless otherwise specified, were determined using the B3LYP hybrid functional with the 6-311++G(d,p) basis set for H, C, N, Cl and Br, and 6-311G(d,p) for iodine.[9,10] A scaling factor of 1 was used[11] for vibrational frequencies and anharmonicity corrections. For the molecules where internal rotations may have significant contributions to the molecular heat capacity, the Ayala-Schlegel[12] method was used to determine a correction to the harmonic treatment of these modes when determining H_{298}-H_0. Thermochemical values were calculated using the G3, W1, and CBS-APNO methods.

2.4.1.1 Ionization Energies

The adiabatic IE is the energy difference between the ground state of the ion and the ground state of the neutral. For fast dissociations, the IE_{ad} is not necessary because, as shown by eq. 2.3, the parent ion abundance is determined by the integral of f_{Th} (E_{Th}) from 0 to E_0-hv. For slow dissociations however, $k(E)$ must be calculated, where E is the ion internal energy relative to the ground state of the ion (*i.e.* hv-IE_{ad}+E_{Th}). Often an experimental value is available but sometimes the adiabatic IE must be calculated. Optimized the periodic table. The difference between the atomization energies of the ground and neutral states provides the adiabatic IE.

2.4.1.2 Calculated thermochemistry from isodesmic reactions.

We have supported several of our reported $\Delta_f H$ using high level energy calculations. The calculated atomization energies of molecules and ions of interest can be converted to heats of formation. However, there is some error in these values due to approximations built into the calculations. This error can be diminished using isodesmic

reactions. An isodesmic reaction is one where the products and reactants have the same number of the same types of bonds, an example is shown in eq. 2.8.

$$CH_3Cl + C_2H_5^+ \rightarrow CH_3^+ + C_2H_5Cl \qquad\qquad 2.8$$

In eq 2.8, both products and reactants have 8 H-C bonds, 1 C-Cl bond, and 1 C-C bond . This sort of "symmetry" results in a cancellation of the intrinsic error when the heat of reaction is determined. This heat of reaction is used in combination with experimentally determined heats of formation for the constituents to determine the heat of formation of the species of interest. By cleverly selecting reaction constituents that can be calculated to a high precision and also have high precision thermochemistry available, uncertainty in the desired heat of formation can be minimized.

Reference List

1. Fogleman, E. A.; Koizumi, H.; Kercher, J. P.; Sztáray, B.; Baer, T. The Heats of Formation of the Acetyl radical and Ion obtained by Threshold Photoelectron Photoion Coincidence, *J. Phys. Chem. A* **2004,** *108* , 5288-5294.

2. Baer, T.; Li, Y. Threshold Photoelectron Spectroscopy with Velocity Focusing: An Ideal Match for Coincidence Studies, *Int. J. Mass Spectrom.* **2002,** *219* , 381-389.

3. Kercher, J. P.; Stevens, W.; Gengeliczki, Z.; Baer, T. Modeling Ionic Unimolecular Dissociations from a Temperature Controlled TPEPCIO Study on 1-C_4H_9I ions, *Int. J. Mass Spectrom.* **2007,** *267* , 159-166.

4. Wiley, W. C.; McLaren, I. H. Time of flight mass spectrometer with improved resolution, *Rev. Sci. Instrum.* **1955,** *26* , 1150-1157.

5. Bodi, A.; Johnson, M.; Gerber, T.; Gengeliczki, Z.; Sztáray, B.; Baer, T. Imaging photoelectron photoion coincidence spectroscopy with velocity focusing electron optics, *Rev. Sci. Instrum.* **2009,** *80* , 034101-1-034101/7.

6. Johnson, M.; Bodi, A.; Schulz, L.; Gerber, T. New vacuum ultraviolet beamline at the Swiss Light Source for chemical dynamics studies, *Nucl. Instrum. Methods Phys. Res. A* **2009,** *610* , 597-603.

7. Bodi, A.; Sztáray, B.; Baer, T.; Johnson, M.; Gerber, T. Data acquisition schemes for continuous two-particle time-of-flight coincidence experiments, *Rev. Sci. Instrum.* **2007,** *78* , 084102-1-084102/7.

8. *Gaussian 03, Revision E.01,*Frisch, M. J.; Trucks, G. W.; Schlegel, H. B.; Scuseria, G. E.; Robb, M. A.; Cheeseman, J. R.; Montgomery, J. A.; Vreven, T.; Kudin, K. N.; Burant, J. C.; Millam, J. M.; Iyengar, S. S.; Tomasi, J.; Barone, V.; Mennucci, B.; Cossi, M.; Scalmani, G.; Rega, N.; Petersson, G. A.; Nakatsuji, H.; Hada, M.; Ehara, M.; Toyota, K.; Fukuda, R.; Hasegawa, J.; Ishida, M.; Nakajima, T.; Honda, Y.; Kitao, O.; Nakai, H.; Klene, M.; Li, X.; Knox, J. E.; Hratchian, H. P.; Cross, J. B.; Adamo, C.; Jaramillo, J.; Gomperts, R.; Stratmann, F.; Yazyev, O.; Austin, A. J.; Cammi, R.; Pomelli, C.; Ochterski, J. W.; Ayala, P. Y.; Morokuma, K.; Voth, G. A.; Salvador, P.; Dannenberg, J. J.; Zakrzewski, V. G.; Dapprich, S.; Daniels, A. D.; Strain, M. C.; Farkas, Ö.; Malick, D. K.; Rabuck, A. D.; Raghavachari, K.; Foresman, J. B.; Ortiz, J. V.; Cui, Q.; Baboul, A. G.; Clifford, S.; Cioslowski, J.; Stefanov, B. B.; Liu, G.; Liashenko, A.; Piskorz, P.; Komáromi, I.; Martin, R. L.; Fox, D. J.; Keith, T.; Al-Laham, M. A.; Peng, C. Y.; Nanayakkara, A.; Challacombe, M.; Gill, P. M. W.; Johnson, B.; Chen, W.; Wong, M. W.; Gonzalez, C.; Pople, J. A. Gaussian, Inc.: Wallingford, CT, 2004.

9. Feller, D. The role of databases in support of computational chemistry calculations, *J. Comp. Chem.* **1996,** *17* , 1571-1586.

10. Schuchardt, K. L.; Didier, B. T.; Elsethagen, T.; Sun, L.; Gurumoorthi, V.; Chase, J.; Li, J.; Windus, T. L. Basis Set Exchange: A Community Database for Computational Sciences, *J. Chem. Inf. Mod.* **2007,** *47* , 1045-1052.

11. Merrick, J. P.; Moran, D.; Radom, L. An Evaluation of Harmonic Vibrational Frequency Scale Factors, *J. Phys. Chem. A* 2007, *111* , 11683-11700.

12.   Ayala, P. Y.; Schlegel, H. B. Identification and treatment of internal rotation in normal mode vibrational analysis, *J. Chem. Phys.* 1998, *108* , 2314-2325.

CHAPTER 3: Photodissociation of $C_3H_8^+$ observed by iPEPICO:

Accurate Heats of Formation of i-$C_3H_7^+$, i-C_3H_7Cl i-C_3H_7Br, and i-C_3H_7I

3.1   Introduction

Due to its stability, the isopropyl ion is a common product of the dissociative photoionization of alkanes. However, a reliable high accuracy determination of its heat of formation has yet to be determined.   One route to determining $\Delta_f H°(i$-$C_3H_7^+)$ is via dissociative photoionization:

$$i\text{-}C_3H_7X + h\nu \rightarrow i\text{-}C_3H_7^+ + X + e^- \text{ (X=H, Cl, Br, I)} \qquad\qquad 3\text{-}1$$
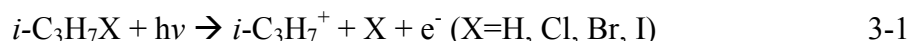
It is known that these systems have stable parent ions that rapidly dissociate to form i-$C_3H_7^+$ which makes determination of their photoionization onset relatively easy.

The 298 K photodissociation of C_3H_8 to form i-$C_3H_7^+$ was first observed by Steiner *et al.*[1] in 1961 and measured again by Chupka and Berkowitz[2] in 1967 using photoionization mass spectrometry (PIMS). The 298 K appearance energy (AE_{298}) of 11.53 ± 0.01 eV reported by Steiner[1] appears to be quite reasonable, however the extrapolated AE_0 was significantly underestimated in both of these studies. The photodissociation of the isopropyl halides have been reported several times but the derived $\Delta_f H°(i$-$C_3H_7^+)$ are scattered over nearly 10 kJ•mol^{-1}.[3-6] The first study was by

Traeger[3] in 1980 using PIMS which yielded a value for $\Delta_f H_{298}(i\text{-}C_3H_7^+)$ of 802.5 ± 1.7 kJ•mol^{-1}.[7] However, the onsets in these measurements are poorly defined and the uncertainty is believed to be underestimated. In 1982, Rosenstock *et al* used photoelectron-photoion coincidence (PEPICO) spectroscopy to report a $\Delta_f H^{\circ}_{298}(i\text{-}C_3H_7^+)$ of 798.8 ± 2 kJ•mol^{-1} from the 0 K photoionization onset of $i\text{-}C_3H_7Br$.[4] In this study, it was reported that the dissociation was metastable which has not been observed in subsequent studies. Accounting for a nonexistent kinetic shift would certainly cause the determined $\Delta_f H^{\circ}_{298}(i\text{-}C_3H_7^+)$ to be underestimated. In 2000, the 0 K dissociation onsets (E_0) of isopropyl ion from isopropyl chloride, isopropyl bromide and isopropyl iodide were measured using pulsed field ionization-photoelectron photoion coincidence spectroscopy (PFI-PEPICO) by Baer *et al*[5] to be 11.085 ± 0.005 eV, 10.505 ± 0.008 eV and 9.851 ± 0.025 eV. This resulted in a composite $\Delta_f H^{\circ}_{298}(i\text{-}C_3H_7^+)$ of 807.7 ± 1.5 kJ•mol^{-1}. However, as pointed out recently,[8] these experiments were plagued by dimers which caused the reported onsets to be too high. In 2004 Brooks *et al*[6] reported a value of 803.9 ± 1.5 kJ•mol^{-1} using threshold photoelectron-photoion coincidence spectroscopy (TPEPICO) to determine the photoionization onset of isopropyl ion from isopropyl chloride. In this study, the sample was not cooled in an expansion, eliminating the possibility of dimer formation. However, it was recently determined that the photon energies of the isopropyl chloride data were not properly calibrated and, as a result, reported a 0K dissociation onset (and therefore $\Delta_f H(i\text{-}C_3H_7^+)$) that was 0.030 meV too low.

Another possible route to $\Delta_f H^{\circ}(i\text{-}C_3H_7^+)$ is measurement of the ionization energy of the isopropyl radical. In 1979 Houle and Beauchamp measured the $IE(i\text{-}C_3H_7)$ to be

7.36 ± 0.02 eV.[9] This value was later confirmed by Dyke *et al.*[10] Beauchamp, relying upon $\Delta_f H^\circ(i\text{-}C_3H_7)$, reported a value of 783 ± 4.6 kJ•mol[-1] for $\Delta_f H^\circ(i\text{-}C_3H_7{}^+)$. A value for $\Delta_f H^\circ(i\text{-}C_3H_7)$ that was too low, in combination with the $IE(i\text{-}C_3H_7)$ being underestimated due to hot bands in the observed photoelectron spectra, caused Beauchamp's reported value for $\Delta_f H^\circ(i\text{-}C_3H_7{}^+)$ to be lower than subsequent photoionization studies by nearly 20 kJ•mol[-1].

The proton affinity of propene plays an important role in calibrating the proton affinity scale. The heats of formation of H^+ and C_3H_6 are very well known.[11] Most of the uncertainty in $PA(C_3H_8)$ is therefore due to the $\Delta_f H^\circ{}_{298}(i\text{-}C_3H_7{}^+)$. As a result of the scatter in $\Delta_f H^\circ{}_{298}(i\text{-}C_3H_7{}^+)$, $PA(C_3H_8)$ has oscillated between 746 kJ•mol[-1] and 743 kJ•mol[-1].

Calculations can also be used to determine $\Delta_f H^\circ{}_{0\,K}(i\text{-}C_3H_7{}^+)$. Lau and Ng[12] have recently determined values of 90.0 and 806.4 kJ•mol[-1] for the isopropyl radical and ion 298 K heats of formation at the CCSD(T)/CBS level. These values appear to be within the scatter of previously reported values. The 0 K values provide an ionization energy of 7.437 eV, significantly higher than the experimentally observed IE.[9,10]

3.2   Results

The data are shown in the forms of threshold photoelectron spectra (Figure 3- 3 through Figure 3- 4) and breakdown diagrams (Figure 3-5 through Figure 3-8) for C_3H_8, $i\text{-}C_3H_7Cl$, $i\text{-}C_3H_7Br$ and $i\text{-}C_3H_7I$. It is shown in Figure 3-5 that the formation of $i\text{-}C_3H_7{}^+$ is the lowest energy dissociation channel for propane. The breakdown diagrams for the isopropyl halides (Figure 3- 6 through Figure 3- 8) show that the only fragment ion formed over the energy range of interest is $i\text{-}C_3H_7{}^+$. For all compounds studied it was
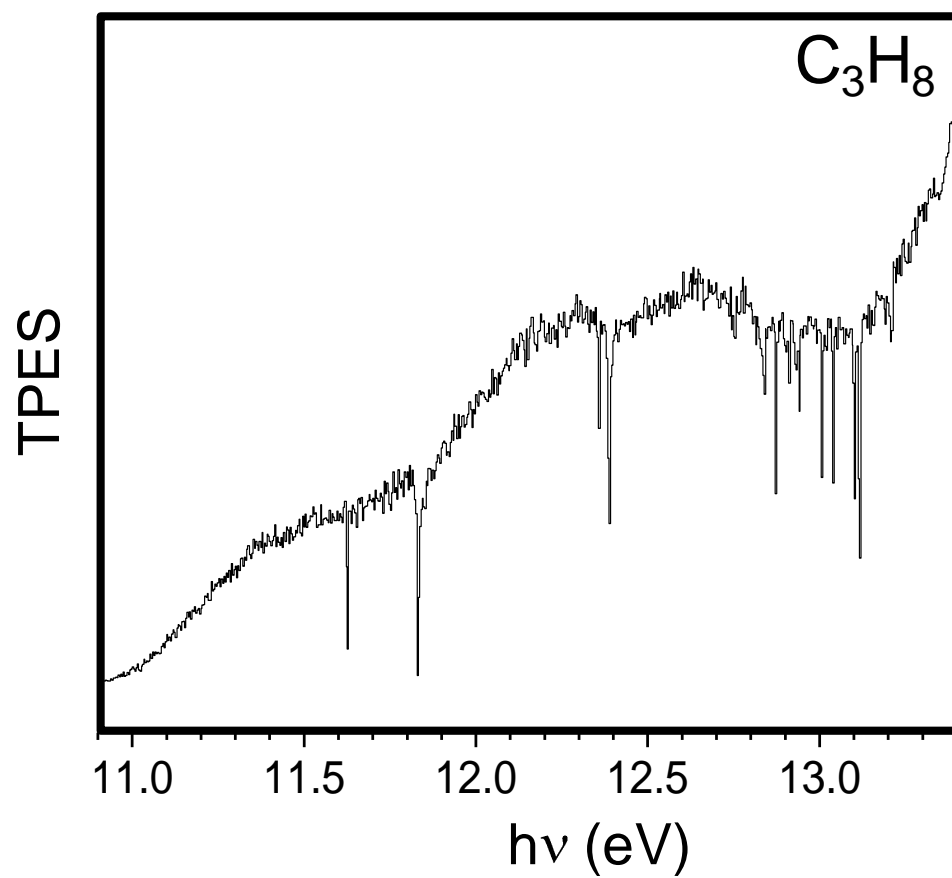
Figure 3- 1 Propane TPES
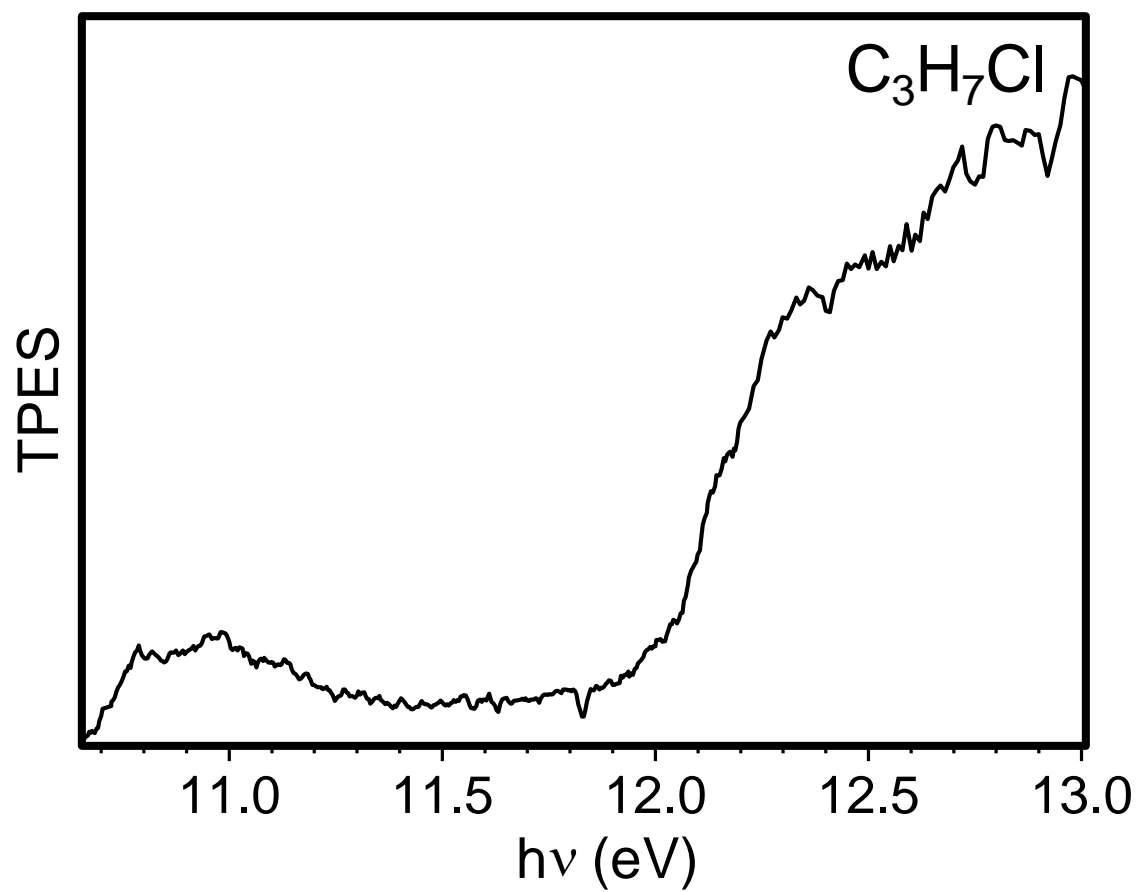
Figure 3- 2 *i*-C_3H_7Cl TPES
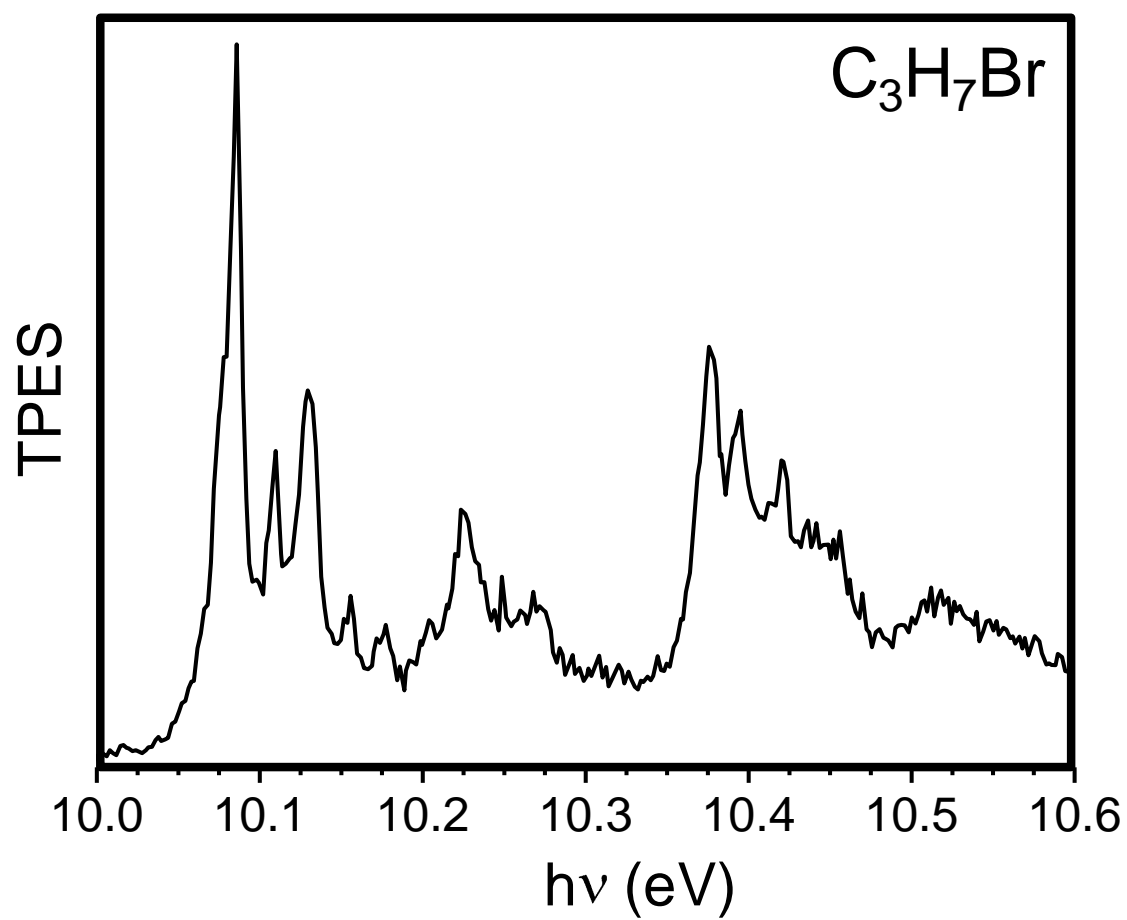
Figure 3- 3 TPES of *i*-C₃H₇Br

C$_3$H$_7$I
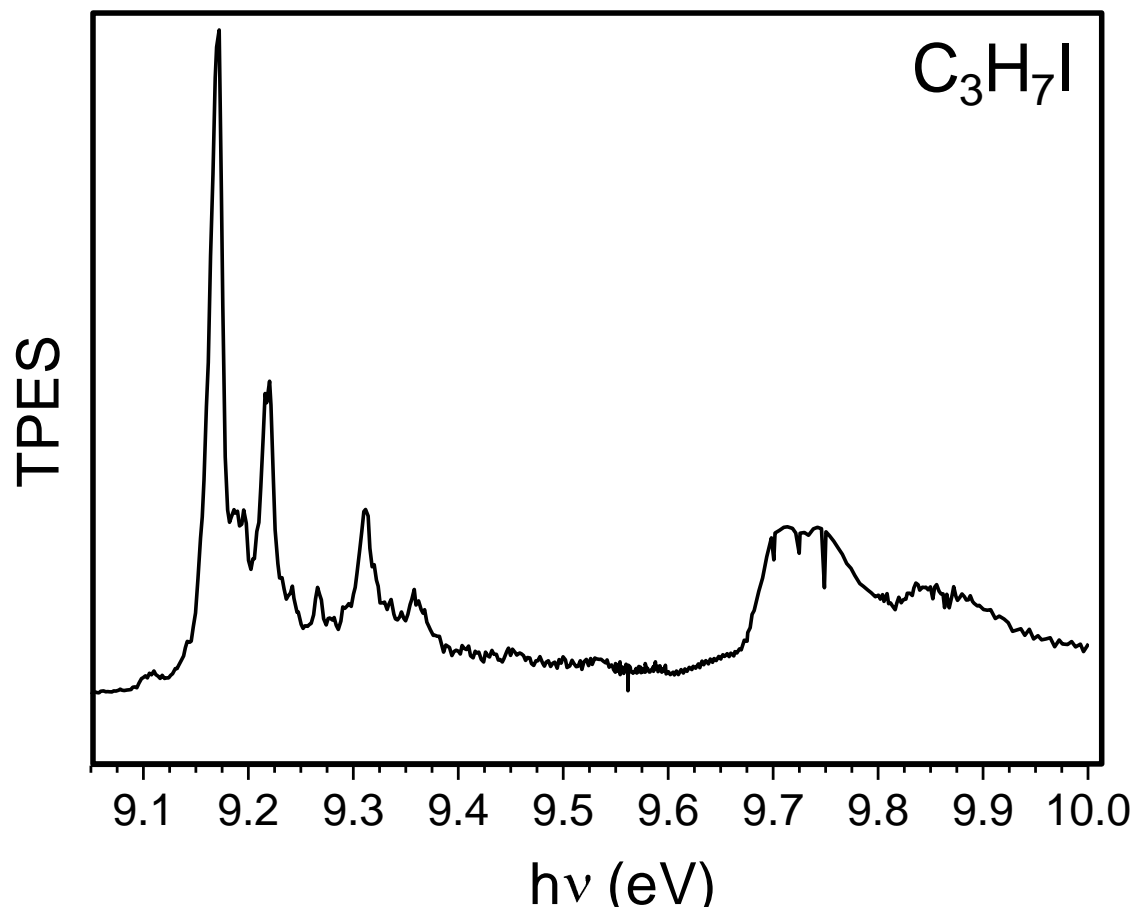
Figure 3- 4 TPES of i-C$_3$H$_7$Br
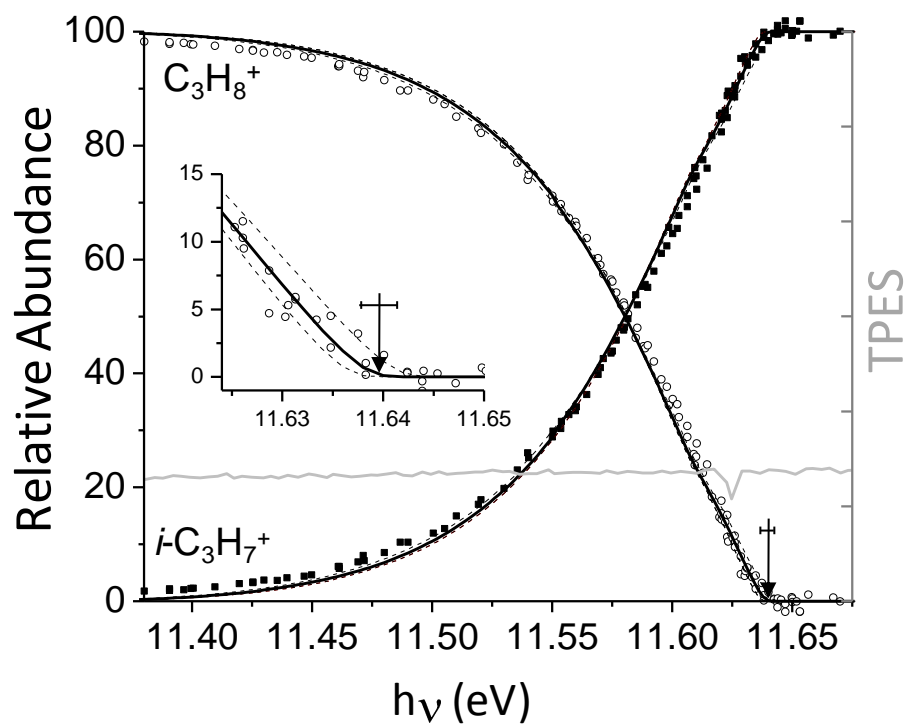
Figure 3- 5 Breakdown Diagram for $C_3H_8^+$. The open circles indicate the $C_3H_8^+$ abundance and the solid squares represent i-$C_3H_7^+$ abundance. The inset is an expanded view of the breakdown diagram near the E_0.
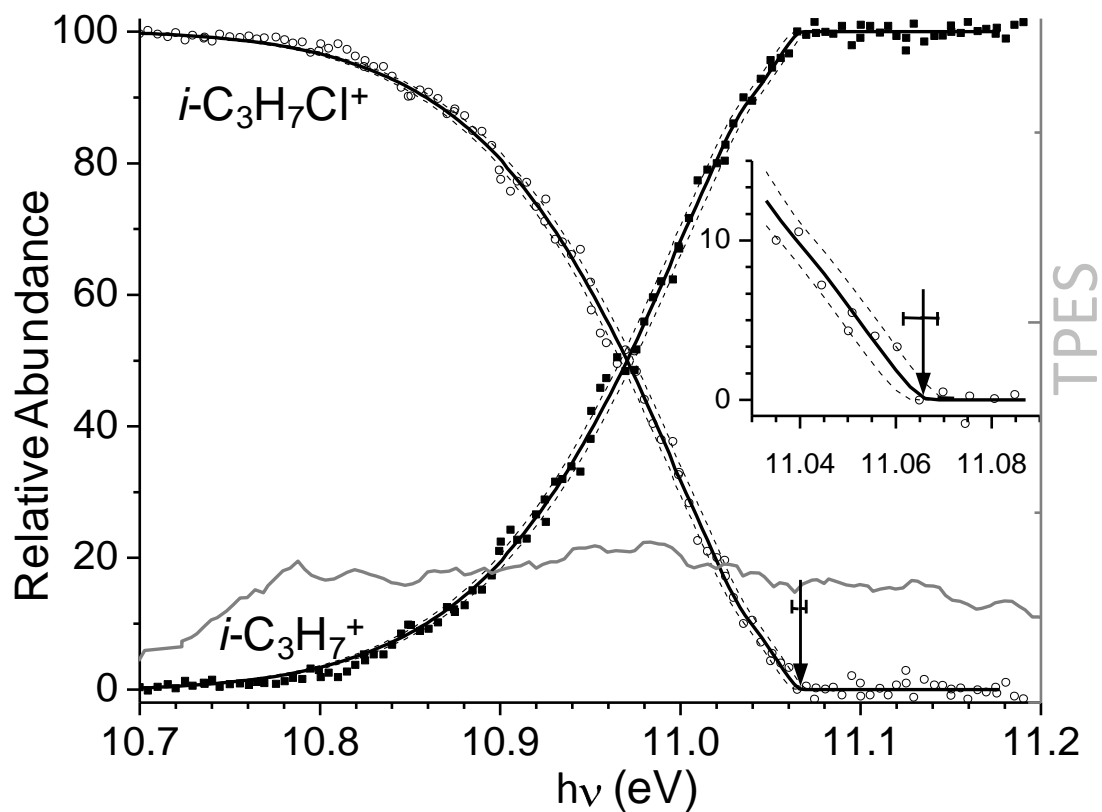
Figure 3- 6 Breakdown Diagram for i-$C_3H_7Cl^+$. The open circles indicate the of the i-$C_3H_7Cl^+$ abundance and the solid squares represent i-$C_3H_7^+$ abundance. The inset is an expanded view of the breakdown diagram near the E_0. The grey line indicates the threshold photoelectron spectrum (arbitrary units).
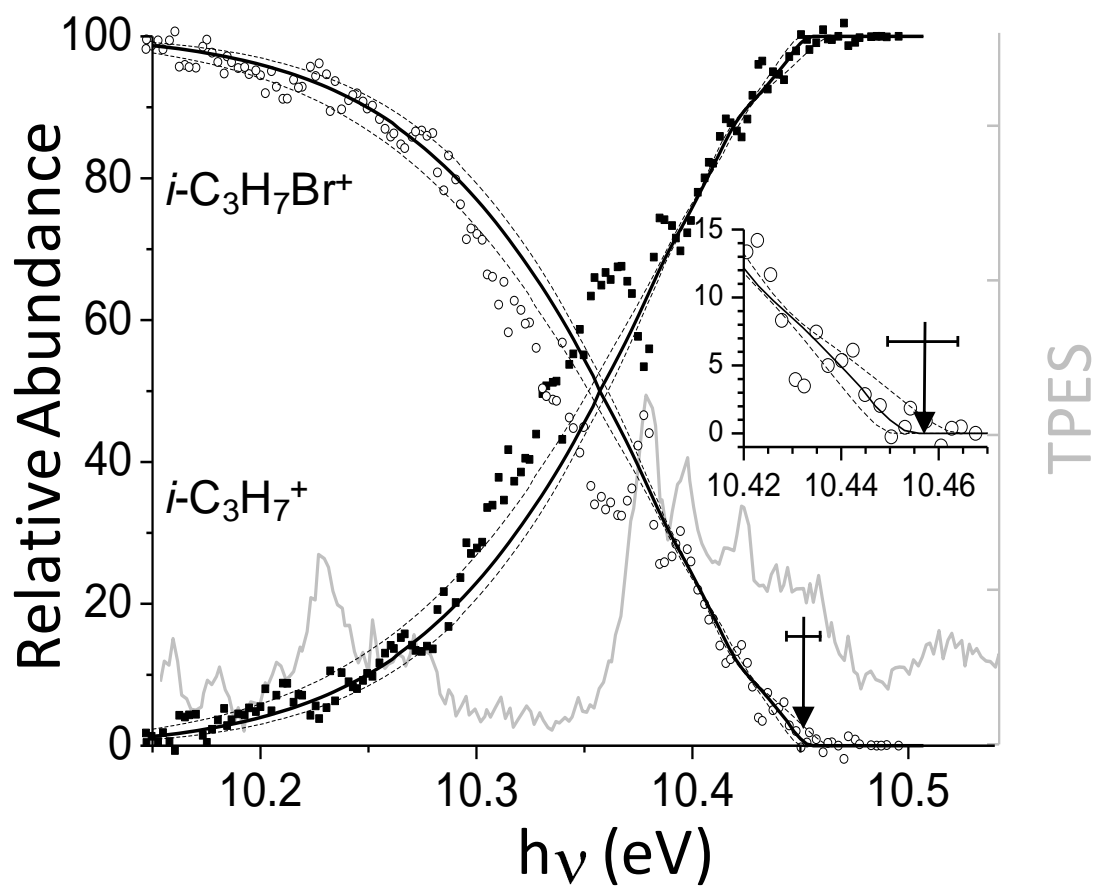
Figure 3- 7 Breakdown Diagram for i-$C_3H_7Br^+$. The open circles indicate the of the i-$C_3H_7Br^+$ abundance and the solid squares represent i-$C_3H_7^+$ abundance. The inset is an expanded view of the breakdown diagram near the E_0. The grey line indicates the threshold photoelectron spectrum (arbitrary units).
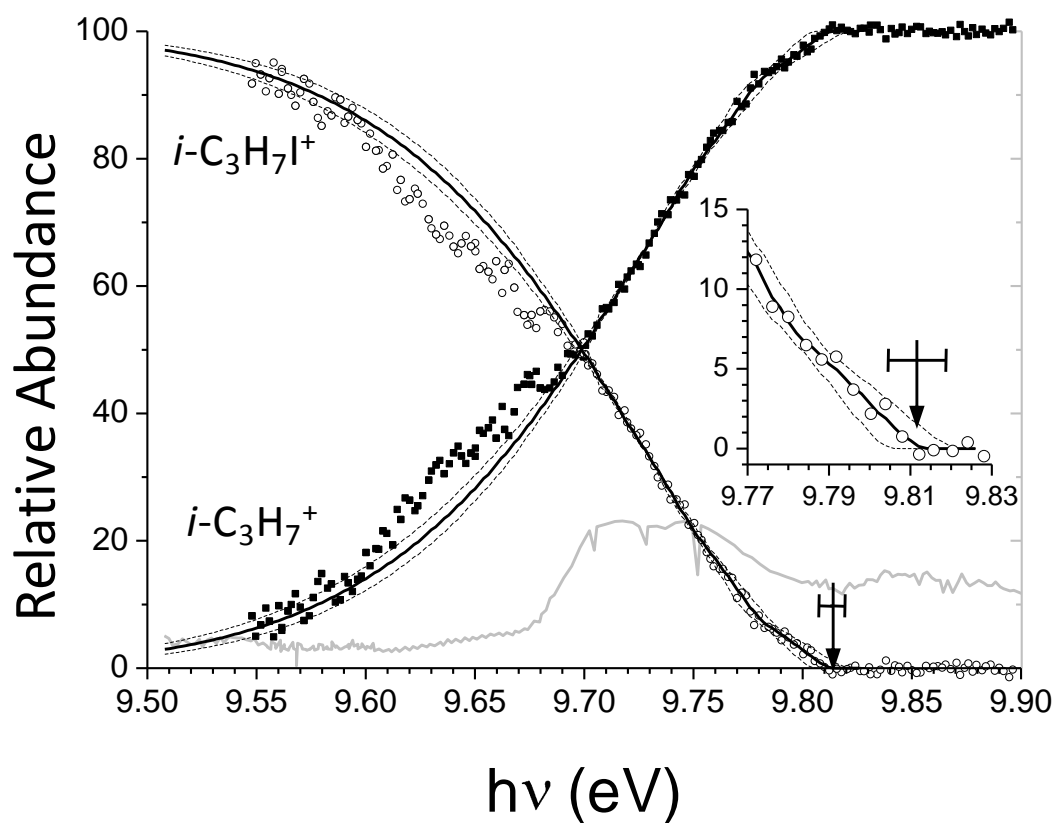
Figure 3- 8 Breakdown Diagram for i-$C_3H_7I^+$. The open circles indicate the of the i-$C_3H_7I^+$ abundance and the solid squares represent i-$C_3H_7^+$ abundance. The inset is an expanded view of the breakdown diagram near the E_0. The grey line indicates the threshold photoelectron spectrum (arbitrary units).

observed that the i-$C_3H_7^+$ peaks in the TOF spectra were symmetric at low energies, indicating that the dissociation rates for i-$C_3H_7^+$ formation were faster than the timescale of our apparatus ($k(E) > 10^7$ s^{-1}).

The improved energy resolution of the iPEPICO apparatus reveals some structure in the breakdown diagrams for i-C_3H_7Br and i-C_3H_7I. Similar features have been observed in the case of CH_3I.[8] In Figure 3- 7 and Figure 3- 8 the i-C_3H_7Br and i-C_3H_7I abundance is lower than expected in the region of the Franck-Condon gaps in the TPES. The production of threshold electrons in Franck-Condon gaps is not well understood. Guyon *et al* [13] and Chupka *et al*[14] proposed a mechanism that relies upon the existence of long-lived neutral Rydberg states. Because there is a quasi continuum of these Rydberg states converging to various ion states, it is possible for the neutral molecule to absorb a photon and access these neutral Rydberg states in regions where the probability of direct ionization is low (*i.e.* a Franck-Condon Gap). From these states the neutral molecule can cross over to a neutral dissociative surface. As the molecule dissociates the molecule may cross over to a lower energy ion state, generating a threshold electron. Because energy must be conserved, the kinetic energy of the dissociating neutral fragments becomes vibrational energy in the ion. It was suggested in the study of CH_3I that the warmer ion internal energy distribution observed as an increase in fragment ion abundance, is a result of this process being aided by rotational excitation.[8] A similar effect appears operatie in the isopropyl halide ion dissociation. Observed in Figure 3- 8 are peaks in the i-C_3H_7Br abundance that coincide perfectly with peaks in the TPES. Most notable is the peak at 10.35 eV. When a neutral molecule is excited to a Rydberg state that is close in energy to an ion state, the Rydberg molecule can autoionize and generate a threshold electron.

49

However rotationally excited neutral molecules can also begin to dissociate, the majority of which will not form a threshold electron. This results in a warmer ion internal energy distribution observed as an increase in fragment ion abundance. It is important to mention that, because the dissociation is fast, these features do not shift the location of the E_0.

When the dissociation rate is fast, the E_0 for the lowest energy dissociation pathway is located at the energy where the parent ion disappears. To precisely determine the E_0, modeling is necessary. The ion internal energy, relative to the ground state of the ion, is given by $E_{ion}(h\nu) = h\nu - IE + E_{th}$, where *IE* is the adiabatic ionization energy and $h\nu$ is the photon energy. If *P(E)* is the normalized thermal energy distribution of the ion, then the relative abundance of i-$C_3H_7X^+$, $BD_{C3H7X}(h\nu)$, is determined by the portion of the ion internal energy distribution that lies below the 0 K dissociation threshold $E_0(i$-$C_3H_7^+)$ (See Figure 1-1):

$$BD_{C_3H_7X}(h\nu) = \int_0^{E_o - h\nu} P(E)dE \quad for \ h\nu < E_0 \tag{3.2}$$

The relative fragment ion abundance is then

$$BD_{C_3H_7^+}(h\nu) = 1 - BD_{C_3H_7X}(h\nu) \tag{3.3}$$

When the photon energy exceeds the E_0, the fractional parent and daughter ion signals remain 0 and 1, respectively. We use the neutral frequencies here to determine the ion internal energy distribution. The internal energy distribution of the neutral molecule is often faithfully transposed to the ionic manifold upon ionization.[15] However, this is not always the case and the temperature is therefore used as a fitting parameter. The best fit onset for C_3H_8 was 11.639 ± 0.002 eV with a Temperature of 270 ± 15 K. For i-C_3H_7Cl and i-C_3H_7Br, the best fit onsets were 11.064 ± 0.004 and 10.454 ± 0.008

eV with best fit temperatures of 305 ±10 K and 298 ± 20 K, respectively. The larger

uncertainty in the temperature for i-C_3H_7Br is due to the enhanced structure in the

breakdown diagram. For i-C_3H_7I, the best fit E_0 and temperature was 9.812 ± 0.008 eV

and 320 ± 15 K. The elevated temperature of the ion internal energy distribution may be a

result of the Franck-Condon gap coinciding with a large portion of the breakdown

diagram. The reported E_0 for i-C_3H_7I is within the experimental error of the previous

TPEPICO measurement by Baer $et~al$[16] (9.818 ± 0.010 eV) and slightly lower than the

laser based MATI value of 9.818 ± 0.004 eV.[17] Table 3-1 summarizes the current and

previously measured onset energies.

Table 3-1. **Comparison of $E_0(i$-$C_3H_7^+)$ with previous values.**

	E_0	AE_{298}	AE_0-AE_{298}
C_3H_8	11.64 ± 0.03[a]	11.58 ± 0.03[b]	0.11
	11.63 ± 0.01[a]	11.52 ± 0.02[c]	
	$\mathbf{11.639 \pm 0.002}$[d]		
i-C_3H_7Cl	11.05 ± 0.02[a]	10.92[e]	0.13
	11.085 ± 0.005[f]		
	11.036 ± 0.010[g]		
	$\mathbf{11.065 \pm 0.004}$[d]		
i-C_3H_7Br	10.47 ± 0.02[a]	10.33[e]	0.14
	10.42 ± 0.01[g]		
	10.505 ± 0.020[f]		
	$\mathbf{10.454 \pm 0.008}$[d]		
i-C_3H_7I	9.84 ± 0.02[a]	9.7[e]	0.14
	9.77 ± 0.02[h]		
	9.851 ± 0.025[f]		
	9.8180 ± 0.0036[i]		
	$\mathbf{9.818 \pm 0.010}$[d]		

[a]These values were converted from an AE_{298} by adding AE_0-$AE_{298}=<E_{rot}>+<E_{vib}>$.
[b]Steiner $et~al.$ 1961[1]; [c]Chupka 1967[2,2-6]; [d]This work; [e]Traeger 1980[3]; [f]Baer $et~al$ 2000[5];
[g]Brooks $et~al$ 2004[6]; [h]Rosenstock $et~al$ 1982[4]; [i]Kim $et~al$[17]

3.3 Derived Thermochemistry of i-$C_3H_7^+$, i-C_3H_7Cl i-C_3H_7Br and i-C_3H_7I

In the absence of a reverse barrier, the E_0 is equal to the thermochemical onset. That is,

$$E_0 = \Delta_f H_{0K}^{\circ}(i\text{-}C_3H_7^+) + \Delta_f H_{0K}^{\circ}(X) - \Delta_f H_{0K}^{\circ}(i\text{-}C_3H_7X) \qquad (3.3)$$

where X = H, Cl, Br, and I. Thus, the uncertainty in $\Delta_f H(i\text{-}C_3H_7^+)$ is dependent upon the uncertainty in the $\Delta_f H^{\circ}_{0K}(i\text{-}C_3H_7X)$, $\Delta_f H^{\circ}_{0K}(X)$, and E_0. The 298 K heats of formation of C_3H_8, i-C_3H_7Cl, i-C_3H_7Br, and i-C_3H_7I reported in the literature must be converted to 0 K heats of formation. This requires the H_0-H_{298} of the constituents of the formation reaction. The H_0-H_{298} for $H_{2\,(g)}$, $Cl_{2\,(g)}$, $Br_{2\,(g)}$, I_2 and $C_{(s)}$ are reported by Chase,[11] but the H_0-H_{298} for i-C_3H_7X must be calculated. Usually, H_{298}-H_0 is calculated using the harmonic oscillator-rigid rotor approximation. However these molecules contain two methyl groups which should be treated as hindered rotors. To account for this we use the method outlined by Ayala and Schlegel[18] to calculate a correction to the H_0-H_{298} determined using the rigid rotor-harmonic oscillator approximation. These corrections were 0.34, 0.24, 0.24, and 0.22 kJ•mol^{-1} for C_3H_8, i-C_3H_7Cl, i-C_3H_7Br, and i-C_3H_7I. The values determined for H_0-H_{298} and $\Delta_f H^{\circ}_{0K}$ (i-C_3H_7X) are listed in Table 3-2 From i-C_3H_7Cl, i-C_3H_7Br, and i-C_3H_7I the $\Delta_f H^{\circ}_{0K}(i\text{-}C_3H_7^+)$ was determined to be 823.9 ± 1.4 kJ•mol^{-1}, 819.3 ± 2.5 kJ•mol^{-1}, and 821.3 ± 3.9 kJ•mol^{-1} respectively. The value for $\Delta_f H^{\circ}_{0\,K}(i\text{-}C_3H_7^+)$ determined from propane is known better than the heats of formation of the isopropyl halides. We can therefore use Eqn. 3.3 and the reported $\Delta_f H^{\circ}_{0K}(i\text{-}C_3H_7^+)$ to determine more precise values for these molecules. These values are determined to be -144.2 ± 0.7 kJ•mol^{-1}, -94.1 ± 0.9 kJ•mol^{-1}, and -37.0 ± 0.9 kJ•mol^{-1} for i-C_3H_7Cl, i-C_3H_7Br, and i-C_3H_7I respectively.

Table 3-2 Derived and Ancillary Thermochemical Values (kJ•mol^{-1})

	$\Delta_f H_{298K}$	$\Delta_f H_{0K}$	H_0-H_{298}
C_3H_8	-104.7 ± 0.5^b	-82.4 ± 0.5	14.70
i-C_3H_7Cl	$\mathbf{-144.2 \pm 0.7^a}$	$\mathbf{-123.4 \pm 0.7}$	16.57
i-C_3H_7Br	$\mathbf{-94.1 \pm 0.9^a}$	$\mathbf{-66.2 \pm 0.9}$	17.07
i-C_3H_7I	$\mathbf{-37.0 \pm 0.9^a}$	$\mathbf{-15.0 \pm 0.9}$	17.32
H		216.035^b	
Cl		119.621^b	
Br		117.92^b	
I		107.161^b	
H$^+$	1530.049^d		
i-C_3H_7	20.0 ± 0.7^e		15.86
i-$C_3H_7{}^+$	$\mathbf{807.4 \pm 0.5^{a,f}}$	$\mathbf{824.6 \pm 0.5^{a,f}}$	15.57
$PA_{298}(C_3H_6)$	$\mathbf{742.7 \pm 0.8^a}$		

[a]**This Work**; [b]Pittam 1972;[19] [c]Pedley 1994;[20] [d]Chase 1998;[21] [e]Seakins *et al* 1992;[22] [f]Determined using the convention that excludes the enthalpy of an electron at room temperature.

3.3.1 Isodesmic Calculations of i-C3H7$^+$

In support of the experimentally derived i-$C_3H_7{}^+$ heat of formation, we calculated

the G3, CBS-APNO, and W1 energies for the following isodesmic reactions:

$$C_3H_8 + \begin{pmatrix} CH_3^+ \\ C_2H_5^+ \end{pmatrix} \rightarrow \left(i\text{-}C_3H_7^+\right) + \begin{pmatrix} CH_4 \\ C_2H_6 \end{pmatrix}$$

$$\left(i\text{-}C_4H_{10}\right) + \begin{pmatrix} CH_3^+ \\ C_2H_5^+ \end{pmatrix} \rightarrow \left(i\text{-}C_3H_7^+\right) + \begin{pmatrix} C_2H_6 \\ C_3H_8 \end{pmatrix}$$
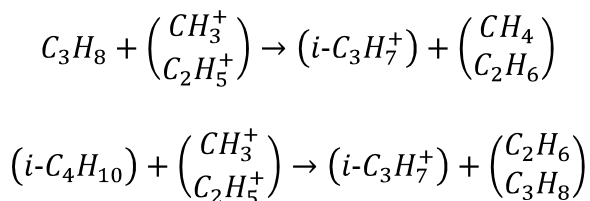
The i-$C_3H_7{}^+$ heat of formation is determined from the calculated reaction energy and the

experimental heats of formation for the other reaction constituents. The methane heat of

formation[23] and the corresponding E_0(CH$_4$ $\rightarrow$ CH$_3{}^+$ + H)[24] are very well known and

provide a value of 1099.37 $\pm$ 0.1 kJ•mol^{-1} for $\Delta_f H^o{}_{0K}(CH_3{}^+)$. The heats of formation of

the neutral hydrocarbons are all reported by Pedley[20] to within 1 kJ•mol^{-1}.

Table 3-3 shows the $\Delta_f H^o{}_{0K}(i\text{-}C_3H_7{}^+)$ determined by calculations of the above

isodesmic reaction energies. The G3 values are the least expensive calculation and

provides results that agree with each other to within 4 kJ•mol^{-1}, yielding an average value

of xxx. The W1 and CBS-APNO results provide values in better agreement with each

other as well as in much better agreement with the experimental value of 823.9 $\pm$ 1.4

kJ•mol^{-1}. The average of the W1 and CBS-APNO calculations is 825.1$\pm$ 1.0 kJ•mol^{-1}.

These results rely upon the accuracy of the experimentally determined heats of formation

of the reaction constituents. It is observed that the values for $\Delta_f H^o{}_{0K}(i\text{-}C_3H_7{}^+)$ determined

for Y=C$_2$H$_5$ are 1kJ•mol^{-1} higher than the values determined for Y=CH$_3$. The methyl ion

heat of formation is known much better than the ethyl. As a result, the ethyl ion heat of

formation may require further study. This value is difficult to obtain experimentally due

to the dearth of systems that dissociate simply to form ethyl ion. This ion is small and is

closed shell, thus making it a good candidate for state of the art *ab initio* calculations

such as W4[25] or HEAT[26].

Table 3-3. $\Delta_f H^o{}_{0K}(i\text{-}C_3H_7{}^+)$ determined from *ab initio* isodesmic reaction energies (kJ•mol^{-1}) for the reaction: $i\text{-}C_3H_7\text{-}X + Y+ \rightarrow i\text{-}C_3H_7+ + XY$

Y	Method	X = H	X = CH$_3$
CH$_3$	G3	828.8	828.0
	CBS-APNO	823.5	825.3
	W1	824.7	
C$_2$H$_5$	G3	824.0	824.0
	CBS-APNO	826.2	826.0
	W1	825.2	

3.3.2 Ionization Energy of i-C_3H_7 and Proton Affinity of C_3H_6

The adiabatic ionization energy of the i-C_3H_7 can be determined from the 0 K heats of formation of the isopropyl ion and radical. Bodi et al[27] reported the $\Delta_fH^{\circ}_{298K}(i$-$C_3H_7)$ to be 90 ± 1.7 kJ•mol^{-1}. With a hindered rotor correction[18] of -0.31 kJ•mol^{-1} the H_0-H_{298} was calculated to be 15.57 kJ•mol^{-1}. Using this value, a $\Delta_fH^{\circ}_{0K}(i$-$C_3H_7)$ of 106.9 kJ•mol^{-1} is determined. Using the experimentally determined value for $\Delta_fH^{\circ}_{0K}(i$-$C_3H_7^+)$ the IE(i-C_3H_7) was determined to be 7.438 ± 0.020 eV. This is in excellent agreement with the theoretical IE(i-C_3H_7) of 7.436 eV calculated by Lau and Ng[12]. This value disagrees, however with previous attempts to measure the adiabatic ionization energy from photoelectron spectra by Houle and Beauchamp[9] and by Dyke et al[10]. This is not surprising as the first peak in the PES of isopropyl radical is very small and broad due to poor Franck-Condon factors at threshold.

The absolute proton affinity of propene can be determined by converting the 0K heat of formation of the isopropyl ion to 298 K. The hindered rotor correction was determined to be 0.32 kJ•mol^{-1} with a value of H_{298}-H_0 of 15.57 kJ•mol^{-1}, the $\Delta_fH^{\circ}_{298K}(i$-$C_3H_7^+)$ is determined to be 806.7 ± 1.4 kJ•mol^{-1}. Using this value, we calculate a $PA_{298}(C_3H_6)$ of 743.4 ± 1.5 kJ•mol^{-1}. This value is in excellent agreement with the composite value reported by Meot-Ner[28] of 743.4 ± 1.3 kJ•mol^{-1} who took a simple average of relative PA_{298}'s reported by Szulejko and McMahon,[29] Meot-Ner and Sieck,[30] and Smith and Radom.[31]

3.4 Conclusions

$\Delta_f H^o{}_{0K}(i\text{-}C_3H_7{}^+)$ has been determined to be 824.6 ± 0.6 kJ•mol^{-1} from measurement of the $E_0(i\text{-}C_3H_7{}^+)$ by modeling TPEPICO breakdown diagram of propane. Breakdown diagrams were also modeled for $i\text{-}C_3H_7Cl$, $i\text{-}C_3H_7Br$, and $i\text{-}C_3H_7I$ and the $E_0(i\text{-}C_3H_7{}^+))$ was determined for each species. Using the currently determined value for $\Delta_f H^o{}_{0K}(i\text{-}C_3H_7{}^+)$, $\Delta_f H^o{}_{298K}(i\text{-}C_3H_7Cl)$, $\Delta_f H^o{}_{298K}(i\text{-}C_3H_7Br)$ and $\Delta_f H^o{}_{298K}(i\text{-}C_3H_7I)$ were determined to be -144.9 ± 0.7 kJ•mol^{-1}, -94.1 ± 1.0 kJ•mol^{-1} and -37.0 ± 1.0 kJ•mol^{-1}, respectively. The new value for $\Delta_f H^o{}_{0K}(i\text{-}C_3H_7{}^+)$ corresponds to an IE($i\text{-}C_3H_7$) of 7.438 ± 0.020 eV which is in good agreement with the theoretical value of Lau and Ng.[12] Using the $\Delta_f H^o{}_{298K}(i\text{-}C_3H_7{}^+)$, the PA$_{298}$(C$_3H_6$) was determined to be 742.7 ± 0.9 kJ•mol^{-1}.

Reference List

1. Steiner, B. W.; Giese, C. F.; Inghram, M. G. Photoionization of alkanes. Dissociation of excited molecular ions, *J. Chem. Phys.* **1961,** *34* , 189-220.

2. Chupka, W. A.; Berkowitz, J. Photoionization of ethane, propane, and n-butane with mass analysis, *J. Chem. Phys.* **1967,** *47* , 2921-2933.

3. Traeger, J. C. Photoionization Mass Spectrometry of the Propyl Halides, *Int. J. Mass Spectrom. Ion. Phys.* **1980,** *32* , 309-319.

4. Rosenstock, H. M.; Buff, R.; Ferreira, M. A. A.; Lias, S. G.; Parr, A. C.; Stockbauer, R.; Holmes, J. L. Fragmentation mechanism and energetics of some alkyl halide ions, *J. Am. Chem. Soc.* **1982,** *104* , 2337-2345.

5. Baer, T.; Song, Y.; Ng, C. Y.; Liu, J.; Chen, W. The heat of formation of 2-$C_3H_7^+$ and the proton affinity of C_3H_6 determined by pulsed field ionization - photoelectron photoion coincidence spectroscopy, *J. Phys. Chem. A* **2000,** *104* , 1959-1964.

6. Brooks, A.; Lau, K.-C.; Ng, C. Y.; Baer, T. The C(3)H(7)(+) appearance energy from 2-iodopropane and 2-chloropropane studied by threshold photoelectron photoion coincidence, *Eur. J. Mass Spectrom.* **2004,** *10* , 819-828.

7. Traeger, J. C.; McLoughlin, R. G. Absolute heats of formation for gas phase cations, *J. Am. Chem. Soc.* **1981,** *103* , 3647-3652.

8. Bodi, A.; Shuman, N. S.; Baer, T. On the ionization and dissociative photoionization of iodomethane: a definitive experimental enthalpy of formation of CH_3I, *Phys. Chem. Chem. Phys.* **2009,** *11* , 11013-11021.

9. Houle, F. A.; Beauchamp, J. L. Photoelectron spectroscopy of methyl, ethyl, isopropyl and tert-butyl radicals. Implications for the thermochemistry and structure of the radicals and their corresponding carbonium ions, *J. Am. Chem. Soc.* **1979,** *101* , 4067-4074.

10. Dyke, J. M.; Ellis, A.; Jonathan, N.; Morris, A. Vacuum Ultraviolet Photoelectron Spectroscopy of Transient Species, *J. Chem. Soc. Faraday Trans. 2* **1985,** *81* , 1573-1586.

11. Chase, M. W. *NIST-JANAF Thermochemical Tables;* 4th ed.; American Institute of Physics: New York, 1998.

12. Lau, K.-C.; Ng, C. Y. Accurate ab initio predictions of ionization energies and heats of formation for the 2-propyl, phenyl, and benzyl radicals, *J. Chem. Phys.* **2006,** *124* , 044323-1-044323/9.

13. Guyon, P. M.; Baer, T.; Nenner, I. Interactions between neutral dissociation and ionization continua in N_2O, *J. Chem. Phys.* **1983,** *78* , 3665-3672.

14. Chupka, W. A.; Miller, P. J.; Eyler, E. E. Predissociation induced ro-vibrational autoionization and zero energy photoelectrons, *J. Chem. Phys.* **1988,** *88* , 3032-3036.

15. Kercher, J. P.; Stevens, W.; Gengeliczki, Z.; Baer, T. Modeling Ionic Unimolecular Dissociations from a Temperature Controlled TPEPCIO Study on 1-C_4H_9I ions, *Int. J. Mass Spectrom.* **2007,** *267* , 159-166.

16. Keister, J. W.; Riley, J. S.; Baer, T. The t-butyl ion heat of formation and the isobutene proton affinity, *J. Am. Chem. Soc.* **1993,** *115* , 12613-12614.

17. Park, S. T.; Kim, S. K.; Kim, M. S. One-photon mass-analyzed threshold spectroscopy of 1- and 2-iodopropanes in vacuum ultraviolet, *J. Chem. Phys.* **2001,** *114* , 5568-5576.

18. Ayala, P. Y.; Schlegel, H. B. Identification and treatment of internal rotation in normal mode vibrational analysis, *J. Chem. Phys.* **1998,** *108* , 2314-2325.

19. Pittam, D. A.; Pilcher G. Measurements of heats of combustion by flame calorimetry. Part 8.-Methane, ethane, propane, n-butane and 2-methylpropane, *J. Chem. Soc. Faraday Trans. 1* **1972,** *68* , 2224-2229.

20. Pedley, J. B. *Thermochemical Data and Structures of Organic Compounds;* Thermodynamics Research Center: College Station, 1994.

21. Chase, M. W., Jr. *NIST-JANAF Thermochemical Tables;* Fourth ed.; 1998; Vol. Monograph 9.

22. Seakins, P. W.; Pilling, M. J.; Niiranen, J. T.; Gutman, D.; Krasnoperov, L. N. Kinetics and thermochemistry of R+HBr<=>RH+Br reactions: Determination of the heat of formation of C_2H_5, i-C_3H_7, sec-C_4H_9, and t-C_4H_9, *J. Phys. Chem.* **1992,** *96* , 9847-9855.

23. Ruscic, B.; Pinzon, R. E.; Morton, M. L.; Laszevski, G.; Bittner, S. J.; Nijsure, S. G.; Amin, K. A.; Minkoff, M.; Wagner, A. F. Introduction to Active Thermochemical Tables: Several "Key" Enthalpies of Formation Revisited, *J. Phys. Chem. A* **2004,** *108* , 9979-9997.

24. Weitzel, K. M.; Malow, M.; Jarvis, G. K.; Baer, T.; Song, Y.; Ng, C. Y. High-resolution pulsed field ionization photoelectron photoion coincidence study of CH_4: Accurate 0 K dissociation threshold for CH_3^+, *J. Chem. Phys.* **1999,** *111* , 8267-8270.

25. Karton, A.; Rabinovich, E.; Martin, J. M. L.; Ruscic, B. W4 theory for computational thermochemistry: In pursuit of confident sub-kJ/mol predictions, *J. Chem. Phys.* **2006,** *125* , 144108-1-144108/17.

26. Tajti, A.; Szalay, P. G.; Csaszar, A. G.; Kallay, M.; Gauss, J.; Valeev, E. F.; Flowers, B. A.; Vazquez, J.; Stanton, J. F. HEAT: high accuracy extrapolated ab initio thermochemistry, *J. Chem. Phys.* **2004,** *121* , 11599-11613.

27. Bodi, A.; Kercher, J. P.; Bond, C.; Meteesatien, P.; Sztáray, B.; Baer, T. Photoion Photoelectron Coincidence Spectroscopy of Primary Amines RCH_2NH_2 (R = H, CH_3, C_2H_5, C_3H_7, i-C_3H_7): Alkylamine and Alkyl Radical Heats of Formation by Isodesmic Reaction Networks, *J. Phys. Chem. A* **2006,** *110* , 13425-13433.

28. Meot-Ner, M. The proton affinity scale, and effects of ion structure and solvation, *Int. J. Mass Spectrom.* **2003,** *227* , 525-554.

29. Szulejko, J. E.; McMahon, T. B. Progress toward an absolute gas phase proton affinity scale, *J. Am. Chem. Soc.* **1993,** *115* , 7839-7848.

30. Meot-Ner, M.; Sieck, L. W. Relative acidities of water and methanol and the stabilities of the dimer anions, *J. Phys. Chem.* **1986,** *90* , 6687-6690.

31. Smith, B. J.; Radom, L. Assigning absolute values to proton affinities: A differentiation between competing scales, *J. Am. Chem. Soc.* **1993,** *115* , 4885-4888.

CHAPTER 4: Specific Rate Constants k*(E)* of the Dissociation of the Halobenzene Ions: Analysis by Statistical Unimolecular Rate Theories

4.1   Introduction

Unimolecular dissociation reactions provide an important access to the threshold energies E_0 for bond breaking. The specific rate constants *k(E)* of these reactions (apart from some fine structure) decrease with decreasing energy E and approach their minimum value as $E \rightarrow E_0$. In order to derive E_0 from *k(E)*, this quantity must be measured experimentally at energies close enough to E_0 that a unique extrapolation is feasible. In addition to the limited range of specific experimental methods, in dissociations with rate constants at threshold slower than about 10^2 s^{-1} it is not possible to directly measure these low energy rates due to competition from radiative decay.[1,2] In these cases, the difference between the experimental appearance energy of the fragments and the bond energy E_0, the so-called "kinetic shift",[3,4] needs to be determined by fitting the measured part of *k(E)* to a model from unimolecular rate theory.[5] Larger molecules have minimum rate constants well below 10^2 s^{-1} and thus require rate constants to be accurate over several orders of magnitude to correctly extrapolate to E_0. For energy selected reactants, a commonly used model for the specific unimolecular rate constants (*k(E)*) is the Rice-Ramsperger-Kassel-Marcus (RRKM) equation:[5]

$$k(E) = \frac{\sigma N^{\ddagger}(E - E_0)}{h\rho(E)}$$

<div align="right">(4.1)</div>

where $N^{\ddagger}(E-E_0)$ is the sum of states of the transition state, $\rho(E)$ is the ion density

ostates, σ is the reaction degeneracy, and h is Planck's constant. In evaluating $N^{\ddagger}(E-E_0)$,

it is useful to separate conserved vibrational modes from the transitional modes, which

are converted from vibrations into rotational and translational degrees of freedom as the

reaction coordinate R goes to infinity. Differences arise in the various rate theories from

their treatment of these transitional modes in calculating $N^{\ddagger}(E-E_0)$.

Phase space theory (PST) as advanced by Light, Pechukas, Klots, Chesnavich and

Bowers[6-10] treats $N^{\ddagger}(E-E_0)$ by locating the transition state at either ∞ along the reaction

coordinate R, or at the centrifugal barrier. In our treatment we assume the low J limit, for

which both models place the transition state at R $= \infty$, at which point the transitional

modes have become rotations. Thus, $k(E)$ is determined by the phase space available to

the products. This treatment is appropriate for reactions where the interaction potential

between the products is isotropic at large separations. At the other extreme is rigid

activated complex RRKM theory (RAC-RRKM), in which the transitional modes are

treated as vibrations with fixed frequencies. This is appropriate for reactions with real

barriers, in which the transition state structure is located at this barrier and does not

change with internal energy. However, it is well known that for reactions with no barrier,

the effective transition state, which is related to an entropic minimum, shifts from $R = \infty$

when $E = E_0$ to progressively smaller values as the energy is raised.[5] Several statistical

unimolecular rate models have been developed to account for this feature.

In variational transition state theory (VTST), the entropic minimum mentioned above is found by locating the global minimum in the sum of states $N(E-V(R))$ along the reaction coordinate.[11-13] Depending on the implementation of the model, two minima may be found, corresponding to a tight transition state (TTS) at smaller values of R and an orbiting transition state (OTS) at large R.[14] Both minima shift inward as the energy increases, but at some energy an abrupt switch from OTS to TTS may occur. There has been some debate as to whether this transition state switching is physically meaningful in a single-well ionic dissociation, or if only the more gentle transition state shifting occurs, and the two entropic wells are merely an artifact of the approximations used in the interpolation.[15]

An alternative approach to this problem is the statistical adiabatic channel model (SACM) in which the rovibrational quantum states of the reactant are treated as invariant throughout the dissociation by following adiabatic potential curves linking the reactant states and the equivalent product states. Each potential curve has a barrier, the maximum of which moves inward along the reaction coordinate as the energy and angular momentum of the channel increase.[5] A full implementation of either VTST or SACM requires considerable computational effort. Rate constants derived from a full SACM-classical trajectory (SACM-CT) treatment however, have been shown to be reproduced by the much simpler PST with suitable rigidity factors incorporated.[16] Such simplified versions of SACM (SSACM) require no more effort than PST as will be demonstrated below.

It has become clear that in barrierless neutral-neutral dissociations the inward movement of the transition state is significant and RAC-RRKM and PST are insufficient

to model the reaction rate.[17] Instead, the extra effort of VTST or SACM is required. The need is less clear, however, in barrierless ionic dissociations. The stronger long range attraction due to ion-induced dipole interactions causes the transition state to be located at larger values of R. The question then arises whether PST is still insufficient to accurately model the rates.

Troe *et al*[16] recently showed that RAC-RRKM fails to predict accurate E_0's in the case of the dissociations of the benzene and butylbenzene cations. However these systems are not ideal for an analysis of kinetic shifts. The former involves a Renner-Teller type avoided curve-crossing between a ground $^2B_1$ and an electronically excited $^2A_1$ state of $C_6H_6^+$.[16,18,19] For the latter system, experimental data[20,21] only exist at higher rates ($k(E) > 10^5$ s^{-1}) which require a large extrapolation to E_0. Additionally, the structure of $C_7H_7^+$ is not known with certainty and the energetics are thus not firmly established. For this reason, we have chosen to investigate other systems which are more suitable for an analysis of kinetic shifts and for the study of energy dependences of specific rate constants $k(E)$. Such systems should fulfill a number of conditions: (i) $k(E)$ should be measurable over a large range; (ii) the thermochemistry of the system should be established sufficiently well by other than kinetic means; (iii) the potential along the dissociating bond should correspond to a simple bond fission, and not show complications such as avoided crossings, small barriers, or reefs.

The halobenzene ion dissociations (2) appear to be suitable systems for the described analysis.

$$C_6H_5X^+ \rightarrow C_6H_5^+ + X^\bullet \quad (X = Cl, Br, \text{ and } I) \quad (4.2)$$

The dissociation does not involve a curve crossing although both singlet and triplet states of $C_6H_5^+$ may be produced. Experimental values of $k(E)$ can be measured over sufficiently large ranges, in the present work over 3–5 orders of magnitude, and the thermochemistry of the reactions is relatively well known. Additionally, the polarizability of the halogens, and therefore the strength of the long-range attraction in the dissociation, increases from Cl to Br to I.

   Previous measurements of halobenzene ion dissociation rates have been obtained by numerous workers[22-35] with varying methods, precisions, and ranges of $k(E)$. In this paper we use threshold photoelectron-photoion coincidence (TPEPICO) to accurately measure the dissociation rate constants over a large range for these three ions and then compare the modeling of these rates with the statistical theories mentioned above in order to determine which methods are appropriate to extrapolate the measured rate constants to their dissociation thresholds.

4.2   Experimental Results

Examples of TOF distributions corrected for hot electrons are shown in Figure 4-1. The isotopic pattern of the parent ion peaks for chlorobenzene is clearly evident at 12.806 eV, where the two chlorine isotopes (35 and 37) as well as the ^{13}C peaks are fully resolved. At higher energies, the subtraction of the hot electron TOF spectrum eliminates these parent ions (in some cases imperfectly because of the sharp peaks). The broad peak to the right of the parent ion is due to fragment ions that were born in the long drift region.

To extend the experimental range of the bromobenzene data, spectra were taken using a temperature-controlled inlet[36] set to 256 K and an extraction field of 50 V cm^{-1}.

The lowered temperature and steeper gradient improved mass resolution and decreased the time spent in the first acceleration region where we obtain our kinetic information allowing for rates as fast as $10^7 \, \text{s}^{-1}$ to be observed for bromobenzene. Threshold photoelectron spectra of argon were taken to ensure that the electron energy resolution was not significantly reduced by the increased extraction fields.

4.3 Thermochemistry of the Dissociations of Halobenzene Ions

Before presenting and analyzing our kinetic data, we briefly inspect the available thermochemical data for the reactions described in equation 4.2. Assuming that there are no energy barriers for the reverse reactions, the E_0's of the halobenzene dissociations are derived from known heats of formation of the participating species through

$$E_0 = \Delta H^0_{f,0K}(\text{X}^\bullet) + \Delta H^0_{f,0K}(\text{C}_6\text{H}_5^+) - \Delta H^0_{f,0K}(\text{C}_6\text{H}_5\text{X}^+) \tag{4.3}$$

The heats of formation of the neutral halobenzene molecules $\text{C}_6\text{H}_5\text{X}$ are given in Table 4- 1. They are accurate to $\pm$ 1.3 kJ •mol^{-1} ($\pm$13 meV) for chlorobenzene and somewhat less certain for bromo- and iodobenzene. The ionization energies for all three halobenzenes have recently been determined by ZEKE spectroscopy[37] and are accurate within 0.05 kJ mol^{-1}. The values for the halogen atoms are well established.[38] The heat of formation of the phenyl cation was obtained from the Active Thermochemical Tables (ATcT)[39,40] by private communication[41] as 1149.1 $\pm$ 1.8 kJ•mol^{-1}. This value is in good agreement with a derived value of 1148.5 $\pm$ 3.4 kJ•mol^{-1} determined from the heat of formation of the phenyl radical[42] and a phenyl ionization energy calculated by Lau and

65
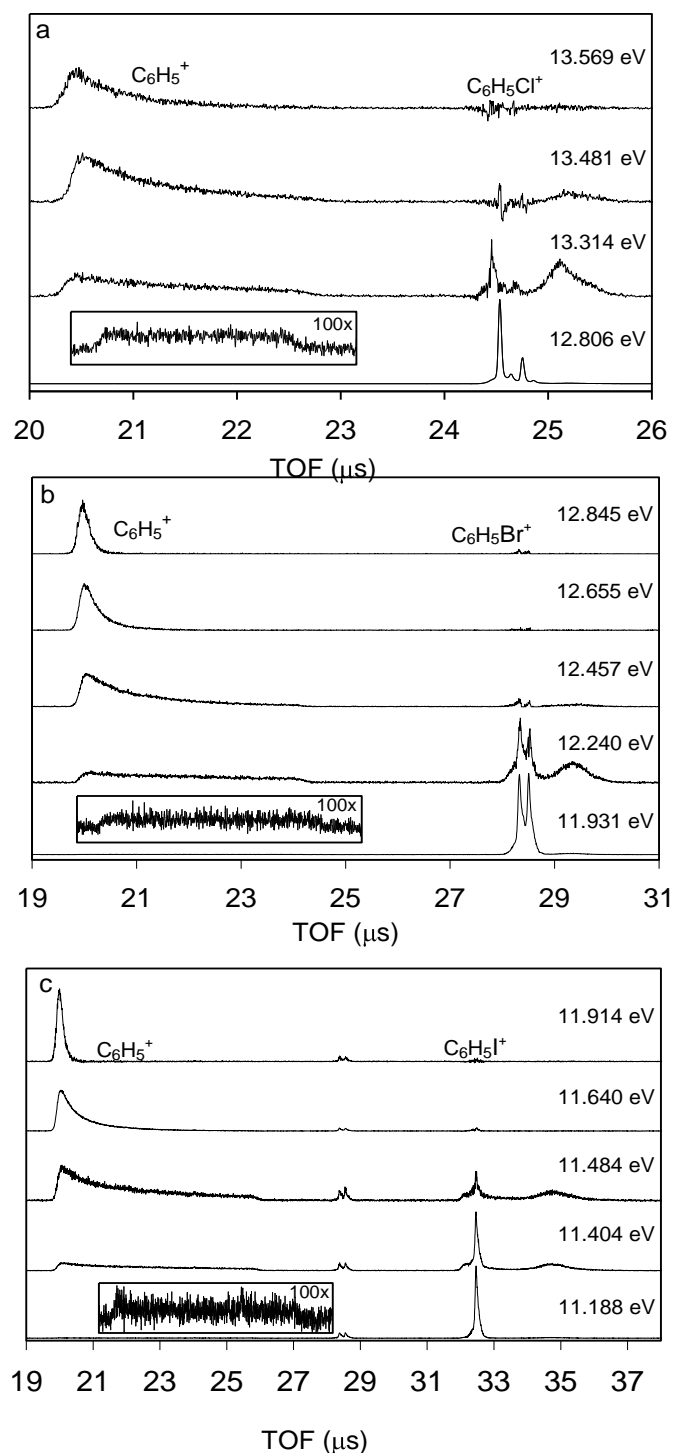
Figure 4-1a-c: Time of flight distributions for the three halobenzene ions at selected photon energies. All spectra have been corrected for energetic electron contamination which accounts for the noise in the region of the parent peak at higher energies. The peak at 28.5 μs in 2c is due to remnant bromobenzene in the sample line, however the bromobenzene ion does not dissociate at these photon energies and does not affect the fragment peak area.
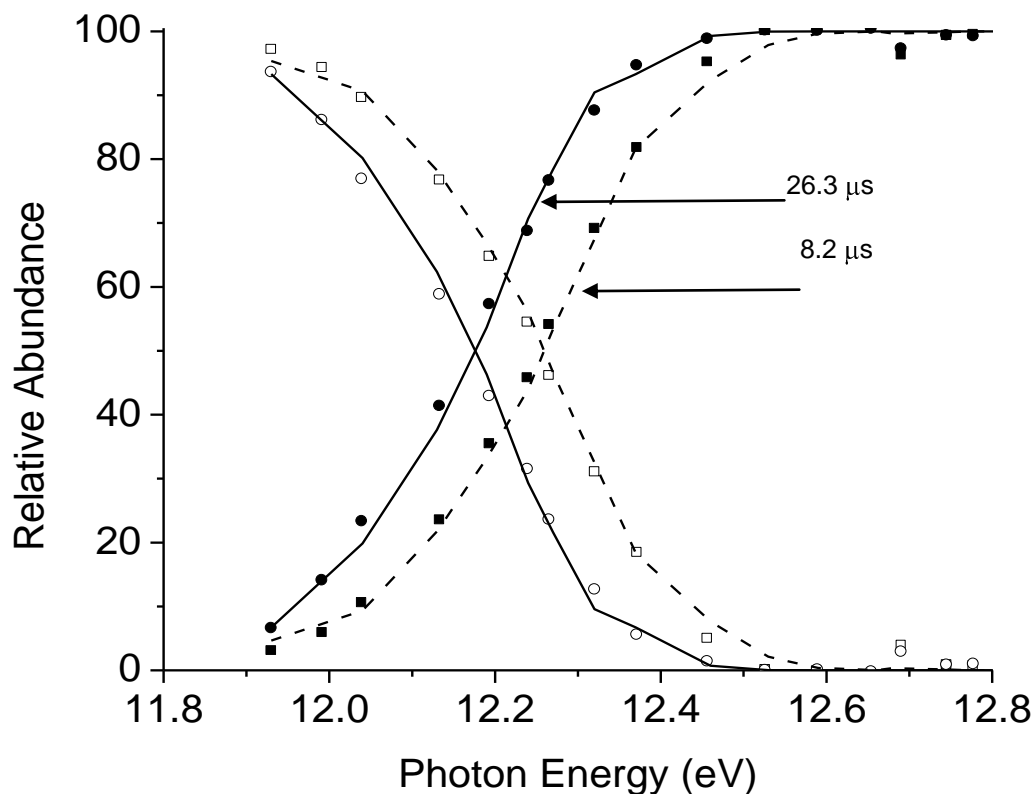
Figure 4- 2 Breakdown curves for bromobenzene. Experimental points indicate abundance of ions dissociating to $C_6H_5^+$ within 8.2 μs (squares) or within 26.3 μs (circles). The respective open points indicate the relative abundance of ions that did not dissociate within that time window. Lines are obtained by fitting the experimental fragment peak shape and relative ion abundances at each photon energy using RAC-RRKM theory at 8.2 μs (---) and 26.3 μs (—)at each photon energy.

Ng^{43}. On the basis of these data, the values $E_0 = 3.381 \pm 0.038$, 2.812 ± 0.046, and 2.382 ± 0.064 eV are obtained for the dissociations of chloro-, bromo- and iodo- benzene ions, respectively.

Table 4- 1. Literature thermochemical values used to determine reference E_0s. (kJ mol^{-1})

Molecule	$\Delta_f H^o_{298K}$	$\Delta_f H^o_{0K}$	IE (eV)
C_6H_5Cl	52.0 ± 1.3[44]	66.42 ± 1.3	$9.0728(6)$[37]
C_6H_5Br	105.4 ± 4.9[44]	127.0 ± 4.1	$8.9976(6)$[37]
C_6H_5I	164.9 ± 5.9[44]	180.7 ± 5.9	$8.7580(6)$[37]
$Cl\bullet$	$121.302(6)$[38]	$119.621(6)$[38] $117.92(6)$[38]	
$Br\bullet$	$111.86(6)$[38]		
$I\bullet$	$106.76(4)$[38]	$107.16(4)$[38]	
$C_6H_5^+$		1149.1 ± 1.8[41]	

4.4 Experimental Determination of Specific Rate Constants k(E)

The specific rate constants *k(E)* of the dissociation determine both the abundance of dissociated ions and the shape of the asymmetric fragment peak in the TOF spectrum. However, while our photon resolution is as narrow as 12 meV, our "energy-selected" ions are produced from a room temperature sample of neutrals and therefore correspond to a room temperature thermal energy distribution. Consequently, our experimentally observed dissociation rates are averages over the internal energy distributions of the ions such as illustrated in Figure 4- 3. In order to extract the rate constants as a function of ion internal energy, we convoluted an assumed *k(E)* function with the thermal energy distribution.

At the lowest experimental energies little information is available from the shape of the fragment peak in the TOF distribution because this distribution is very flat (see Figure 4-1). At these energies, the rate is mainly determined from the relative peak areas of the parent ions, the asymmetric peak, and the drift peak after the parent ion. However, at higher energies the asymmetric shape of the first peak provides the bulk of the rate information. The largest range of rate constants was accessible for the bromobenzene ion because there are large Franck-Condon factors in the photoelectron spectrum over the full range, which permitted us to obtain rate constants over almost 5 orders of magnitude. In the case of the chlorobenzene ion, the experimental range was limited at high energies by a Franck-Condon gap and the low photon intensity of our light source. At low energies, the range was less than for bromobenzene because of the shorter chlorobenzene ion time of flight.

The convolution of the $k(E)$ function with the spectral width of our light source (*ca* 12 meV) and the energy distribution of our room temperature sample (*ca* 140 meV) was carried out for the TOF distribution and the relative abundances of parent and fragment ions. Denoting a calculated TOF distribution at an energy E by $F(E,t)$ and the thermal internal energy distribution by $f_{th}(E_{th})$, the convoluted TOF distribution $F_{eff}(h\nu,t)$ is given by

$$F_{eff}(h\nu,t) = \int_{0}^{\infty} f_{th}(E_{th}) F(h\nu + E_{th},t) dE_{th}$$

(4.4)

The TOF distribution $F(h\nu+E_{th},t)$, where t is the ion TOF, is directly given by the specific rate constants $k(E)$ at an energy $E = h\nu+E_{th}$, while $F_{eff}(h\nu,t)$ is the observable

TOF distribution. The fractional abundances A of the parent and fragment ions observed

up to a time τ, are given by

$$A_{parent} = \int_0^\infty f_{th}(E_{th})\exp[-k(h\nu + E_{th})\tau]dE_{th}$$

(4.5)

and

$$A_{fragment} = 1 - A_{parent} = \int_0^\infty f_{th}(E_{th})(1-\exp[-k(h\nu + E_{th})\tau])dE_{th}$$

(4.6)

$k(E)$ has to be chosen in such a way that the convoluted TOF distributions $F_{eff}(h\nu,t)$ and

the fractional ion abundances from the experiment are reproduced in an internally

consistent manner. We achieve this by using an RRKM trial function for $k(E)$

which is locally optimized around the energy of the data point. The procedure provides a

unique and correct $k(E)$ at an energy that corresponds to the peak of the thermal energy

distribution (Figure 4- 3) and is independent of the trial function. As an example of the

analysis of our experimental data, Figure 4- 4 shows a comparison of measured and fitted

TOF distributions in the bromobenzene system for a series of excitation energies.

The reported rate constants are those evaluated at the peak of each ion internal energy

distribution. They are shown, along with their uncertainties, in Table 4-2, Table 4- 3, and

Table 4-4 and in Figure 4- 5 and Figure 4- 6. The given errors were established by

observation of the fit to the experimental TOF distributions and breakdown diagrams.

The larger errors in the chlorobenzene rates from 3.893 to 4.163 eV and in the
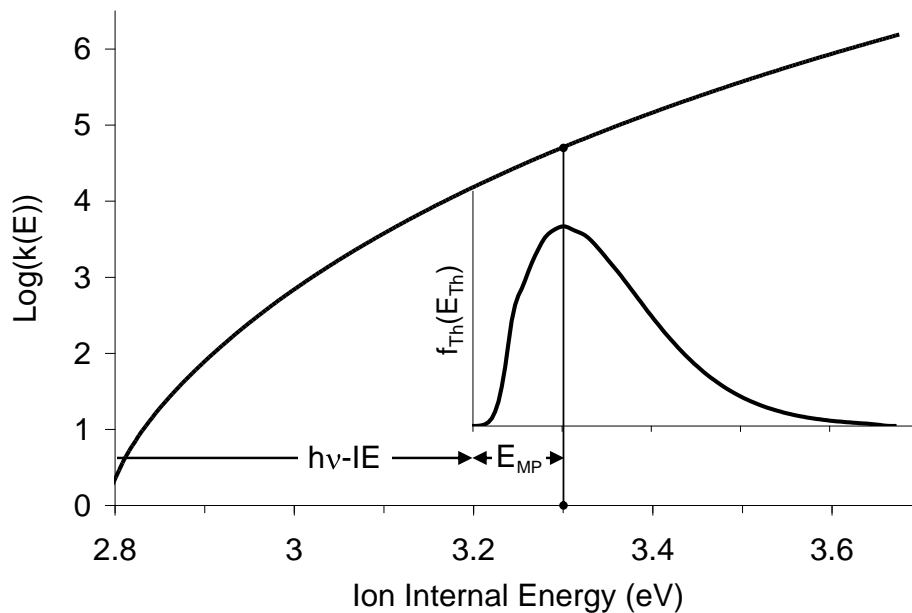
Figure 4- 3 Depiction of the ion thermal energy distribution ($f(E_{Th})$) and corresponding variation in the dissociation rate at a single photon energy. Experimental $k(E)$ for a single ion internal energy are determined from the RRKM $k(E)$ evaluated at the most probable (MP) energy in the ion internal energy distribution ($h\nu - IE + E_{MP}$) as described in the text where E_{MP}=56 meV, 61 meV, and 61 meV for chloro-, bromo-, and iodobenzene.

bromobenzene rates from 3.136 to 3.323 eV reflect a discrepancy between the rate constants derived from the fragment peak shapes and those derived from the relative areas of the fragment and parent peaks. Before comparing the measured rate constants to the calculated dissociation rate constants, it is important to establish whether at low energies the ions could be stabilized by IR emission. Such an emission would effectively stabilize the parent ions and yield a daughter to parent ratio that is too low. The IR emission rates, calculated using the method described by Dunbar[45] with frequencies and IR emission intensities calculated using Gaussian 03,[46] were similar for all three systems and ranged from about 100 photons·s^{-1} at 2.4 eV internal energy to 450 photons·s^{-1} at 5 eV. Although IR emission is competitive with dissociation at the lowest experimental energies, the effect on the extracted rate constants is much smaller than the reported error bars.

The measured rate constants range from 3×10^2 s^{-1} to 10^7 s^{-1}, a range of over 4 orders of magnitude. A number of groups have previously determined halobenzene ion dissociation *k(E)* rates using a variety of techniques and covering selected regions of the k*(E)* curve (Figure 4- 5).[22-33,35,47] Baer *et al*[22] reported rate constants for all three molecular ions that were obtained by fitting the TPEPICO TOF distributions for the room temperature sample with a single exponential decay. These points have rates that are too high. In a subsequent paper[35] the rates for the bromobenzene ion were analyzed in terms of a distribution of single exponential decays over the thermal energy distribution, resulting in rate constants that are in agreement with the current measurements. In a series of three papers, Rosenstock *et al.*[23-25] measured k*(E)* for the three ions by fitting an RRKM curve to breakdown diagrams obtained by TPEPICO at two ion extraction times.
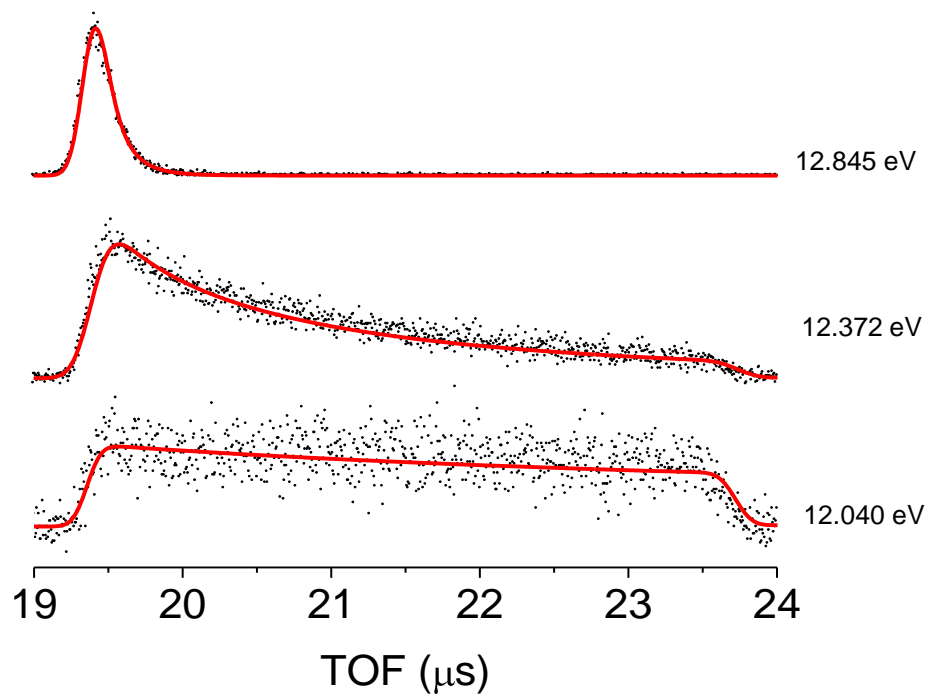
Figure 4- 4 Experimental and modeled fragment peaks for bromobenzene at various photon energies.

Table 4-2. Experimental and Calculated Log($k(E)$) / s^{-1} for chlorobenzene.

hν	E(eV)	exp.[a]	RRKM	PST	SSACM	VTST
12.753	3.736	$2.79^{0.10}_{0.09}$	2.80	2.34	2.77	2.75
12.806	3.789	$3.07^{0.10}_{0.09}$	3.07	2.71	3.06	3.09
12.872	3.855	$3.33^{0.09}_{0.05}$	3.38	3.13	3.39	3.43
12.932	3.915	$3.68^{0.32}_{0.11}$	3.55	3.35	3.56	3.59
12.987	3.970	$4.00^{0.30}_{0.20}$	3.87	3.76	3.89	3.91
13.062	4.045	$4.09^{0.46}_{0.01}$	4.17	4.12	4.19	4.20
13.117	4.100	$4.34^{0.40}_{0.07}$	4.37	4.37	4.39	4.39
13.180	4.163	$4.52^{0.29}_{0.08}$	4.58	4.64	4.60	4.60
13.222	4.205	$4.74^{0.18}_{0.13}$	4.72	4.80	4.74	4.74
13.264	4.247	$4.85^{0.10}_{0.07}$	4.86	4.96	4.87	4.87
13.314	4.297	$5.05^{0.07}_{0.08}$	5.01	5.15	5.03	5.02
13.314	4.297	$5.02^{0.15}_{0.06}$				
13.357	4.340	$5.18^{0.04}_{0.09}$	5.14	5.30	5.15	5.14
13.415	4.398	$5.33^{0.09}_{0.05}$	5.30	5.49	5.31	5.30
13.481	4.464	$5.46^{0.10}_{0.04}$	5.48	5.70	5.48	5.47
13.495	4.478	$5.57^{0.19}_{0.11}$	5.52	5.75	5.52	5.51
13.522	4.505	$5.59^{0.24}_{0.08}$	5.59	5.83	5.59	5.58
13.569	4.552	$5.64^{0.15}_{0.06}$	5.71	5.97	5.70	5.69
13.569	4.552	$5.76^{0.35}_{0.08}$				
13.719	4.702	$5.97^{0.14}_{0.07}$	6.07	6.38	6.04	6.03

[a]The superscripts and subscripts represent the upper and lower uncertainties in the experimental values respectively.

Table 4- 3 As in Table 4-2 except for bromobenzene.

hv	E(eV)	exp.[a]	RRKM	PST	SSACM	VTST
11.931	2.994	$2.64^{0.27}_{0.39}$	2.94	2.11	2.68	2.57
12.04	3.103	$3.51^{0.13}_{0.13}$	3.60	3.10	3.47	3.45
12.134	3.197	$4.03^{0.11}_{0.12}$	4.09	3.77	4.02	4.06
12.194	3.257	$4.35^{0.11}_{0.09}$	4.37	4.14	4.32	4.40
12.240	3.303	$4.58^{0.14}_{0.13}$	4.57	4.40	4.54	4.62
12.266	3.329	$4.74^{0.09}_{0.09}$	4.68	4.54	4.66	4.73
12.321	3.384	$4.97^{0.13}_{0.13}$	4.90	4.82	4.89	4.95
12.372	3.435	$5.20^{0.12}_{0.12}$	5.09	5.05	5.10	5.14
12.457	3.520	$5.49^{0.09}_{0.09}$	5.39	5.42	5.41	5.43
12.527	3.590	$5.69^{0.09}_{0.09}$	5.62	5.70	5.65	5.65
12.590	3.653	$5.92^{0.08}_{0.06}$	5.82	5.93	5.85	5.84
12.655	3.718	$6.13^{0.07}_{0.07}$	6.00	6.15	6.04	6.03
12.681[b]	3.722	$6.02^{0.10}_{0.05}$	6.01	6.54	6.37	6.35
12.778	3.841	$6.43^{0.10}_{0.07}$	6.34	6.71	6.52	6.49
12.845	3.908	$6.56^{0.16}_{0.13}$	6.49	6.16	6.05	6.04
12.919[b]	3.960	$6.62^{0.10}_{0.10}$	6.63	6.88	6.66	6.63
12.976[b]	4.017	$6.72^{0.09}_{0.07}$	6.76	7.03	6.79	6.76
13.022[b]	4.063	$6.81^{0.07}_{0.08}$	6.86	7.14	6.89	6.86
13.069[b]	4.110	$6.89^{0.09}_{0.05}$	6.97	7.27	7.00	6.96
13.145[b]	4.186	$6.93^{0.07}_{0.06}$	7.12	7.44	7.15	7.11

[a]The superscripts and subscripts represent the upper and lower uncertainties in the experimental values respectively. [b]Measurements taken at 40 V/cm and 256 K.

Table 4-4. As in Table 4-2 except for Iodobenzene

$h\nu$	E(eV)	exp.[a]	RRKM	PST	SSACM	VTST
11.188	2.491	$2.64_{0.25}^{0.34}$	2.73	2.45	2.75	2.63
11.234	2.537	$3.16_{0.22}^{0.09}$	3.21	3.03	3.22	3.13
11.275	2.578	$3.61_{0.16}^{0.19}$	3.59	3.48	3.59	3.54
11.326	2.629	$4.00_{0.07}^{0.17}$	4.00	3.94	4.01	3.98
11.378	2.681	$4.42_{0.14}^{0.04}$	4.37	4.34	4.39	4.37
11.404	2.707	$4.53_{0.07}^{0.07}$	4.53	4.53	4.56	4.55
11.431	2.734	$4.72_{0.10}^{0.07}$	4.70	4.71	4.73	4.73
11.457	2.760	$4.86_{0.13}^{0.07}$	4.86	4.87	4.88	4.89
11.484	2.787	$5.03_{0.13}^{0.07}$	5.01	5.04	5.03	5.05
11.537	2.840	$5.27_{0.10}^{0.06}$	5.29	5.34	5.31	5.34
11.586	2.889	$5.56_{0.10}^{0.03}$	5.53	5.59	5.55	5.57
11.640	2.943	$5.74_{0.03}^{0.09}$	5.77	5.85	5.79	5.78
11.706	3.009	$6.04_{0.09}^{0.09}$	6.05	6.14	6.06	6.02
11.756	3.059	$6.19_{0.08}^{0.11}$	6.25	6.35	6.25	6.19
11.914	3.217	$6.73_{0.12}^{0.27}$	6.80	6.92	6.79	6.67

[a]The superscripts and subscripts represent the upper and lower uncertainties in the experimental values respectively.
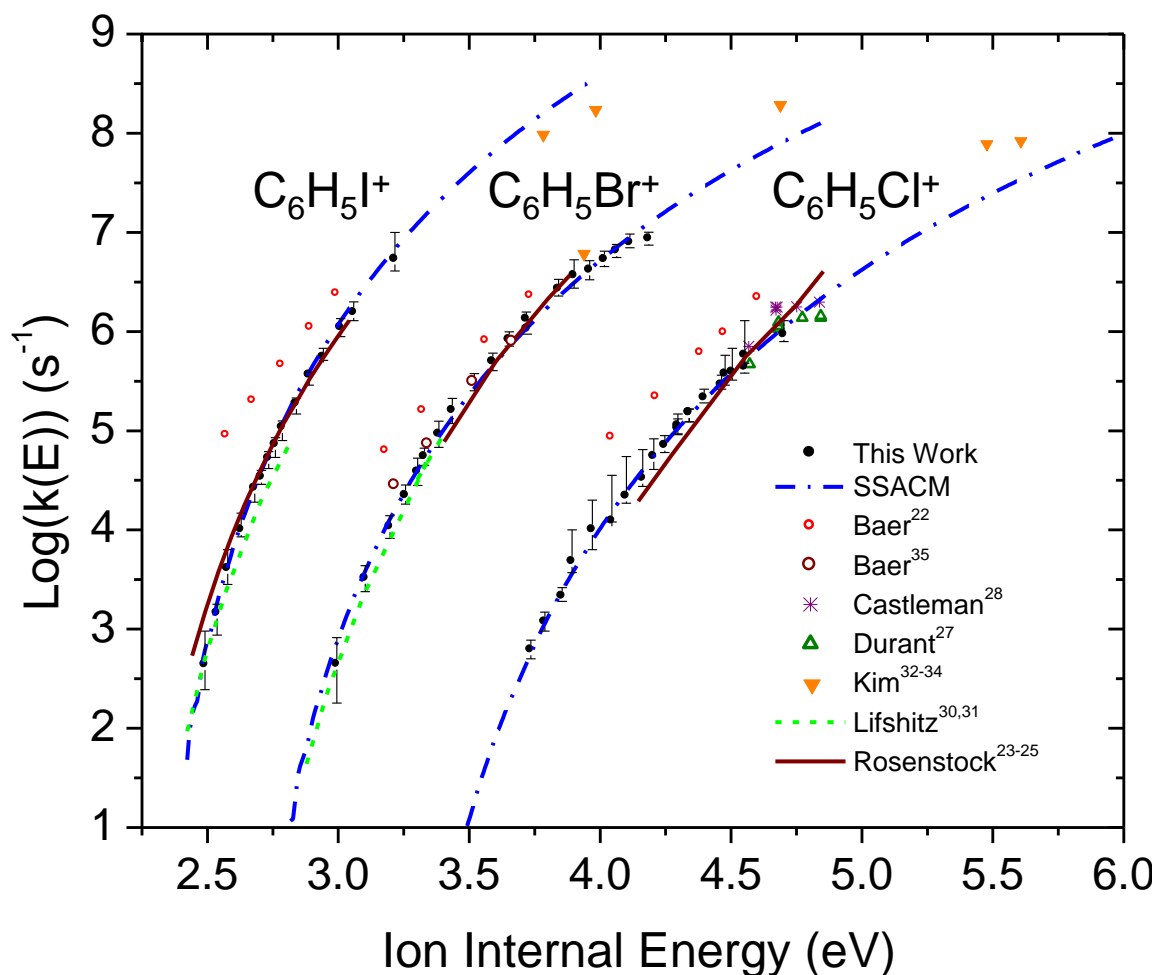
Figure 4- 5 Comparison of current experimental data with previously reported data. SSACM curves are calculated using the parameters that best describe the data presented in this paper. The names in the legend are those of the corresponding authors who reported the data and superscripts refer to their citations. For a detailed discussion of previous data see text. All *k(E)* data have been adjusted to reflect the most current ionization energies reported in table 1.

These rate constants, which extend between 2 to 3 orders of magnitude, agree well with the current data. In 1984, Durant et $al.$[27] used a supersonically cooled sample of chlorobenzene to investigate the ion dissociation rates in the vicinity of $k(E)\sim 10^6$ s^{-1} by multi-photon ionization time of flight mass spectrometry. A few years later, Castleman et $al.$[28] used a similar technique to study the chlorobenzene ion dissociation over a similarly limited range of rate constants by varying the reflector voltage in a reflectron-time of flight apparatus. None of these investigations reported rate measurements below about 5×10^4 s^{-1}, which means that they were not very useful for extrapolating the rate measurements to the dissociation threshold. However, Lifshitz et $al.$[30,31] performed a series of measurements using an ion trap, which could store the ions for up to milliseconds and could thus explore the critical low rate constant region for the case of bromo- and iodobenzene. Although the ions were not energy selected, the ion internal energy distribution obtained by single photon ionization was modeled and the ratios of the fragment and parent ions as a function of both photon energy and ion extraction time where reproduced using RRKM rate curves. This provided rates in the 10^2 to 10^5 s^{-1} range, which as shown in Figure 4- 5, agree quite nicely with our reported rate constants. Finally, Kim et $al.$[32,33,48] measured the $k(E)$s of iodo-, chloro-, and bromobenzene by mass-analyzed ion kinetic energy spectrometry (MIKES) in which ions prepared by charge transfer were photodissociated as they were traveling at high velocity toward an electric sector of a double focusing mass spectrometer. With the exception of one measurement for bromobenzene at a rate of 10^7 s^{-1}, which agrees with our rate constants, this yielded rates in the region of about $k(E)\sim 10^8$ s^{-1}, which for bromo- and chlorobenzene are clearly higher than the extrapolated rate constants using the SSACM

model. Because we did not measure rate constants up to 10^8 s^{-1}, we cannot be certain that the Kim rate constants are in error. However, it is worth mentioning that ion energy selection by charge transfer depends upon the assumption that the ionizing ion (Xe^+ for chlorobenzene and CS_2^+ for bromo- and iodobenzene) be in the ground state and that the charge transfer process is strictly resonant so that no energy is lost to translation.

4.5   Modeling the Rate Constants k(E) by Statistical Unimolecular Rate Theories

The lowest energy rate points measured are between 0.1 and 0.4 eV above E_0. In order to extrapolate the rate curves down to threshold we model the dissociations using several forms of statistical unimolecular rate theory: RAC-RRKM, PST, SSACM, and VTST (Figure 4- 6). These approaches all use the same density of states in the denominator of Eq. (4.1), but differ in the manner in which the sum of states is calculated. We have made the assumption that the various excited electronic states initially populated in the ionization process rapidly interconvert to the ground ionic state, thereby converting their electronic energy into vibrational energy of the ground state. However, ions are free to interconvert electronic and vibrational energy among the several electronic states that lie below the dissociation limit. We tested the contribution of the excited electronic state to the total density of states and found that even for the case of chlorobenzene, in which the upper spin orbit state lies only 100 meV above the ground state, the contribution is less than 10%. Such small differences are negligible and are generally compensated by assumed transition state frequencies.

4.5.1 Rigid Activated Complex RRKM Theory (RAC-RRKM):

In RAC-RRKM[5] theory, $N^{\ddagger}$ is a function of just the vibrational frequencies of the transition state, which we express by means of the calculated equilibrium frequencies of the halobenzene ion. The frequency corresponding to the C-X stretch is assumed to correspond to the reaction coordinate and is omitted from the transition state. The 27 vibrational modes of the phenyl ring are assumed to be conserved along the reaction coordinate, and the frequencies of the remaining 2 modes, corresponding to C-X bends, are scaled by a common factor. Two parameters, this frequency scaling factor and E_0, are optimized to find a best-fit to the experimental data.

The molecular parameters and the parameters used in the fitting are summarized in the Appendix. One should note that there are ambiguities even in this simple RAC-RRKM approach because, apart from the uncertainties in the frequency set, the contribution of anharmonicity can only be guessed. An energy-independent anharmonicity factor $F_{anh} = 1.4$ was adopted by Klippenstein et al[18] for the case of H loss from benzene ions. However, this ignores the fact that F_{anh} is energy dependent[5]. Here we take $F_{anh} = 1.0$ and include the effects of anharmonicity in the fitted transition state frequency scaling parameter. The experimental $k(E)$ curves can be fit well by this RAC-RRKM modeling, however, the resulting bond energies underestimate the chloro- and bromobenzene thermochemical values from section 3 by 0.13 eV, well outside the thermochemical uncertainties. Of the fitted values, only the iodobenzene value is within the uncertainty of the literature value. Tables 2-4 compare the RAC-RRKM $k(E)$ results with the experimental data.

The good agreement between the RAC-RRKM derived E_0 and the thermochemical value for the iodobenzene ion dissociation is the result of the low E_0 which causes the minimum rate $k(E_0)$ to be larger and therefore the kinetic shift to be smaller. For bromobenzene, in addition to inaccurately predicting the E_0, the described RAC-RRKM modeling was unable to provide good agreement simultaneously at the upper and lower extremes of the data set. The results for chlorobenzene demonstrate most clearly the shortcomings of the RAC-RRKM method. The experimental chlorobenzene data set extends over the smallest experimental range (three orders of magnitude), and requires the largest extrapolation to E_0. These two factors allow for a 'worst case scenario' where the modeling in Figure 4- 6 reproduces the chlorobenzene data deceivingly well over the entire data set but nevertheless predicts a dissociation energy that is too low by 0.13 eV.

4.5.2   Phase Space Theory (PST)

The underestimation of E_0 by RAC-RRKM theory agrees with the observations made by Troe et al.,[16] namely that RAC-RRKM fails because it treats the activated complex with a set of vibrational oscillators, resulting in a $k(E)$ function with too weak an energy dependence. One then might think that PST is more appropriate for ionic dissociations, because it considers the activated complex at $R = \infty$, where the transitional modes are rotations and the energy dependence of $k(E)$ is much stronger. In this case, the activated complex frequencies are those of the phenyl product ion. The density of states of these "conserved oscillators" is then convoluted with the relevant number of states $N_{orb}(E)$ of the orbital motion of the fragments. We simplify any rotational effects by using only $k(E,J=0)$ for which $N_{orb}(E) \approx (E - E_0)/B_{eff}$ and $B_{eff} = (ABC)^{1/3}$,[49] thereby treating the phenyl ion as a spherical top. The J-dependence of $k(E,J)$ in this case is known to be

small and can practically be neglected if E is identified with the vibrational energy.[16]

However, it must be accounted for through $E_0(J)$ when thermal rate constants for

dissociation or the reverse combination are calculated. We again neglect anharmonicity

($F_{anh} = 1.0$) and note that there are considerable uncertainties in the frequencies of the

phenyl cation (see Appendix). The two frequency sets determined by Klippenstein[19] lead

to differences in $k(E)$ by about a factor of 2. Regardless of this ambiguity, using the

frequencies determined here, the PST $k(E)$ (Figure 4- 6) provides a good fit to the

iodobenzene ion experimental $k(E)$, but not to the chloro- or bromobenzene ion data. The

only parameter, E_0, is varied in order to fit the PST rates at an energy near the middle of

the experimental data set. This leads to values of E_0 that are larger than the

thermochemical values. Apart from the uncertainties in the frequency set and the

anharmonicity factor, the PST model of $k(E,J=0)$ is a single-parameter fitting approach

which provides upper limits of E_0. We note that the PST rate curve anchored at the

literature value of E_0 provides a good fit to the experimental rates below 10^5 s^{-1} for the

bromobenzene ion and below 10^4 s^{-1} for the chlorobenzene ion, but significantly

overestimates the higher energy rates.

The overestimation of k (E) by PST, if the true E_0 is chosen, is a general

phenomenon which, within the framework of the SACM, is attributed to the anisotropy of

the potential energy surface and is characterized by a "rigidity factor" f_{rigid} being smaller

than unity. One might try to represent this effect by an increased value of B_{eff} in $N_{orb}(E)$,

which corresponds to an energy-independent value of f_{rigid} such as was proposed in the

simplest version of a "simplified SACM" (SSACM)[50]. Adopting this approach here and

fitting the scaling factor of B_{eff} in the middle of the experiments still overestimates the

true E_0. Although this approach accounts for some rigidity of the activated complexes, it

does not do this in an adequate manner when large energy ranges are considered. A more realistic procedure requires energy-dependent rigidity factors such as discussed in the following section. Alternatively variational transition state theory (VTST) may be used such as also described in the following. In these models, there will be a gentle "shifting" or a more abrupt "switching" of the effective transition states from larger fragment distances at lower energies to smaller distances at higher energies. As a result, $k(E)$ with increasing energy falls increasingly below the PST values.

4.5.3 Simplified SACM(SSACM) for Ion Dissociation

Rigidity factors $f_{rigid}(E)$ reflect the anisotropy of the potential and, in addition, the subtle interplay between the anisotropic and attractive properties of the potential, i.e. they are specific for particular types of potential energy surfaces of the dissociation process.[51] In some cases, like ion fragmentations dominated by long range ion-permanent dipole forces,[52] f_{rigid} is energy independent, but strongly depends on angular momentum J. In other cases like ion fragmentations governed by a superposition of polarizability and permanent dipole contributions, E- and J-dependences of $f_{rigid}(E,J)$ arise.[53] Energy-dependent rigidity factors $f_{rigid}(E)$ are also typical for ion fragmentations which at short range are dominated by valence forces and at long range by comparably weak ion-induced dipole forces. A detailed SACM/CT treatment was applied[16] to systems of this type. The results could approximately be described by a functional form of $k(E)$ in which $N_{orb}(E)$ is used from PST and is multiplied by an energy-dependent rigidity factor given approximately by

$$f_{rigid}(E) = \exp[-(E-E_0)/c] \qquad (4.7)$$

This version of a SSACM was shown to mimic the transition state shifting or switching and found to reproduce quite well the results of the full SACM/CT calculations

on modelled potential energy surfaces for the fragmentations of benzene and n-butylbenzene cations.

Similar to RAC-RRKM theory, this version of SSACM contains two adjustable parameters, E_0 and c. In order to determine the best-fit E_0 and the corresponding uncertainty, we calculate a least-linear squares error between the calculated and experimentally determined rate curves for all reasonable combinations of E_0 and c. The results are recorded in Figure 4- 5 and Figure 4- 6 and Table 4-2, Table 4- 3, Table 4-4, and Table 4- 5. Our best fits correspond to values of $E_0 = 3.355^{0.030}_{0.040}$, $2.783^{0.026}_{0.029}$, and $2.415^{0.020}_{0.027}$ eV, where the superscripts and subscripts respectively correspond to the upper and lower uncertainties, and c = 71, 77, and 194 meV for chloro-, bromo-, and iodobenzene, respectively. The meaning of the c parameter will be discussed later.

We obtain the error limits for the onset energies by calculating a least squares error between the calculated and experimentally determined rate curves for all reasonable combinations of E_0 and the fit parameter c (Figure 4- 7). The reported E_0 corresponds to the best fit value, while the uncertainties correspond to the limits of a goodness-of-fit contour (Figure 4- 7, bold contour) beyond which the agreement of the rate curves is determined to be poor. The relationship between E_0, the fit parameter c and the resulting error bars are plotted in Figure 4- 8 for the three halobenzenes. Figure 4- 7 and Figure 4-8 show the origins of the sometimes asymmetric error bars. The nearly vertical line in the case of iodobenzene indicates that, within the experimental window, $k(E)$ is independent of c and is therefore described well by PST.

4.5.4 Microcanonical Variational Transition State Theory (VTST)

Microcanonical VTST locates the transition state at the minimum in the $N(E,R)$ along the reaction coordinate R, which moves to shorter bond distances with increasing E. Obtaining $N(E,R)$ requires knowledge of both the interaction potential and transitional modes along R. elow is a simplified approach to obtaining $N(E,R)$ proposed by Chesnavich et al[14]. For this version of VTST, the potential is approximated by

$$V_{CX}(R) \approx \frac{D_e}{c_1 - 6}\left\{2(3 - c_2)\exp[c_1(1-X)] - (4c_2 - c_1 c_2 + c_1)X^{-6} - (c_1 - 6)c_2 X^{-4}\right\}$$

(4.8)

where X is the reduced length, $X = R/R_e$, of the dissociating bond, D_e is the dissociation energy corrected for the zero point energy, $c_2 = \alpha q^2 / 2R_e^4 D_e$ with the polarizability α of the halogen atoms, q is the ionic charge, and c_1 is determined by the force constant of the C-X stretch. These quantities are calculated and given in the Appendix. We note that the corresponding quantum-chemical potentials for chloro- and bromobenzene[19] are more repulsive than this empirical potential in the important region between 3 and 5 Å. We will return to this point below and highlight the relative unimportance of an accurate reaction coordinate potential in the VTST scheme.

The contribution of the transitional modes, which for the halobenzene dissociation are the two C-X bending modes, to $N_{tot}(E,R)$ was determined using a hindered rotor potential of the form

$$V(\theta) = \frac{V_0(r)}{2}(1 - \cos 2\theta)$$

(4.9)

The rotational barrier V_0 is a function of the bond length R of the form

$$V_0(r) = V_e \exp[-a(R - R_e)^3]$$

(4.10)

where a is a fit parameter that determines how quickly the rotational barrier decays as a function of bond length, and therefore the rate of "loosening" of the transitional modes. The equilibrium barrier heights V_e were calculated from the geometrical means of the equilibrium C-X bending frequencies and were derived to be 7.85, 5.92, and 4.85 eV for chloro-, bromo-, and iodobenzene, respectively. The exponent in (10) differs from the Gaussian form proposed by Chesnavich and used in previous studies.[14,29] In modelling the $k(E)$ data with VTST, we found that raising the $(R-R_e)$ function to the third power provided a better fit over the full range of the data, and more importantly, provided a much tighter fit (with uncertainties of ±3 kJ mol^{-1} as opposed to ±7 kJ mol^{-1}). Energy levels for the transitional modes, E_i, were calculated using a harmonic oscillator $E_i < V_0(R)$ and a Pitzer rotor model for $E_i > 0.75$ $V_0(R)$. $N_{tot}(E,R)$ was determined by convoluting the phenyl cation density of states with the contribution from the transitional modes. In all three reactions we found two minima of $N(E,R)$ along the reaction coordinate R, an outer TS at very large bond distances ($r > 15$Å), where $N(E,R)$ is independent of the parameter a, and a tight TS in the range $3 < r < 5$ Å where $N(E,r)$ strongly depends on a. At small E, the outer minimum is the global minimum, as E increases, the inner minimum increases at a slower rate and eventually determines the rate.

We obtained an optimum fit to the experimental $k(E)$ with the parameters $E_0 = 3.401^{0.017}_{0.062}$, $2.829^{0.012}_{0.030}$, and $2.420^{0.010}_{0.011}$ eV and $a = 0.38, 0.28$, and 0.22 Å^{-2} for chloro-, bromo-, and iodobenzene, respectively. The VTST results are plotted with experimental $k(E)$ for comparison in Figure 4- 6 and listed in and Table 4-2, Table 4- 3, Table 4-4, and

Table 4- 5. The uncertainties in E_0 were determined in the same way as for the present

SSACM, and are included in Figure 4- 8.

Table 4- 5 compares the E_0 values obtained by the different approaches. In the

cases of chloro- and bromobenzene, RAC-RRKM extrapolates to too low a barrier,

PSTextrapolates to too high a barrier, while both VTST and SSACM extrapolate to

barriers within mutual uncertainty of the literature values. All four methods correctly the

uncertainty of the literature value of the iodobenzene ion dissociation.

Table 4- 5 Dissociation energies E_0 (eV) for $C_6H_5X^+ \rightarrow C_6H_5^+ + X$ (see text)

	Reference E_0	RRKM	PST[†]	SSACM[*]	VTST[*]
$C_6H_5Cl^+$	3.381 ± 0.023	3.253 ± 0.05	3.457	$3.355^{0.030}_{0.040}$	$3.401^{0.017}_{0.062}$
$C_6H_5Br^+$	2.812 ± 0.046	2.684 ± 0.06	2.874	$2.783^{0.026}_{0.029}$	$2.829^{0.012}_{0.030}$
$C_6H_5I^+$	2.382 ± 0.070	2.387 ± 0.05	2.435 ± 0.01	$2.415^{0.020}_{0.027}$	$2.420^{0.010}_{0.011}$

*The superscripts and subscripts represent the upper and lower uncertainties in the
experimental   values respectively. †Due to poor fits to the experimental data, uncertainties
are not reported for chlorobenzene and bromobenzene.

4.6   Discussion

Neither the RAC-RRKM nor PST approaches correctly extrapolate to the reaction

barriers for the chloro- and bromobenzene ion dissociations explored here or the benzene

and *n*-butylbenzene ions previously studied.[16] Of particular concern is the fact that the

RAC-RRKM theory is perfectly capable of fitting data over a broad range of rates from

10^3 to 10^7 s^{-1} and provides no clues about its inability to extrapolate to the onset.   Thus,

if the predicted kinetic shift is greater than about 0.2 eV, it is best not to apply RAC-

RRKM for extrapolation. In contrast, both the VTST approach correctly determines the

E_0 for not only the iodobenzene but also the chloro- and bromobenzene ion dissociations
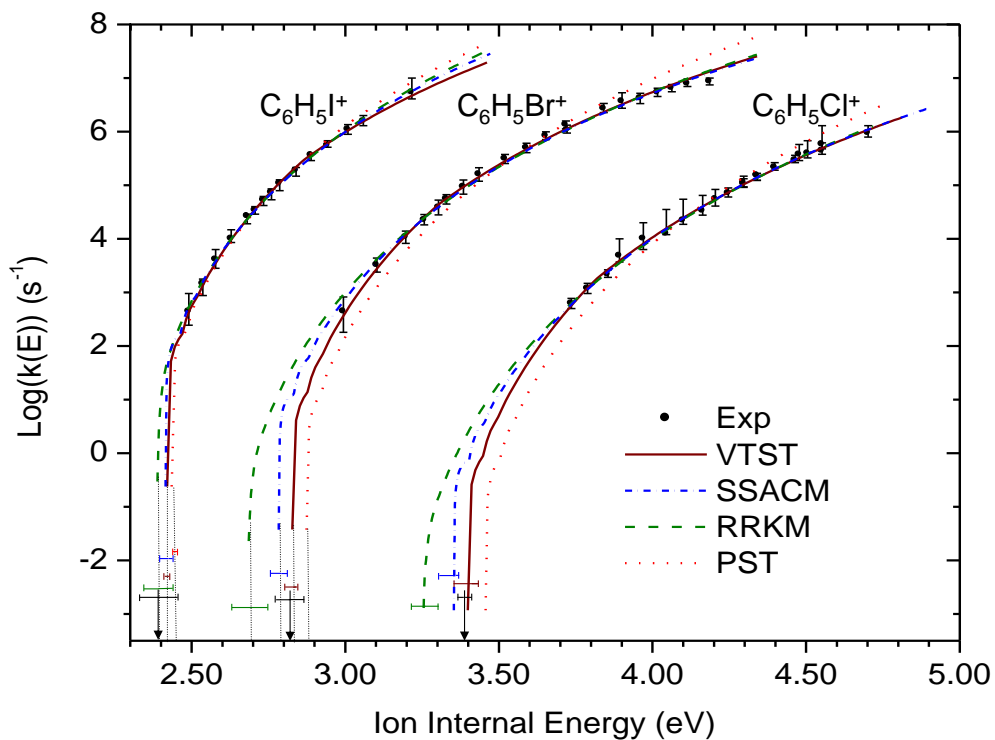
Figure 4- 6. Comparison of rate curves predicted by several models (see text) of statistical unimolecular dissociation fit to experimentally determined rate points. Literature dissociation thresholds (E_0) are indicated by black arrows. Dotted vertical lies for iodo and bromobenzene are to guide the eye from lowest $k(E_0)$ point to the horizontal axis. The determination of errors bars in rate points and E_0 is described in the text.
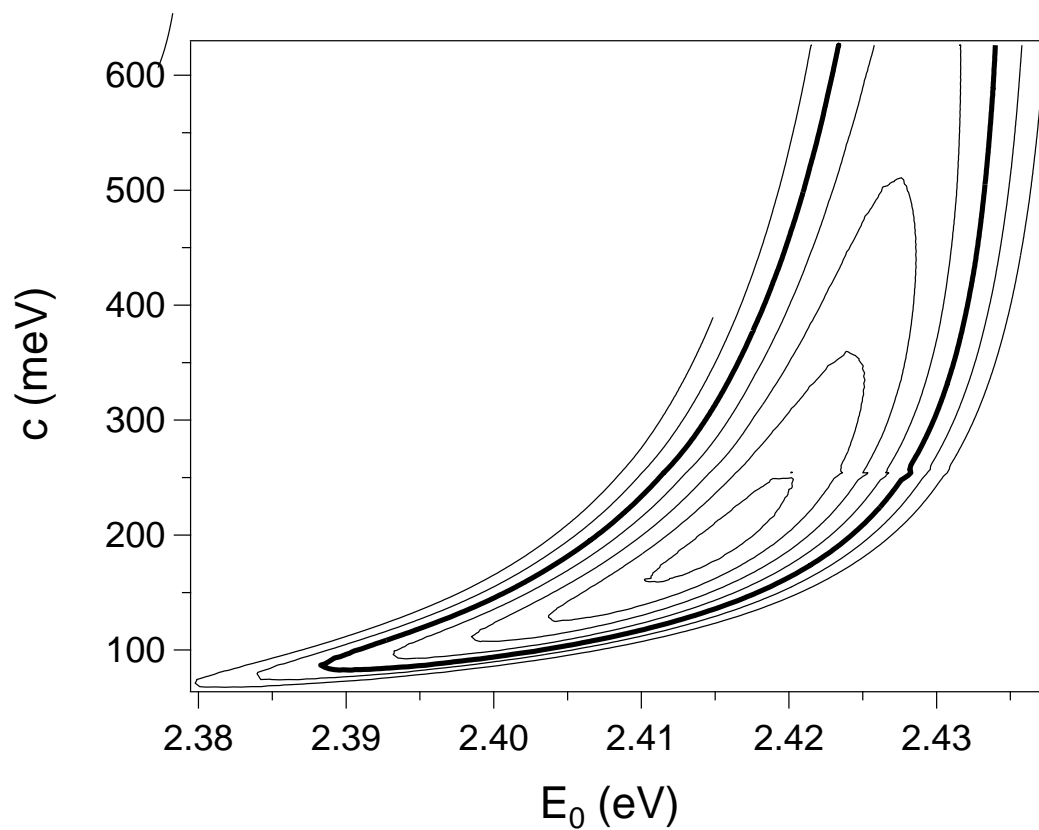
Figure 4- 7 The two-parameter c versus E_0 plot used to determine the best fit SSACM $k(E)$ curve for the experimental rate constants for iodobenzene. The bold contour represents the maximum error that defines an acceptable fit.
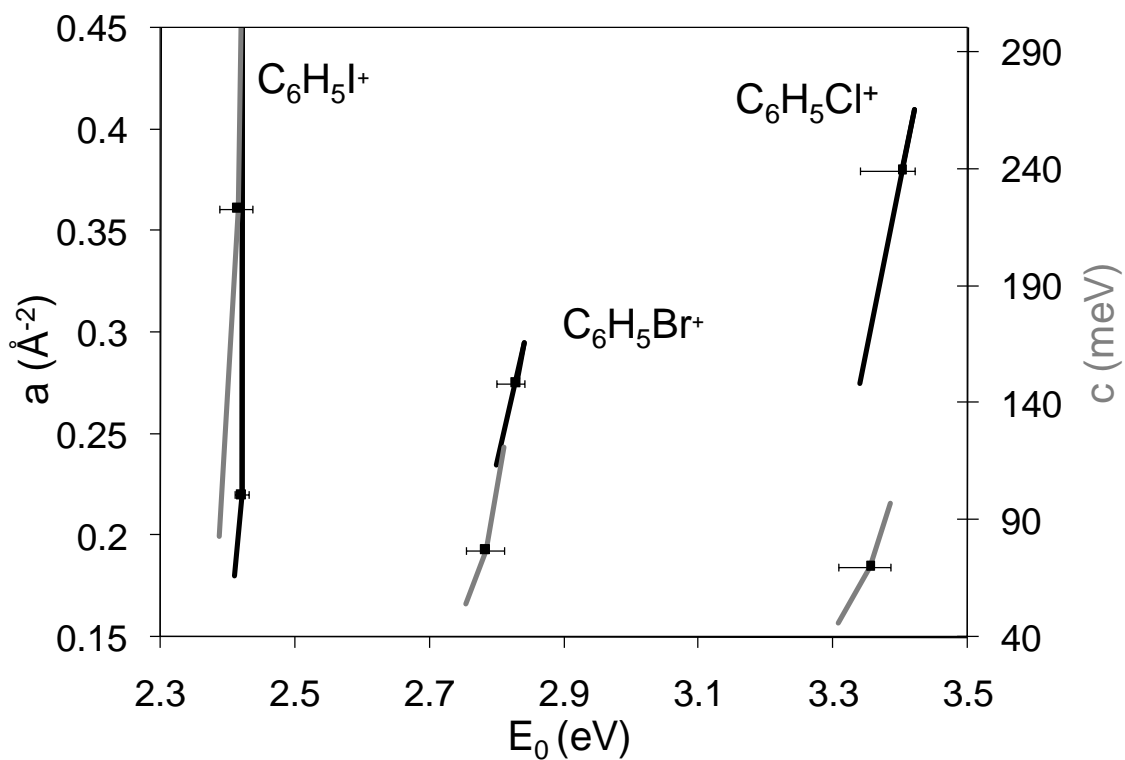
Figure 4- 8. Combinations of E_0 and fitting parameter (see text) determined by VTST (black, left axis) and SSACM (gray, right axis) that yield an acceptable fit to the experimentally determined rate curves. Points are the best fit parameters and the limits of the whiskers are the derived uncertainties in E_0.

while SSACM determines the E_0 to within the uncertainty of bromobenzene and is just outside the limit of uncertainty for the chlorobenzene E_0.

The VTST and SSACM models produce nearly identical rate curves over the experimental range, along with similar E_0s and uncertainties. The VTST calculation requires knowledge of the potential energy surface along the entire reaction coordinate, whereas the SSACM requires only the product vibrational and rotational frequencies. Additionally, the SSACM rate curve can be calculated using 2 orders of magnitude less computational effort than our VTST curve. In fact, it requires no more effort than the RAC-RRKM method.

What physical insight does the functional form of eq. 4.7 and the values of the parameter c provide? The energy-dependence of $f_{rigid}(E)$ signals a potential with changing anisotropy character, being strongly anisotropic at short range where valence forces dominate and being nearly isotropic at long range where ion-induced dipole forces are relevant. The values of the parameters c, being 71, 77, and 194 meV for chloro, bromo, and iodobenzene, respectively, are of the same order as observed in benzene and n-butylbenzene cation dissociations.[16] In an intricate manner they reflect the transition from the anisotropic to the isotropic region of the potential. The larger value of c for iodobenzene indicates that the relative contribution of the isotropic long range part of the potential in comparison to the anisotropic short range part is larger than for chloro- and bromobenzene, due to the smaller value of E_0. However, a more quantitative connection to details of the potential would require the full SACM/CT treatment on the complete potential energy surface. This is beyond the scope of our present work.

It might appear that our version of VTST provides more dynamical information than SSACM because we identify the entropy bottle neck directly by minimizing the sum

of states. However, we found that our empirical potential, fitted to some of the molecular properties of the ion, does not correspond well with a DFT calculated interaction potential. Furthermore, when we replace the empirical potential with a DFT calculated curve, or even a simple Morse potential, the *a* parameter changes, but the overall fit of the rates to the data and its ability to extrapolate to the onset is not affected. This means that our approach is simply a procedure that reproduces the data using an adjustable parameter. The empirical VTST approach also does not lend much insight into the question of transition state switching versus a smooth transition from PST at low energy to RRKM at high energy. For instance, we observe an abrupt transition-state switch at 10^4 s^{-1} for chlorobenzene and at 10^5 s^{-1} for the bromobenzene ion dissociations. However, the energy at which the switch occurs is highly dependent on the specifics of the model. The data can be well fit and the switch occur inside the experimental range, outside that range, or not at all depending on the treatment of the transitional modes (i.e. the value of the *a* parameter and the form of eq. 4.10). Further insight about the issue of transition state switching can be found in discussions by Klippenstein[19] and Hase[15]. On the basis of our results, we conclude that the *a* parameter is effectively a catch-all fitting parameter, much like the c parameter in the SSACM or the frequency scaling factor in RAC-RRKM. On the one hand this robustness lends confidence in the results of the calculation in that incorrect assumptions about the potential energy surface do not bias the results, but on the other hand, it means that *a* does not have a precise meaning.

Because both VTST and the SSACM provide similar results and similarly limited physical insight into the dissociations, the considerably simpler SSACM is the preferred approach. Although VTST and SSACM both predict E_0s that are within the experimental error, the error limits are smaller than those of the experiment, and the two theories

systematically differ in that the VTST approach yields slightly lower E_0s than does the SSACM, and their predictions in the case of chloro- and bromobenzene are just beyond the error of each method. Both methods predict a considerably higher E_0 for iodobenzene, which means that the experimental values for the heat of formation of iodobenzene should probably be lowered by 3 kJ mol^{-1}. If the precision of the thermochemistry of the halobenzene ion dissociations could be improved, it could decide whether VTST or SSACM approaches are more accurate. Finally, it is worth noting that the version of SSACM used is essentially a first order correction to the PST and is thus most accurate at low energies. As the energy is increased, the employed rigidity factor decreases faster than the PST $k(E)$ increases and the calculated reaction rates become too slow, even decreasing at higher energies, which is clearly not in accord with experiment. This can be corrected for by adding a small energy independent term to eq. 4.7. The VTST rate curves do not suffer from this same problem, however their accuracy at higher energies are untested.

Whether the VTST or SSACM method is used, the accuracy of the derived E_0 values is highly dependent on the quality and range of the experimentally determined rate curves. The uncertainties in E_0 scale roughly linearly with the uncertainties in the experimental rates and are very sensitive to the range of the experimental data. For chlorobenzene, excluding rates below 10^4 s^{-1} from our analysis doubles the uncertainty in the derived E_0 and excluding rates below 10^5 s^{-1} increases the uncertainty beyond reasonable limits. However, the effect of increasing the experimental range at higher energies is marginal. Excluding all rates above 10^4 s^{-1} only doubles the uncertainty. The VTST analysis of Lifshitz et al.[29] of the bromobenzene ion dissociation illustrates this point. The modeled rate curve, fit to experimental PIE data ranging from 10^3 s^{-1} to 10^5 s^{-}

[1], is wholly inaccurate at higher rates, but the extrapolated E_0 is nearly as accurate and precise as the results presented here.

4.7 Conclusions

Rate constants for energy selected dissociation of the halobenzene ions have been measured by TPEPICO over four orders of magnitude from 4×10^2 to 9×10^6 s^{-1}. Rate curves calculated by RAC-RRKM, PST, SSACM, and VTST were fitted to the experimental rate data and used to extrapolate the rates down to the threshold energy, E_0. The derived dissociation onsets were compared to the known E_0s as determined from literature thermochemical values. While RAC-RRKM provided good fits to the experimental rate curves, the predicted E_0s were significantly lower than the literature values for the chloro- and bromobenzene ion dissociations. PST provided neither good fits to the experimental rate curves for chloro- and bromobenzene, nor the correct E_0s. Although both models correctly predict the E_0 of the iodobenzene ion dissociation, PST and RAC-RRKM should not be used for barrierless ionic dissociations. Both simplified 2-parameter versions of VTST and SSACM properly fit the experimental rate curves and extrapolate to the correct E_0 for all three halobenzene ion dissociations with VTST appearing to do better for the case of chlorobenzene. However, SSACM is significantly simpler to employ.

Finally, the range and quality of the experimental rate points are critical to any method of extrapolating the rate curve down to threshold. The uncertainty in the derived E_0 scales approximately linearly with the uncertainty in the experimental data points, while extending the experimental range to the lowest rates possible is vital for an accurate determination.

Reference List

1. Asamoto, B.; Dunbar, R. C. Observation of the infrared radiative relaxation of iodobenzene ions using two light pulse photodissociation, *J. Phys. Chem.* **1987,** *91* , 2804-2807.

2. Dunbar, R. C.; Chen, J. H.; So, H. Y.; Asamoto, B. Infrared fluorescence relaxation of photoexcited gas-phase ions by chopped laser two-photon dissociation, *J. Chem. Phys.* **1987,** *86* , 2081-2086.

3. Chupka, W. A. Effect of unimolecular decay kinetics on the interpretation of appearance potentials, *J. Chem. Phys.* **1959,** *30* , 191-211.

4. Lifshitz, C. Time-resolved appearance energies, breakdown graphs, and mass spectra: the elusive "kinetic shift", *Mass Spectrom. Rev.* **1982,** *1* , 309-348.

5. Baer, T.; Hase, W. L. *Unimolecular Reaction Dynamics: Theory and Experiments;* Oxford University Press: New York, 1996.

6. Light, J. C. Phase space theory of chemical kinetics, *J. Chem. Phys.* **1964,** *40* , 3221-3229.

7. Pechukas, P.; Light, J. C. On detailed balancing and statistical theories of chemical kinetics, *J. Chem. Phys.* **1965,** *42* , 3281-3291.

8. Klots, C. E. Reformulation of the quasiequilibrium theory of ionic fragmentation, *J. Phys. Chem.* **1971,** *75* , 1526-1532.

9. Klots, C. E. Ionic Fragmentation through centrifugal barriers, *Chem. Phys. Lett.* **1971,** *10* , 422-xxx.

10. Chesnavich, W. J.; Bowers, M. T. Statistical phase space theory of polyatomic systems: Rigorous energy and angular momentum conservation in reactions involving symmetric polyatomic species., *J. Chem. Phys.* **1977,** *66* , 2306-2315.

11. Chesnavich, W. J. Multiple transition states in unimolecular reactions, *J. Chem. Phys.* **1986,** *84* , 2615-2619.

12. Hase, W. L. The criterion of minimum state density in unimolecular rate theory. An application to ethane dissociation, *J. Chem. Phys.* **1976,** *64* , 2442-2449.

13. Klippenstein, S. J.; Marcus, R. A. Application of unimolecular reaction theory for highly flexible transition states to the dissociation of CH_2CO into CH_2 and CO, *J. Chem. Phys.* **1989,** *91* , 2280-2292.

14. Chesnavich, W. J.; Bass, L.; Su, T.; Bowers, M. T. Multiple transition states in unimolecular reactions: A transition state switching model. Application to the $C_4H_8^+$ system, *J. Chem. Phys.* **1981,** *74* , 2228-2246.

15. Hu, X.; Hase, W. L. Properties of canonical variational transition state theory for association reactions without potential energy barriers, *J. Phys. Chem.* **1989,** *93* , 6029-6038.

16. Troe, J.; Ushakov, V. G.; Viggiano, A. A. On the Model Dependence of Kinetic Shifts in Unimolecular Reactions: The Dissociation of the Cations of Benzene and n-Butylbenzene, *J. Phys. Chem. A* **2006,** *110* , 1491-1499.

17. Klippenstein, S. J.; East, A. L. L.; Allen, W. D. A high level ab initio map and direct statistical treatment of the fragmentation of singlet ketene, *Journal of Chemical Physics* **1996,** *105* , 118-140.

18. Klippenstein, S. J.; Faulk, J. D.; Dunbar, R. C. A combined theoretical and experimental study of the dissociation of benzene cation, *J. Chem. Phys.* **1993,** *98* , 243-256.

19. Klippenstein, S. J. Ab initio reaction path energetics for the CX dissociations of C6H5X+ with X = H, F, Cl, and Br, *International Journal of Mass Spectrometry* **1997,** *167* , 235-257.

20. Baer, T.; Dutuit, O.; Mestdagh, H.; Rolando, C. Dissociation dynamics of n-butylbenzene ions: The competitive production of m/z 91 and 92 fragement ions, *J. Phys. Chem.* **1988,** *92* , 5674-5679.

21. Muntean, F.; Armentrout, P. B. Modeling Kinetic Shifts and Competition in Threshold Collision-Induced Dissociation. Case Study: n-Butylbenzene Cation Dissociation, *J. Phys. Chem. A* **2003,** *107* , 7413-7422.

22. Baer, T.; Tsai, B. P.; Smith, D.; Murray, P. T. Absolute unimolecular decay rates of energy selected metastable halobenzene ions, *J. Chem. Phys.* **1976,** *64* , 2460-2465.

23. Rosenstock, H. M.; Stockbauer, R.; Parr, A. C. Kinetic shift in chlorobenzene ion fragmentation and the heat of formation of the phenyl ion, *J. Chem. Phys.* **1979,** *71* , 3708-xxx.

24. Rosenstock, H. M.; Stockbauer, R.; Parr, A. C. Photoelectron-photoion coincidence study of the bromobenzene ion, *J. Chem. Phys.* **1980,** *73* , 773-777.

25. Dannacher, J.; Rosenstock, H. M.; Buff, R.; Parr, A. C.; Stockbauer, R.; Bombach, R.; Stadelmann, J. P. Benchmark measurement of iodobenzene ion fragmentation rates, *Chem. Phys.* **1983,** *75* , 23-35.

26. Pratt, S. T.; Chupka, W. A. Photoionization study of the kinetics of unimolecular decomposition of halobenzene ions, *Chem. Phys.* **1981,** *62* , 153-163.

27. Durant, J. L.; Rider, D. M.; Anderson, S. L.; Proch, F. D.; Zare, R. N. Unimolecular dissociation rates of chlorobenzene cation prepared by multiphoton ionization, *J. Chem. Phys.* **1984,** *80* , 1817-1825.

28. Stanley, R. J.; Cook, M.; Castleman, A. W. Unimolecular dissociation rate constant: Chlorobenzene cations revisited by using a new method, *J. Phys. Chem.* **1990,** *94* , 3668-3674.

29. Lifshitz, C.; Louage, F.; Aviyente, V.; Song, K. Transition State switching for single potential well ionic dissociations, *J. Phys. Chem.* **1991,** *95* , 9298-9302.

30. Gefen, S.; Lifshitz, C. Time-dependent mass spectra and breakdown graphs V. The kinetic shift in iodobenzene. A time resolved electron impact study., *Int. J. Mass Spectrom. Ion. Proc.* **1984,** *58* , 251-258.

31. Malinovich, Y.; Arakawa, R.; Haase, G.; Lifshitz, C. Time-dependent mass spectra and breakdown graphs. 6. Slow unimolecular dissociation of bromobenzene ions at near threshold energies, *J. Phys. Chem.* **1985,** *89* , 2253-2260.

32. Yim, Y. H.; Kim, M. S. Photodissociation of iodobenzene molecular ion: Investigation of entropy bottleneck in ionic systems, *J. Phys. Chem.* **1993,** *97* , 12122-12126.

33. Yim, Y. H.; Kim, M. S. Photodissociation of chlorobenzene molecular ion: Investigation of entropy bottleneck in ionic systems 2, *J. Phys. Chem.* **1994,** *98* , 5201-5206.

34. Lim, S. H.; Choe, J. C.; Kim, M. S. C6H5Br+center dot -> C6H5++Br-center dot occurs via orbiting transition state, *J. Phys. Chem. A* **1998,** *102* , 7375-7381.

35. Baer, T.; Kury, R. Random energy flow in the dissociation of energy selected bromobenzene and bromobenzene-d$_5$ ions, *Chem. Phys. Lett.* **1982,** *92* , 659-662.

36. Kercher, J. P.; Stevens, W.; Gengeliczki, Z.; Baer, T. Modeling Ionic Unimolecular Dissociations from a Temperature Controlled TPEPCIO Study on 1-C$_4$H$_9$I ions, *Int. J. Mass Spectrom.* **2007,** *267* , 159-166.

37. Kwon, C. H.; Kim, H. L.; Kim, M. S. Vibrational spectra of halobenzene cations in the ground and ~B 2B2 electronic states obtained by one-photon mass-analyzed threshold ionization spectrometry, *J. Chem. Phys.* **2002,** *116* , 10361-10371.

38. Chase, M. W. *NIST-JANAF Thermochemical Tables;* 4th ed.; American Institute of Physics: New York, 1998.

39. Ruscic, B.; Pinzon, R. E.; Morton, M. L.; Laszevski, G.; Bittner, S. J.; Nijsure, S. G.; Amin, K. A.; Minkoff, M.; Leahy, D.; Montoya, D.; Wagner, A. F. Active Thermochemical Tables: thermochemistry for the 21st century, *J. Phys. Conf. Ser.* **2005,** *16* , 561-570.

40. Ruscic, B.; Pinzon, R. E.; Morton, M. L.; Laszevski, G.; Bittner, S. J.; Nijsure, S. G.; Amin, K. A.; Minkoff, M.; Wagner, A. F. Introduction to Active Thermochemical Tables: Several "Key" Enthalpies of Formation Revisited, *J. Phys. Chem. A* **2004,** *108* , 9979-9997.

41. Ruscic, B. Private communication of interim ATcT results based on the Core (Argonne) Thermochemical Network ver. 1.078. Unpublished Work, 2009.

42. Blanksby, S. J.; Ellison, G. B. Bond Dissociation Energies of Organic Molecules, *Acc. Chem. Res.* **2003,** *36* , 255-263.

43. Lau, K.-C.; Ng, C. Y. Accurate ab initio predictions of ionization energies and heats of formation for the 2-propyl, phenyl, and benzyl radicals, *J. Chem. Phys.* **2006,** *124* , 044323-1-044323/9.

44. Pedley, J. B. *Thermochemical Data and Structures of Organic Compounds;* Thermodynamics Research Center: College Station, 1994.

45. Dunbar, R. C. Infrared Radiative Cooling of Gas-Phase Ions, *Mass Spectrom. Rev.* **1992,** *11* , 309-339.

46. *Gaussian 03, Revision C.02,* Frisch, M. J.; Trucks, G. W.; Schlegel, H. B.; Scuseria, G. E.; Robb, M. A.; Cheeseman, J. R.; Montgomery, J. A.; Vreven, T.; Kudin, K. N.; Burant, J. C.; Millam, J. M.; Iyengar, S. S.; Tomasi, J.; Barone, V.; Mennucci, B.; Cossi, M.; Scalmani, G.; Rega, N.; Petersson, G. A.; Nakatsuji, H.; Hada, M.; Ehara, M.; Toyota, K.; Fukuda, R.; Hasegawa, J.; Ishida, M.; Nakajima, T.; Honda, Y.; Kitao, O.; Nakai, H.; Klene, M.; Li, X.; Knox, J. E.; Hratchian, H. P.; Cross, J. B.; Adamo, C.; Jaramillo, J.; Gomperts, R.; Stratmann, F.; Yazyev, O.; Austin, A. J.; Cammi, R.; Pomelli, C.; Ochterski, J. W.; Ayala, P. Y.; Morokuma, K.; Voth, G. A.; Salvador, P.; Dannenberg, J. J.; Zakrzewski, V. G.; Dapprich, S.; Daniels, A. D.; Strain, M. C.; Farkas, Ö.; Malick, D. K.; Rabuck, A. D.; Raghavachari, K.; Foresman, J. B.; Ortiz, J. V.; Cui, Q.; Baboul, A. G.; Clifford, S.; Cioslowski, J.; Stefanov, B. B.; Liu, G.; Liashenko, A.; Piskorz, P.; Komáromi, I.; Martin, R. L.; Fox, D. J.; Keith, T.; Al-Laham, M. A.; Peng, C. Y.; Nanayakkara, A.; Challacombe, M.; Gill, P. M. W.; Johnson, B.; Chen, W.; Wong, M. W.; Gonzalez, C.; Pople, J. A. Gaussian, Inc.: Wallingford, CT, 2004.

47. Lim, S. H.; Choe, J. C.; Kim, M. S. C6H5Br+center dot -> C6H5++Br-center dot occurs via orbiting transition state, *J. Phys. Chem. A* **1998,** *102* , 7375-7381.

48. Lim, S. H.; Choe, J. C.; Kim, M. S. C6H5Br+center dot -> C6H5++Br-center dot occurs via orbiting transition state, *J. Phys. Chem. A* **1998,** *102* , 7375-7381.

49. Troe, J. Specific rate constants k(E,J) for unimolecular bond fissions, *J. Chem. Phys.* **1983,** *79* , 6017-6029.

50. Brouwer, L.; Cobos, C. J.; Troe, J.; Dubal, H. R.; Crim, F. F. Specific rate constants k(E,J) and product state distributions in simple bond fission reactions II. Application to HOOH --> OH + OH, *J. Chem. Phys.* **1987,** *86* , 6171-6182.

51. Troe, J. Specific rigidity factors in simple unimolecular bond fission reactions, *Journal of the Chemical Society-Faraday Transactions* **1997,** *93* , 885-891.

52. Troe, J. Statistical adiabatic channel model for ion-molecule capture processes .2. Analytical treatment of ion-dipole capture, *Journal of Chemical Physics* **1996,** *105* , 6249-6262.

53. Troe, J. Specific rigidity factors in simple unimolecular bond fission reactions, *Journal of the Chemical Society-Faraday Transactions* **1997,** *93* , 885-891.

CHAPTER 5: The heats of formation of $C_6H_5{}^\bullet$ $C_6H_5{}^+$ and C_6H_5NO by TPEPICO and Active Thermochemical Tables Analysis

5.1 Introduction

The development of the active thermochemical tables, in which the directly measured reaction energy differences are used to determine optimal heats of formations for the relevant species, has reinforced the importance of alternative routes that relate the various species. In this study we focus on the nitrosobenzene molecule, which dissociatively ionizes to form $C_6H_5{}^+$. The monosubstituted benzenes are often difficult systems to study by dissociative photoionization ($C_6H_5X + h\nu \rightarrow C_6H_5{}^+ + X$) because of slow dissociation near threshold and/or large uncertainties in the thermochemistry of the constituents. The active thermochemical tables[1,2] provide a reasonably accurate value for $\Delta_f H(C_6H_5{}^+)$ and $\Delta_f H(C_6H_5)$ and the neutral bond dissociation energy has been measured for nitrosobenzene.[3] Figure 5-1 shows that by measuring $E_0(C_6H_5{}^+)$ from nitrosobenzene, new values for $IE(C_6H_5)$ and $\Delta_f H(C_6H_5NO)$ can be determined.

A precise ionization energy of the phenyl radical has been difficult to determine experimentally. This is due to the poor Franck-Condon factors associated with the adiabatic transition from the ground electronic state of the radical to the ground singlet state of the phenyl ion. Difficulties in determining the phenyl radical and cation heats of formation have hindered thermochemical determination of $IE(C_6H_5)$. As a result, the two
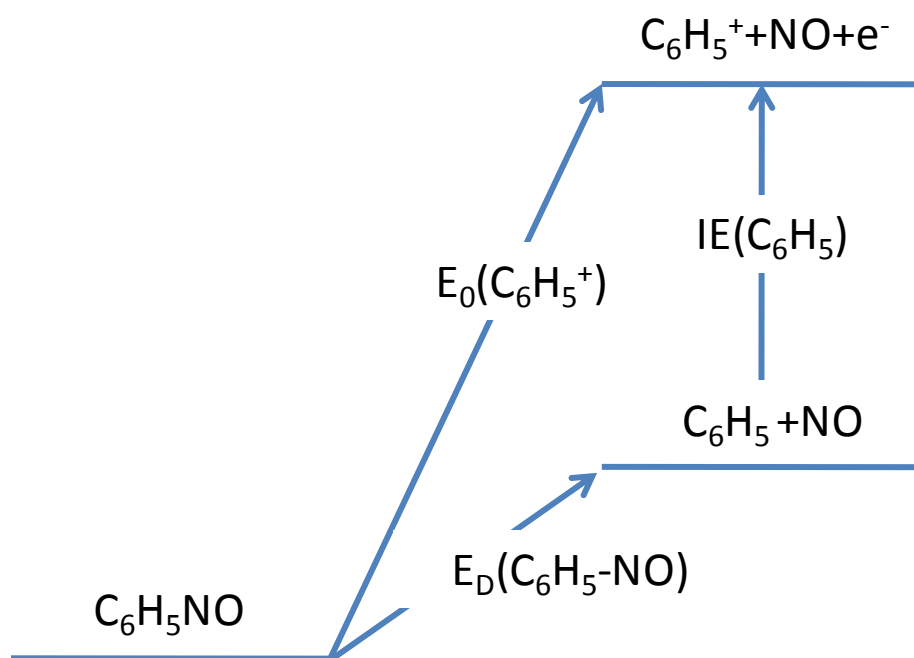
Figure 5-1 Energy diagram showing that the phenyl radical ionization energy is the difference between the onsets for C_6H_5 and $C_6H_5^+$.

previously reported measurements of the adiabatic IE(C_6H_5) differ by 200 meV, well

outside of their mutual uncertainty.[4,5] The first attempt to directly measure IE(C_6H_5) was

in 1972 by Sergeev et al.[4] who measured the appearance energy of the phenyl ion from

the phenyl radical, generated by pyrolysis of azobenzene , by photoionization mass

spectrometry to be 8.1 $\pm$ 0.1 eV. In 1987, Butcher et al.[5] determined the best

experimental value to date using photoelectron spectroscopy to measure an IE(C_6H_5) of

8.32 $\pm$ 0.04 eV. Low intensity due to low concentrations of the phenyl radical and poor

Franck Condon factors limited the precision of this measurement.

Previous attempts to calculate the IE(C_6H_5) have also been inconclusive in

determining the IE(C_6H_5) . In 1997 Hrusak et al. calculated, using single point CCSD(T)

calculations on B3LYP optimized geometries of the phenyl radical and cation, an IE of

8.1 $\pm$ 0.1 eV,[6] identical to the experimental value by Sergeev et al.[4] However, Lau and

Ng recently calculated a value of 8.261 eV[7] with an estimated uncertainty of 0.035 eV

by CBS extrapolation using the CCSD(T)/6-311++G method. This value is in mutual

agreement with the photoionization value reported by Butcher et al yet is well outside the

uncertainty of the value by Sergeev et al. Clearly this value merits further study.

Figure 5-1 demonstrates that the IE(C_6H_5) can be determined from the neutral bond

dissociation energy E_D(C_6H_5) and phenyl ion dissociation onset E_0($C_6H_5^+$) from the same

precursor. This has the advantage of not being dependent upon the thermochemistry

associated with the phenyl radical and ion or the benevolence of Franck-Condon factors.

The neutral BDE of nitrosobenzene (C_6H_5NO) has been determined by Park et al. to be

226.8 $\pm$ 2.1 kJ•mol^{-1}.[3] It is possible to determine E_0($C_6H_5^+$) using photoelectron-photoion

coincidence spectroscopy. However, the homolytic dissociation to the phenyl ion from

C_6H_5NO is immeasurably slow at threshold, requiring an extrapolation to determine $E_0(C_6H_5^+)$. This extrapolation requires the use of unimolecular rate theory. It has recently been shown that for the dissociation of the benzene, butyl benzene, and halobenzene cations, which also have immeasurably slow rate constants at threshold and no well defined transition state, the extrapolated zero Kelvin dissociation onset (E_0) is strongly dependent upon the rate model used.[8,9] For these systems Rice-Ramsperger-Kassel-Marcus (RRKM) theory, although capable of fitting the data over 4-5 orders of magnitude, significantly underestimates the E_0, while phase space theory (PST) does not fit the data very well, and tends to overestimate the E_0. On the other hand, a semi-empirical variational transition state theory (VTST)[10] and the simplified statistical adiabatic channel model (SSACM)[11,12] both were both capable of fitting the data and predicting the correct onset. However, the SSACM was found to be much easier to employ and is used here. More recent studies[13,14] have successfully employed this model to extrapolate accurate E_0 for both kinetic and competitive shifts.

Figure 5-1 shows that, in addition to using $E_0(C_6H_5^+)$ to determine $IE(C_6H_5)$, we can use the experimentally determined $E_0(C_6H_5^+)$ and $\Delta_f H^\circ_{0K}(C_6H_5^+)$ from the active thermochemical tables[15] to determine a new value for $\Delta_f H^\circ_{0K}(C_6H_5NO)$. Prior to this study, the only route to $\Delta_f H^\circ_{0K}(C_6H_5NO)$ has been by reported measurement of the bond dissociation energy of neutral C_6H_5NO.[3,16] Large uncertainties in both the $BDE(C_6H_5NO)$ and $\Delta_f H^\circ_{0K}(C_6H_5)$[17] have limited the uncertainty in $\Delta_f H^\circ_{0K}(C_6H_5NO)$ to about 3 kJ•mol^{-1}.

5.2   Thermochemistry and Energetics

Determining absolute thermochemistry of the constituents of the cycle in Figure 5-1 requires a species with known thermochemistry for calibration. Furthermore, the

uncertainty in that calibration species will propagate to any derived thermochemistry. Until recently, the uncertainty in $\Delta_f H_{0K}(C_6H_5^+)$ has been too large ($\pm$ 4 kJ•mol^{-1}) to significantly improve the thermochemistry of this cycle by measuring the E_0. However, a value of 1149.8 $\pm$ 2.1 kJ•mol^{-1} has been obtained by private communication[15] of results obtained using the Active Thermochemical Tables (ATcT).[1,18] Additionally, ATcT provides a value for $\Delta_f H_{0K}(C_6H_5)$ of 350.5 $\pm$ 0.8 kJ•mol^{-1}.[15]   Lastly, the $\Delta_f H_{0K}(NO)$ is well known and is reported by Chase[19] to be 89.77 $\pm$ 0.17 kJ•mol^{-1}.

Figure 5-1 shows that the E_0 can be determined from the sum of IE(C$_6$H$_5$) and E_D(C$_6$H$_5$). Using the ATcT values for $\Delta_f H_{0K}(C_6H_5^+)$ and $\Delta_f H_{0K}(C_6H_5)$, in combination with the E$_D$ determined by Lin et al., an E_0 of 10.584 $\pm$ 0.032 eV is obtained.

5.3   Results

Figure 5-2 shows the threshold photoelectron spectrum for C$_6$H$_5$NO. A detail of the first band shows some vibrational structure with a spacing of 205 cm^{-1} which we ascribe to a single vibrational mode. The reason for this is that if two or more modes had significant Franck-Condon factors for $\Delta v > 1$ transitions, the structure would disappear due to dephasing of the two or more slightly different vibrational modes. The electronic configuration of the ion is produced predominantly by the loss of the noboning lone pair electron from the nitrogen atom. This is confirmed by the calculated C-N-O bending mode which changes from 257 to 221 cm^{-1} and the corresponding angle change 116 to 134 °. , The experimentaly measured spacing of the PES peask is 200 cm^{-1}, which is close to the calculated ion frequency of 221 cm^{-1}. We therefore rely upon the IE predicted
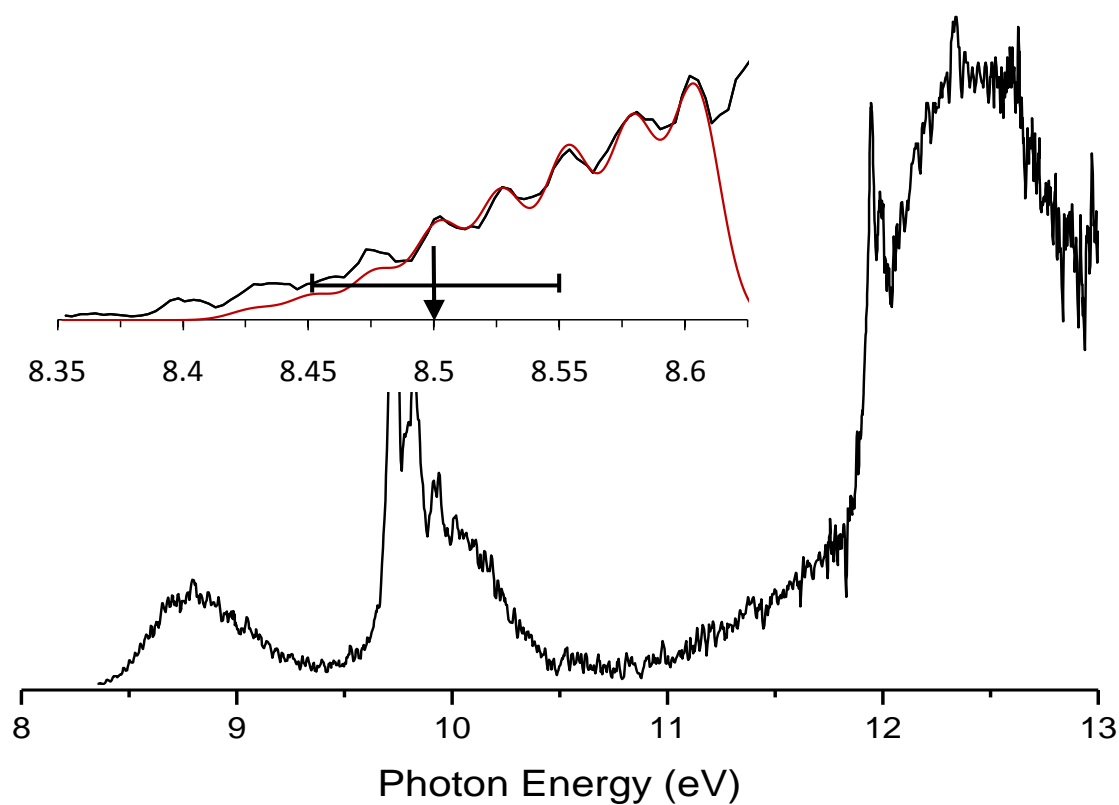
Figure 5-2 TPES of nitrosobenzene with zoom in of threshold region in inset. The red line corresponds to the modeled TPES (see text) and the arrow corresponds to the IE calculated by CBS-APNO with an estimated uncertainty of $\pm\,0.05$ eV.

to the calculated ion frequency of 221 cm^{-1}. We therefore rely upon the IE predicted

using CBS-APNO determined to be 8.50 ± 0.05 eV. As a check, we have taken a linear

combination of Gaussian functions with widths and centroids optimized to fit the

 experimental TPES. The coefficients were determined by assuming that each peak

corresponds to a single transition (*i.e.* the peaks at 8.475 eV and 8.525 eV are due solely

to the $v_1 \rightarrow v_0$' and $v_0 \rightarrow v_1$'transitions respectively) and that the Franck-Condon factors for

$v_i \rightarrow v_j$' transitions are equal to $v_j \rightarrow v_i$' transitions. This allows us to predict the intensity

of the hot bands independent of the Franck Condon factors by taking the ratio of the

$v_i \rightarrow v_j$' peak intensity to the $v_j \rightarrow v_i$' intensity The results from this approach are shown in

the inset of Figure 5-2. It is observed that this method somewhat underestimates the hot

band intensities which may be due to the assumption that each peak corresponds to a

single transition. Performing a similar analysis assuming a higher energy IE results in a

worse fit while a lower IE results in a better fit to the TPES. However it is not clear

whether this is due to an incorrect IE assignment, faulty assumptions in the model, or the

fact that at lower IE's the fit is less sensitive. A more sophisticated analysis of the TPES

may eliminate this ambiguity but is outside of the scope of this paper. We account for the

uncertainty in the IE(C_6H_5NO) by assigning a somewhat large error bars of 0.05 eV.

This error will be used in the modeling of the dissociative photoionization of the

C_6H_5NO.

Figure 5-3 shows representative TOF distributions of the parent fragment ions of

$C_6H_5NO^+$ at various photon energies, corrected for contamination from ionization events

that generated energetic electrons. The parent peak ($C_6H_5NO^+$) is observed at 24.0 μs.

The shoulder at slightly longer times of flight, observed in the TOF distribution at 10.58
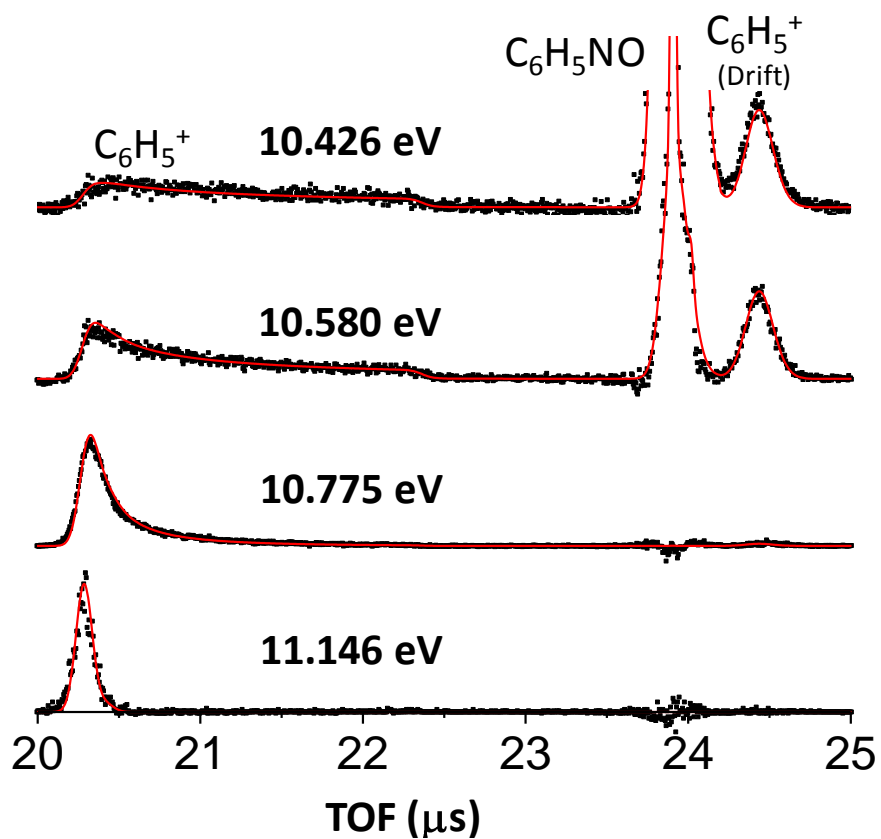
Figure 5-3 TOF distributions for nitrosobenzene over experimental window. Black Dots represent the experimental TOF distributions that have been corrected for ions that generated energetic electrons. Red lines indicate simulated TOF distributions.

eV, is due to the ^{13}C isotope peak. The rapidly dissociated fragment ions have a TOF of

20.32 μs. Slowly dissociating fragment ions in the first acceleration region show up as

asymmetric daughter ion time of flight distributions as shown in the data for the top three

TOF distributions in Figure 5-3. If the parent ion lives sufficiently long to enter the first

drift region, it will produce a fragment ion that has the same velocity, but a lighter mass,

thus less kinetic energy. These daughter ions are separated from their parent ions by

slowing them down in the last 10 cm of the drift region. Their reduced translational

energy causes them to be slowed down more than the parent ions and results in the

daughter ion peak at 24.5 μs. By analyzing the whole TOF distribution, it is possible to

derive a dissociation rate constant, which can be measured in the range between 10^3 and

10^7 s^{-1}.

Figure 5-4 shows the relative abundances of the fragment and parent peaks from

10.30 to 10.9 eV. The $C_6H_5NO^+$ intensity remains zero at photon energies greater than

10.8 eV. The two breakdown diagrams plotted in Figure 5-4 differ in how the fragment

peak at 24.5 μs is treated. In one case , labeled '7.0 μs' , this drift peak is added to the

parent peak area. The drift peak area is added to the fragment ion peak for the

breakdown diagram labeled '19.5 μs'. These two breakdown diagrams differ in the time

scale of the experiment.

5.3.1   Modeling of the TOF distributions and the breakdown diagrams.

The experimental data are modeled using experimental parameters and either

RRKM or SSACM. For both RRKM and SSACM the vibrational frequencies of the ion

were used to determine density of states, $\rho(E)$. For the RRKM treatment, the vibrational

frequencies of the ion equilibrium geometry were used for transition state frequencies
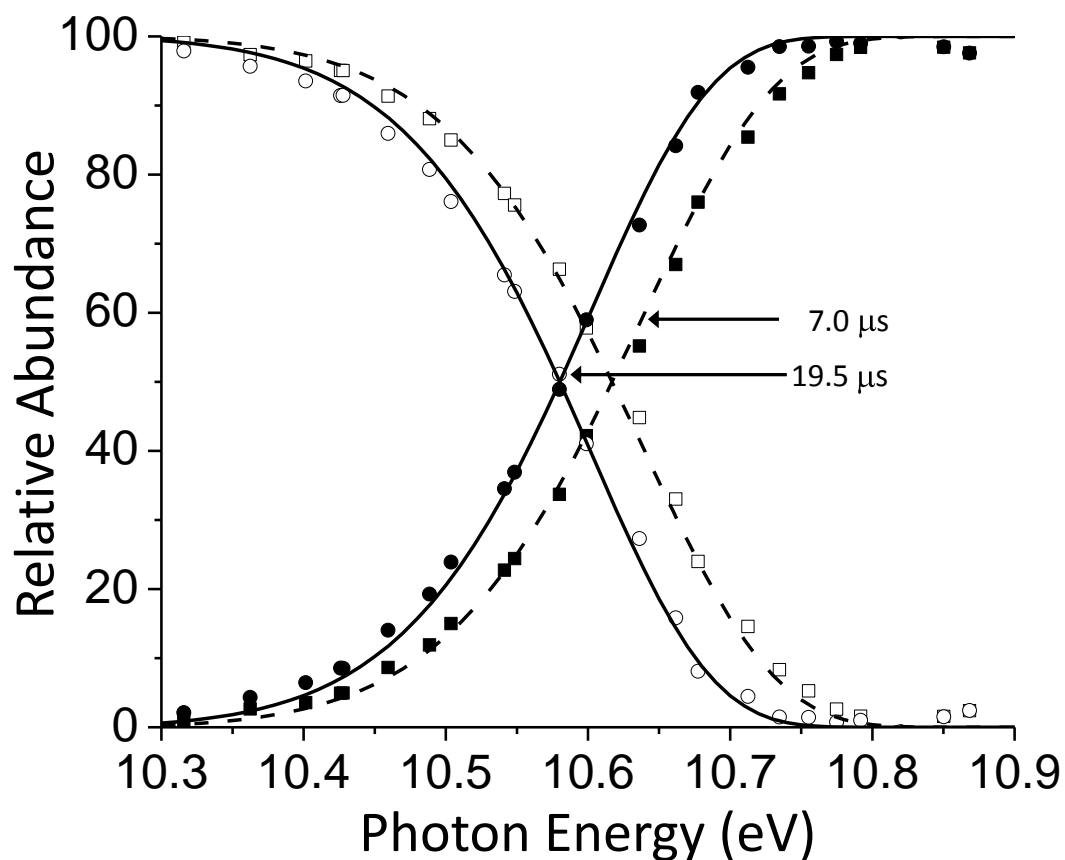
Figure 5-4Breakdown diagram for nitrosobenzene. The points represent the experimental relative abundances of the parent (open) and fragment (solid) ion at each photon energy. The lines are the simulated results.   The squares and dashed lines consider all fragment ions formed after 7 μs to be parent while the circles and solid lines consider fragment ion formed after 19.5 μs to be parent.

less the C-N stretching mode. In addition to the E_0, the 4 vibrational frequencies corresponding to the transitional modes were scaled to fit the data. For SSACM, the product vibrational frequencies and rotational constants are used to determine the phase space theory transition state. The rotational contribution to the transition state sum of states is scaled by an energy dependent rigidity factor $f(E)$:

$$f(E) = e^{-\left(\frac{E-E_0+IE}{c}\right)}$$ (5.1)

In addition to the E_0 and the IE, the variable, c, which is determined by the anisotropy of the interaction potential between the leaving neutral and fragment ion, was optimized to fit the data and to extract the limits of uncertainty for E_0. The modeled RRKM and SSACM curves are shown in Figure 5-5. The time of flight distributions are modeled by taking into account the thermal energy distribution of the room temperature sample. The RRKM and SSACM rate curves are essentially identical throughout the experimental window which extends over 4 orders of magnitude, but diverge at both higher and lower energies. At lower energies, the SSACM transition state is at the phase space limit and therefore has much stronger energy dependence than does the RRKM, so that SSACM predicts a higher E_0 than RRKM. Figure 5-5 also shows the calculated ion internal energy distribution for a single photon energy, which is obtained by assuming that the neutral thermal energy distribution is transposed to the ionic manifold. Because the ion internal energy distribution covers nearly the entire experimental window, it is impossible to obtain accurate k(E) information without accounting for the ion internal energy distribution. This is done by calculating TOF distributions at each ion internal energy and combining them, weighted by the ion internal energy distribution. The extrapolated
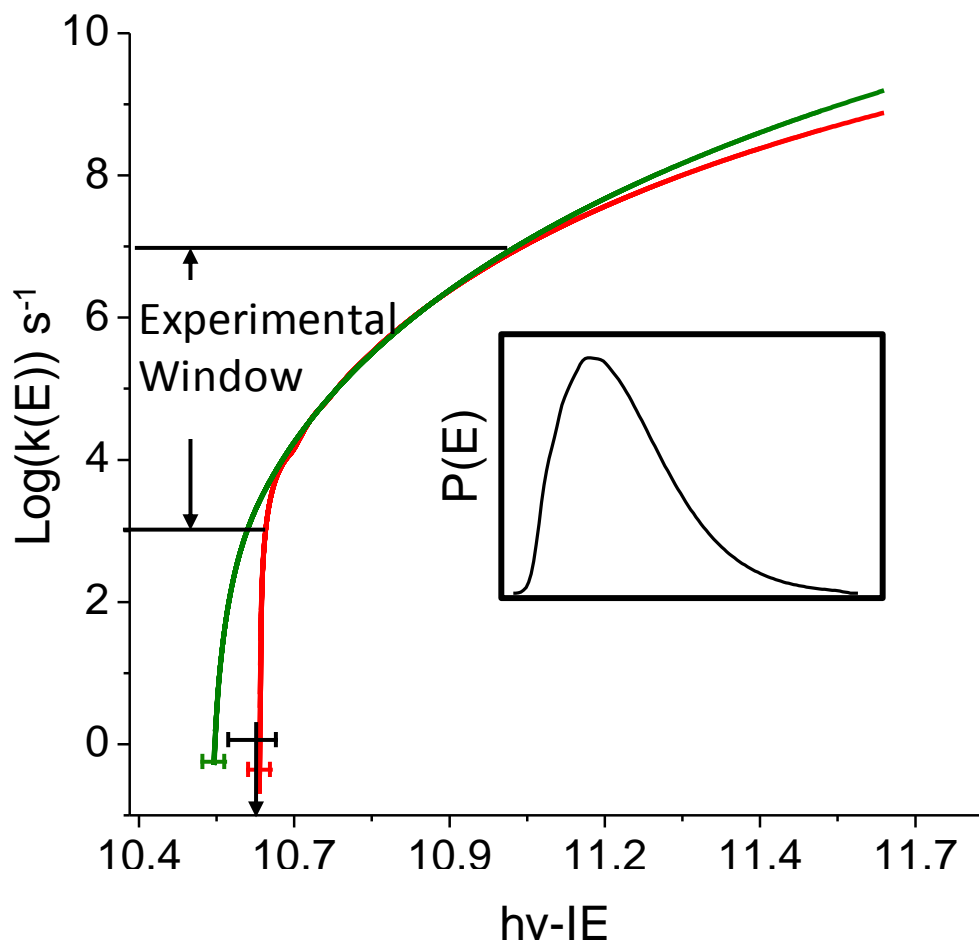
Figure 5-5 RRKM and SSACM rate curves and ion internal energy distribution used to fit the experimental data. The arrow indicates the location of the E_0 determined from current literature values (see text). The error bars represent uncertainties in the extrapolated onset by SSACM and RRKM.

E_0s are 10.533 ± 0.02 eV and 10.607 ± 0.02 eV for RRKM and SSACM respectively.

For both rate models, the somewhat large uncertainty in IE(C_6H_5NO) was taken into account when computing the uncertainties in the E_0's. However, because the ionic dissociation energy (E_0-IE(C_6H_5NO)) changes to offset changes in the IE(C_6H_5NO), this had a negligible effect on the uncertainty in E_0. SSACM fits to the data were obtained with a fitting parameter c of 100 meV. For RRKM, fits were obtained by scaling the transitional frequencies by 0.12, indicating a very loose transition state with an entropy of activation of 66 J/mol•K. Although good agreement between the two models is observed within the experimental window, they extrapolate to different E_0's. Previous studies have shown that the RRKM model extrapolates to E_0 values that are to low, and so we utilize the SSACM results for extracting thermochemical information.

5.3.2 The heat of formation of C_6H_5NO

The determined E_0 (10.607 ± 0.02) provides access to the $\Delta_f H$(C_6H_5NO) from the known $C_6H_5^+$ and NO heats of formation. Using these values we obtain a $\Delta_f H_{0K}$(C_6H_5NO) of 216.1 ± 2.6 kJ•mol^{-1}. This value is within mutual uncertainty of the $\Delta_f H$(C_6H_5NO) derived from the neutral BDE of C_6H_5NO and C_6H_5 and NO heats of formation of 213.5 ± 2.25 kJ•mol^{-1} and the higher value determined by Choo et al. of 218.3 ± 4.2 kJ•mol^{-1}.[16]

5.3.3 The ionization energy of C_6H_5

According to Figure 5-1, there are two paths for determining the IE(C_6H_5). The first route is to take the difference between the Active Tables heats of formation of the phenyl radical and ion. Using the values reported in Table 5- 1 results in an IE(C_6H_5) of 8.284 ± 0.023 eV. The second route is by taking the difference between the E_0 and the

neutral BDE reported by Lin et al., which results in an IE(C_6H_5) of 8.257 ± 0.029 eV.

These values are independent of one another, we can therefore reduce the uncertainty in

the $\Delta_fH(C_6H_5NO)$ by taking an uncertainty weighted mean of the two values using the

equation below.

$$\bar{x} = \frac{\sum_i x_i \sigma_i^{-2}}{\sum_i \sigma_i^{-2}} \tag{5.2a}$$

$$\bar{\sigma} = \left(\sum_i \sigma_i^{-2}\right)^{-\frac{1}{2}} \tag{5.2b}$$

Where x_i corresponds to the individual values of IE(C_6H_5) and σ_I are the uncertainties in

those values. This method results in an IE of 8.273 ± 0.018 eV. This value is within

mutual uncertainty of the IE(C_6H_5) determined by Butcher et al[5] and in good agreement

with the IE(C_6H_5) calculated by Lau andNg.[7]

Table 5- 1. Derived and Ancillary Thermochemistry and Energetics.

	Δ_fH_{0K} (kJ•mol^{-1})	Δ_fH_{298K} (kJ•mol^{-1})	H_{298}-H_0 (kJ•mol^{-1})	IE (eV)	E_0 (eV)	D_0 (eV)
C_6H_5NO	216.1 ± 2.6^a	198.8 ± 2.6	18.8	8.50 ± 0.05^b	10.607 ± 0.02 ^{a}	2.350 ± 0.022^c
C_6H_5	350.5 ± 0.8^d	337.2 ± 0.8	15.7	8.273 ± 0.018^a		
$C_6H_5^+$	1149.8 ± 2.1^d	1138.0 ± 2.1	14.2			
NO	89.775 ± 0.17^e					

^{a} Determined in the present study.
^{b} Calculated using CBS-APNO
^{c}Park 1997[3]
^{d}ATcT value[15]
^{e}Chase 1998[19]

5.4 Conclusion

The 0 K dissociation onset for nitrosobenzene has been determined by SSACM

modeling of data obtained by TPEPICO to be 10.607 ± 0.02 eV. Using this value the

heat of formation of nitrosobenzene has been determined to be 216.1 ± 2.6 kJ•mol^{-1}.

Using the E_0 determined in this study and the previously determined neutral bond energy

of nitrosobenzene,[3] in combination with the ATcT values for $\Delta_f H_{0K}(C_6H_5)$ and

$\Delta_f H_{0K}(C_6H_5^+)$, a new value for the phenyl radical IE has been determined to be 8.273±

0.018 eV. This is in good agreement with the value calculated by Ng. et al and with

mutual uncertainty of the IE experimentally determined by Butcher et al.

Reference List

1. Ruscic, B.; Pinzon, R. E.; Morton, M. L.; Laszevski, G.; Bittner, S. J.; Nijsure, S. G.; Amin, K. A.; Minkoff, M.; Wagner, A. F. Introduction to Active Thermochemical Tables: Several "Key" Enthalpies of Formation Revisited, *J. Phys. Chem. A* **2004,** *108* , 9979-9997.

2. Ruscic, B.; Pinzon, R. E.; Morton, M. L.; Laszevski, G.; Bittner, S. J.; Nijsure, S. G.; Amin, K. A.; Minkoff, M.; Leahy, D.; Montoya, D.; Wagner, A. F. Active Thermochemical Tables: thermochemistry for the 21st century, *J. Phys. Conf. Ser.* **2005,** *16* , 561-570.

3. Park.J.; Dyakov, I. V.; Mebel, A. M.; Lin, M. C. Experimental and Theoretical Studies of the Unimolecular Decomposition of Nitrosobenzene: High-Pressure Rate Constants and the C-N Bond Strength, *J. Phys. Chem. A* **1997,** *101* , 6043-6047.

4. Sergeev, Y. L.; Akopyan, M. E.; Vilesov, F. I. Photoionization of the phenyl radical, *Opt. Spect.* **1972,** *32* , 230-231.

5. Butcher, V.; Costa, M. L.; Dyke, J. M.; Ellis, A. R.; Morris, A. A study of the phenyl radical by vacuum ultraviolet photoelectron spectroscopy, *Chem. Phys.* **1987,** *115* , 261-267.

6. Hrusak, J.; Schröder, D.; Iwata, S. The ground state ($^1A_1$) and the lowest triplet state ($^3B_1$) of the phenyl cation $C_6H_5^+$ revisited., *J. Chem. Phys.* **1997,** *106* , 7541-7549.

7. Lau, K.-C.; Ng, C. Y. Accurate ab initio predictions of ionization energies and heats of formation for the 2-propyl, phenyl, and benzyl radicals, *J. Chem. Phys.* **2006,** *124* , 044323-1-044323/9.

8. Troe, J.; Ushakov, V. G.; Viggiano, A. A. On the Model Dependence of Kinetic Shifts in Unimolecular Reactions: The Dissociation of the Cations of Benzene and n-Butylbenzene, *J. Phys. Chem. A* **2006,** *110* , 1491-1499.

9. Stevens, W.; Sztáray, B.; Shuman, N.; Baer, T.; Troe, J. Specific Rate Constants k(E) of the Dissociation of the Halobenzene Ions: Analysis by Statistical Unimolecular Rate Theories, *J. Phys. Chem. A* **2009,** *113* , 573-582.

10. Chesnavich, W. J.; Bass, L.; Su, T.; Bowers, M. T. Multiple transition states in unimolecular reactions: A transition state switching model. Application to the $C_4H_8^+$ system, *J. Chem. Phys.* **1981,** *74* , 2228-2246.

11. Troe, J. Towards Simplified Thermal and Specific Rigidity Factors for Ion-Molecule Reactions and Ion Fragmentations, *Z. Phys. Chem.* **2009,** *223* , 347-357.

12. Baer, T.; Hase, W. L. *Unimolecular Reaction Dynamics: Theory and Experiments;* Oxford University Press: New York, 1996.

13. Stevens, W. R.; Walker, S. H.; Shuman, N. S.; Bodi, A.; Baer, T. Threshold photoelectron photoion coincidence study of neopentane, t-butyl iodide and t-butyl hydrogen peroxide: The heat of formation of the t-butyl ion. Unpublished Work, 2009.

14. Shuman, N. S.; Spencer, A. P.; Baer, T. Experimental Thermochemistry of SiCl3R; (R = Cl, H, CH3, C2H5, C2H3, CH2Cl, SiCl3, SiCl3+, and SiCl3), *J. Phys. Chem. A* **2009,** *113* , 9458-9466.

15. Ruscic, B. Private communication of interim ATcT results based on the Core (Argonne) Thermochemical Network ver. 1.078. Unpublished Work, 2009.

16. Choo, K. Y.; Golden, D. M.; Benson, S. W. Very-low-pressure pyrolysis of nitroso- and pentafluoronitrosobenzene C-NO bond dissociation energies, *Int. J. Chem. Kin.* **1975,** *7* , 713-724.

17. Blanksby, S. J.; Ellison, G. B. Bond Dissociation Energies of Organic Molecules, *Acc. Chem. Res.* **2003,** *36* , 255-263.

18. Ruscic, B.; Pinzon, R. E.; Morton, M. L.; Laszevski, G.; Bittner, S. J.; Nijsure, S. G.; Amin, K. A.; Minkoff, M.; Leahy, D.; Montoya, D.; Wagner, A. F. Active Thermochemical Tables: thermochemistry for the 21st century, *J. Phys. Conf. Ser.* **2005,** *16* , 561-570.

19. Chase, M. W. *NIST-JANAF Thermochemical Tables;* 4th ed.; American Institute of Physics: New York, 1998.

CHAPTER 6: Dissociative Photoionization Study of Neopentane: A path to an accurate heat of formation of the *t*-butyl ion, t-butyl iodide, and t-butyl hydroperoxide

6.1 Introduction

The *t*-butyl cation is a very stable ion, yet a high precision ($\pm$ 1-2 kJ•mol^{-1}) direct determination of its heat of formation, $\Delta_f H°(t\text{-}C_4H_9^+)$, has proven to be difficult. An attractive route for obtaining ionic heats of formation is via dissociative photoionization, $t\text{-BuR} + h\nu \rightarrow t\text{-Bu}^+ + R + e^-$. If the precursor molecule, t-BuR, and the neutral fragment, R, have known energetics, an onset energy can be used to obtain the heat of formation of t-Bu$^+$. However, the high stability of the ion actually causes a complication in that the parent ion is in many cases unbound, causing the dissociative photoionization onset to reflect only the ionization energy of the neutral.

Another approach involves measuring the ionization energy of the *t*-butyl radical[1,2] and obtaining the ion heat of formation using the t-butyl radical as the anchor. However, the large geometry change from tetrahedral to trigonal planar causes the Franck-Condon factors for the $v_i \rightarrow v_i'$ transition to be very weak, thus enhancing hot band transitions. Making matters even worse, the *t*-butyl radical is typically formed via

pyrolysis at temperatures in excess of 800 K, thus making an accurate determination of the IE of the *t*-butyl radical problematic. These difficulties are illustrated in the various reported IE's which are, in chronological order, 6.58± 0.01 eV,[1] 6.70 ± 0.03 eV,[2] and a recent unpublished result of 6.77 ± 0.02 eV[3]

The final route to the *t*-butyl ion heat of formation is via calculations.[4] Its closed shell structure makes this an attractive alternative to experimental approaches. However, in order to improve upon experimental values for $\Delta_f H^{\circ}_{0K}(t\text{-}C_4H_9^+)$, such calculations would have to be reliable to within 2.5 kJ•mol[-1]. Such precision would require the highest level of theory (*e.g.* W4[5] or HEAT[6] methods). To date no such calculations have been reported.

The best experimental measurements of the *t*-butyl ion heat of formation have come from dissociative photoionization measurements with neopentane,[7,8] *t*-butyl iodide,[9-11] and possibly isobutane,[8,12] all of which have stable parent ions and yield *t*-butyl ions as products. The first such measurement was reported by Steiner et al.[7] in which they measured the onset of the *t*-butyl ion from neopentane at various temperatures using photoionization mass spectrometry (PIMS). The problem with such experiments is that the onset energy is ill defined because the shape of the PI curve is a function of the molecule's thermal energy, the shape of the photoelectron spectrum, the rate at which the ion dissociates, and competition with lower energy dissociation channels. Usually, a "straight line" portion of the fragment ion PI signal is extrapolated to intersect with the energy axis. This phenomenological appearance energy must then be related to the 0 K dissociation limit. By observing the shift in this appearance energy with temperature, Steiner et al. derived a 0 K CH_3 loss onset energy of 10.56 ± 0.020 eV. The lower energy

CH_4 loss onset was reported as 10.39 ± 0.020 eV.[7] A rather strange finding in these neopentane data was that the onsets hardly shifted as the temperature was varied. In the case of the CH_3 loss reaction, The 0 K onset of 10.56 ± 0.02 eV was extrapolated from the 10.53 (150°C) and 10.55 (28°C) eV onsets. As they pointed out, this 15 meV shift was only 11 % of the expected shift if all the neopentane thermal energy were available for dissociation. The only other PIMS study of neopentane was carried out by Traeger[8] in 1996 who reported 298 K onsets of 10.38 ± 0.02 and 10.33 ± 0.01 eV for CH_3 and CH_4 loss steps. It is instructive to note that the 0.17 eV discrepancy between the Inghram and Traeger 298 K methyl loss onsets stems from the choice of the straight line portion of the PIMS curve chosen by the two groups. However, because Traeger used the full thermal correction, whereas Inghram et al. used their measured extrapolation, the two 0 K values (10.56 and 10.54 eV, respectively) end up being quite similar. Neither group took into account any correction for the interference of the lower energy CH_4 loss channel.

For a number of years, the isobutene proton affinity (PA) accepted by the thermochemical community[13] was based on the 1979 Houle and Beauchamp[2] adiabatic ionization energy of the t-butyl radical (6.70 ± 0.03 eV) by HeI photoelectron spectroscopy (PES), and a 1979 PIMS study of the H loss reaction from isobutane.[12] Their derived heats of formation of 681.5 ± 5 kJ •mol^{-1} and 678.5 ± 3 kJ•mol^{-1} agreed to within their mutual uncertainty. However, a decade later Radom and co-workers undertook an extensive theoretical study defining the PA scale using the G2 method.[14] The study noted a significant and systematic discrepancy between calculated and experimental values, which would be rectified were the accepted isobutene PA anchor too positive by roughly 20 kJ•mol^{-1}. Further G2 calculations suggested a t-butyl cation

298 K heat of formation of 716 kJ•mol^{-1},[4] prompting a reevaluation of the experimental results. Apparently, an uncertain IE measurement of the t-butyl radical coupled with an even less certain t-butyl radical heat of formation caused the resulting t-butyl ion heat of formation to be in error. The PIMS measurement on isobutane, later corrected by Traeger,[8] suffered from t-C$_4$H$_9$Cl contamination in addition to the fact that the H loss reaction accounts for less than 1% of the yield because of competition with methane loss, which makes its PIMS onset determination very unreliable.

In search of another route for establishing the t-butyl ion heat of formation, Keister et al.[10] used a supersonically cooled beam of t-butyl iodide and collected threshold photoelectron photoion coincidence (TPEPICO) spectra at energies near the dissociation limit for I atom loss. They extracted a 0 K onset energy of 9.180 ± 0.015 eV, which yielded a 298 K t-butyl cation heat of formation of 711 ± 3.6 kJ•mol^{-1}, in good agreement with the calculated G2 results for Radom. However, this analysis was marred by low signal level due to the molecular beam, a significant contribution of hot electrons to the spectrum, and the ± 3.3 kJ•mol^{-1} uncertainty in the t-butyl iodide heat of formation. Although the data were modeled by taking into account the contaminating hot electrons, the derived onset is less than firm. More recently, Kim et al.[11] determined the I loss onset from t-butyl iodide ions by mass analyzed threshold ionization (MATI) in which t-butyl iodide cooled in a molecular beam was ionized by a vacuum UV laser and the parent and daughter ion signals monitored as a function of the laser energy. Although the data are somewhat less than convincing, they derived an onset of 9.176 ± 0.004 eV, which agrees well with the 9.180 ± 0.015 eV TPEPICO onset of Keister et al.[10] These two measurements are probably the most consistent and best values for determining the t-

butyl ion heat of formation. However, the t-butyl iodide heat of formation is known to only 3.3 kJ•mol^{-1}, an uncertainty that is then transferred to the t-butyl ion. So, this route is also not optimum for obtaining an accurate value for the t-butyl ion heat of formation.

The fundamental problem in establishing an accurate heat of formation of the t-butyl ion by dissociative photoionization is that of the few systems that dissociate simply to form t-C$_4$H$_9^+$ (*i.e.* no lower energy pathways, stable parent ion, etc.) none have established heats of formation. Two reactions, the previously mentioned t-butyl iodide and the not yet investigated t-butyl hydroperoxide, yield the t-butyl ion fall into this category. On the other hand, neopentane has a very well established heat of formation of 167.9 ± 0.8 kJ•mol^{-1},[15] which is based on a bomb calorimetry measurement. In addition, high level quasi W4 level calculations by Karton et al.[16] on a variety of hydrocarbons, including neopentane, have reported a value of -166.0 kJ/mol, which agrees reasonably well with the experimental value of Good. However, the methyl loss reaction for this ion is in competition with a lower energy methane loss, which makes the extraction of the higher energy onset difficult.   Fortunately, recent progress in our laboratory in modeling complex dissociation paths involving both parallel and sequential reactions[17] gives us the opportunity to extract a high quality onset for the methyl loss reaction in the presence of the slightly lower energy methane elimination.   An accurate heat of formation for the t-butyl ion then allows us to obtain an accurate heat of formation of the t-C$_4$H$_9$I and t-C$_4$H$_9$OOH, as well as a more reliable proton affinity of the isobutene molecule.

6.2 Results

We begin with the more easily analyzed t-butyl iodide and t-butyl hydroperoxide results. Both dissociations proceed through a single channel at a rate much faster than the microsecond time scale of the experiment.

6.2.1 *t*-Butyl Iodide

The relative abundances of the parent and fragment peaks are plotted as a function of photon energy in Figure 6-1 for t-C_4H_9I (i.e. a breakdown diagram). The only product ion observed over this energy range is the t-$C_4H_9^+$ ion. Additionally the *t*-$C_4H_9^+$ peak is symmetric at low energies, indicating that the dissociation rate is faster than the timescale of our apparatus ($>10^7$ s-1).

When the dissociation rate is fast, the E_0 for the lowest energy dissociation pathway is located at the energy at which the parent ion disappears. However, for large ions with many vibrational degrees of freedom, the precise energy at which the parent ion disappears is poorly defined and modeling is necessary to determine this 0 K dissociation energy. The ion internal energy, relative to the ground state of the ion, is given by $E_{ion}(h\nu) = h\nu - IE + E_{Th}$, where IE is the adiabatic ionization energy and $h\nu$ is the photon energy. If $P(E)$ is the normalized thermal energy distribution of the ion, then the relative abundance of *t*-$C_4H_9I^+$, $BD_{C4H9I}(h\nu)$, is determined by the portion of the ion internal energy distribution that lies below the 0 K dissociation threshold $E_0(t\text{-}C_4H_9^+)$:

$$BD_{C_4H_9I^+}(h\nu) = \int_0^{Eo-h\nu} P(E)dE \quad for\ h\nu < E_0 \tag{6.1}$$

The relative fragment ion abundance is then

$$BD_{C4H9}(h\nu) = 1 - BD_{C4H9I}(h\nu) \tag{6.2}$$

When the photon energy exceeds E_0, the fractional parent and daughter ion signals remain 0 and 1, respectively.

It is often possible to assume that the internal energy distribution of the neutral molecule is faithfully transposed to the ionic manifold upon ionization.[18] However, this assumption may fail when the ion and neutral geometries are significantly different. This geometry change causes low Franck-Condon factors for $v_i \rightarrow v_i'$ transitions and therefore a different internal energy distribution for the ion. Such a case was found in the ionization of $SiCl_3H$ [19] for which the ion structure has an elongated Si-H bond and a nearly planar $SiCl_3$ subgroup, relative to the neutral. As a result, the ion vibrational modes are much looser, and the ion internal energy distribution is best described by a temperature 22 K higher than that of the neutral. Similar results are observed for all three systems studied here. Unfortunately, we are unable to describe these changes quantitatively in order to predict the ion energy distribution and must treat the distribution as an additional fitting parameter. This extra parameter increases the uncertainty in the E_0 by about a factor of two for the case of t-butyl iodide. The best fit E_0 (Figure 6-1) was 9.170 ± 0.007eV with an optimized temperature of 280 K for the nominal temperature of 260 K. This is within the experimental error of the previous TPEPICO measurement by Keister et al.[10] (9.18 ± 0.015 eV) as well as the laser based MATI value of 9.176 ± 0.004 eV.[11] Table 6-1 summarizes the current and previously measured onset energies.

6.2.2 t-Butyl hydroperoxide

The breakdown diagram for t-C_4H_9OOH is shown in Figure 6-2. As with t-C_4H_9I, eq. 6.1 can be used to determine $E_0(t$-$C_4H_9^+)$. The B3LYP optimized structures of the ion
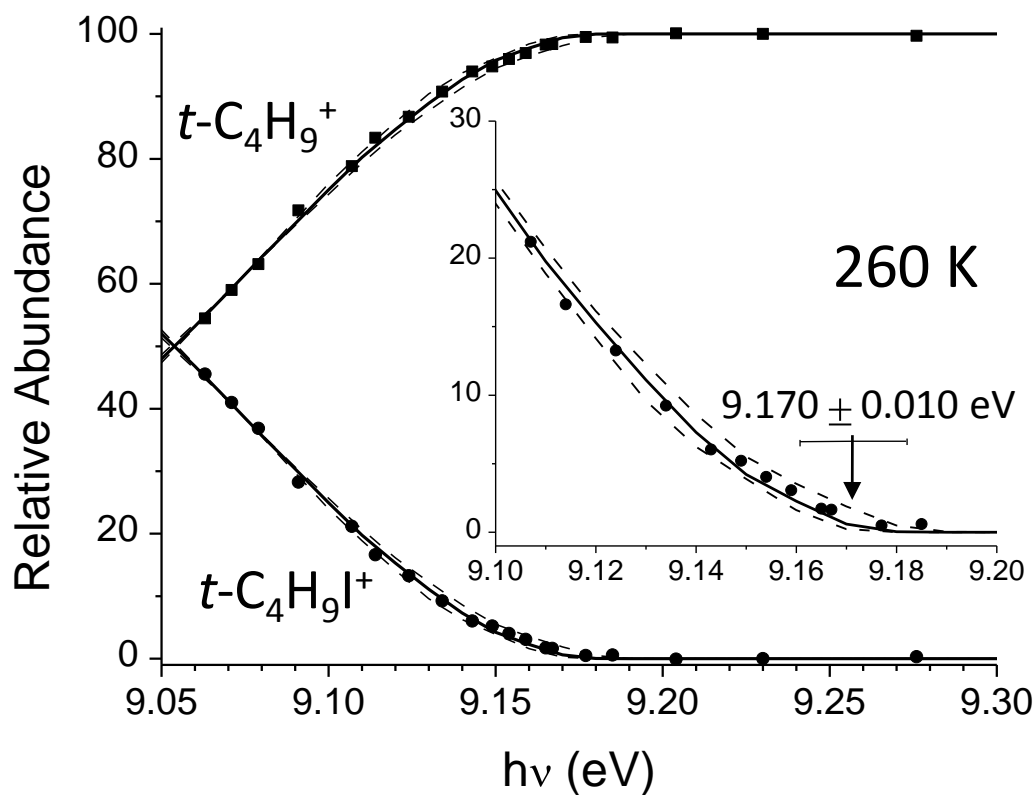
Figure 6-1 *t*-butyl iodide breakdown diagram acquired at 260 K. Points are experimentally measured ion abundances. Solid line is the bes*t*-fit simulation of the data (see text); dashed lines are the simulated fits at the edges of the reported uncertainty. The inset graph is an expanded view of the breakdown diagram in the energy range of the determined onset.

Table 6-1 Comparison of $E_0(t\text{-}C_4H_9{}^+)$ (in eV) with previously determined studies.

Precursor	Ion	AE_{298K}	E_0	Δ
$t\text{-}C_4H_9I$	$t\text{-}C_4H_9{}^+$	$8.98^{a,c}$		0.01
		$8.99^{b,c}$		0.01
			9.16^{d}	0.03
			9.18^{e}	0.015
			9.176^{f}	0.005
			9.170^{g}	0.010
$t\text{-}C_4H_9OOH$	$t\text{-}C_4H_9{}^+$		9.904^{g}	0.012
$(CH_3)_4C$	$t\text{-}C_4H_9{}^+$	10.55^{h}	10.56^{h}	0.02
		10.38^{b}	10.53^{i}	0.02
			10.564^{g}	0.025
	$C_4H_8{}^+$	10.37^{h}	10.39^{h}	0.02
		10.33^{b}	10.48^{i}	0.01
			10.397^{g}	0.010

[a] McLoughlin and Traeger 1979;[12] [b]Traeger 1996;[8] [c]These values reflect the ionization energy of $t\text{-}C_4H_9I$ and were therefore not converted to E_0; [d]Oliveira, Olesik, Almoster Ferreira and Baer 1988;[9] [e]Keister, Riley and Baer 1993;[10] [f]Park, Kim and Kim 2001;[11] [g]These values were obtained in the current study; [h]Steiner, Giese and Inghram 1961;[7] [i]Only AE_{298} values were reported, an E_0 was determined by adding the neutral internal energy ($<E_{vib}>+<E_{rot}>$) of 0.15 eV to AE_{298} .and neutral molecules show a change in ion geometry where the central carbon moves into the same plane as the methyl groups and the C-O bond length increases. As with t-butyl iodide, the temperature used to fit the experimental breakdown diagram was higher than the neutral temperature. The determined E_0 was 9.904 ± 0.012 eV with a temperature of 330 K for a nominal temperature of 298 K.

6.2.3 Neopentane

TOF spectra of $(CH_3)_4C$ taken at 223 K (LinTOF), 260 K (Re TOF), and 298 K (LinTOF) are shown in Figure 6-2. Spectra taken with the ReTOF with its resolution of 350 have clearly resolved m/Z 56 ($C_4H_8^+$) and m/Z 57 (t-$C_4H_9^+$ and $^{13}C_4H_8^+$) peaks. Spectra taken with the LinTOF mass analyzer, resolution of 100, have these peaks less well resolved so that the peak areas are determined by fitting the spectra with a linear combination of Gaussian functions.

The breakdown diagrams corresponding to the three different temperatures for neopentane are shown in Figure 6-3. Because the dissociation is fast, the breakdown diagrams are not dependent upon the total flight time, and therefore independent of which apparatus (the LinTOF or the ReTOF) was used. Poor Franck-Condon factors and low photon intensity at the ionization threshold cause the increased scatter at lower photon energies observed in the breakdown diagrams.

Figure 6-3 shows that the appearance of t-$C_4H_9^+$ is slightly higher in energy than $C_4H_8^+$. This means that in order to obtain $E_0(t$-$C_4H_9^+)$, both dissociation channels must be modeled simultaneously. Methane loss is the lowest energy channel and as a result the 0K dissociation energy, E_{CH4}, is obtained as was described above for t-C_4H_9I. However, the higher energy competitive loss of the methyl group is more complicated because there
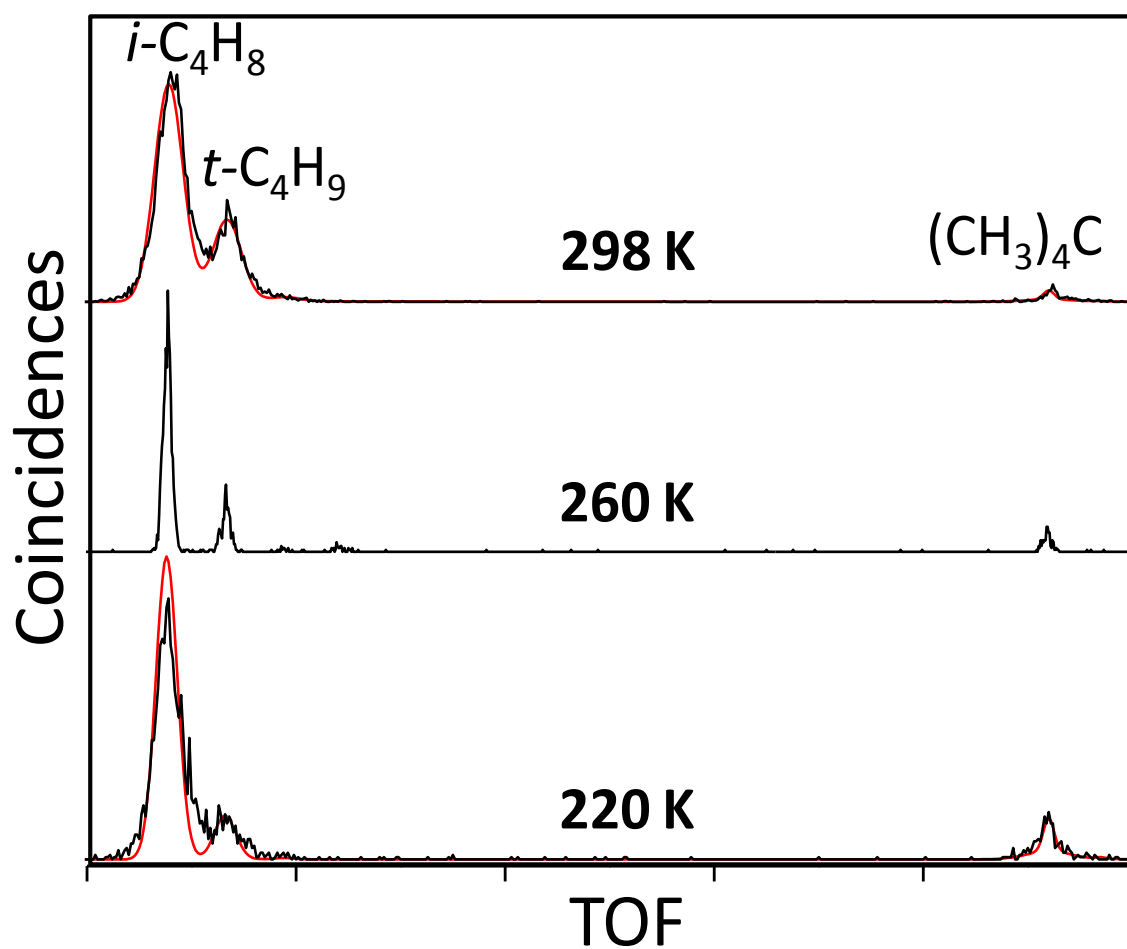
Figure 6-2 Experimental neopentane mass spectra acquired at various temperatures. The 260 K spectrum used a ReTOF analyzer at a photon energy of 10.365 eV while spectra acquired at 220 K and 298 K used the LinTOF mass analyzer at 10.345 and 10.373 eV. The 260 K spectrum has been scaled so that the masses are aligned with the linear TOF spectra
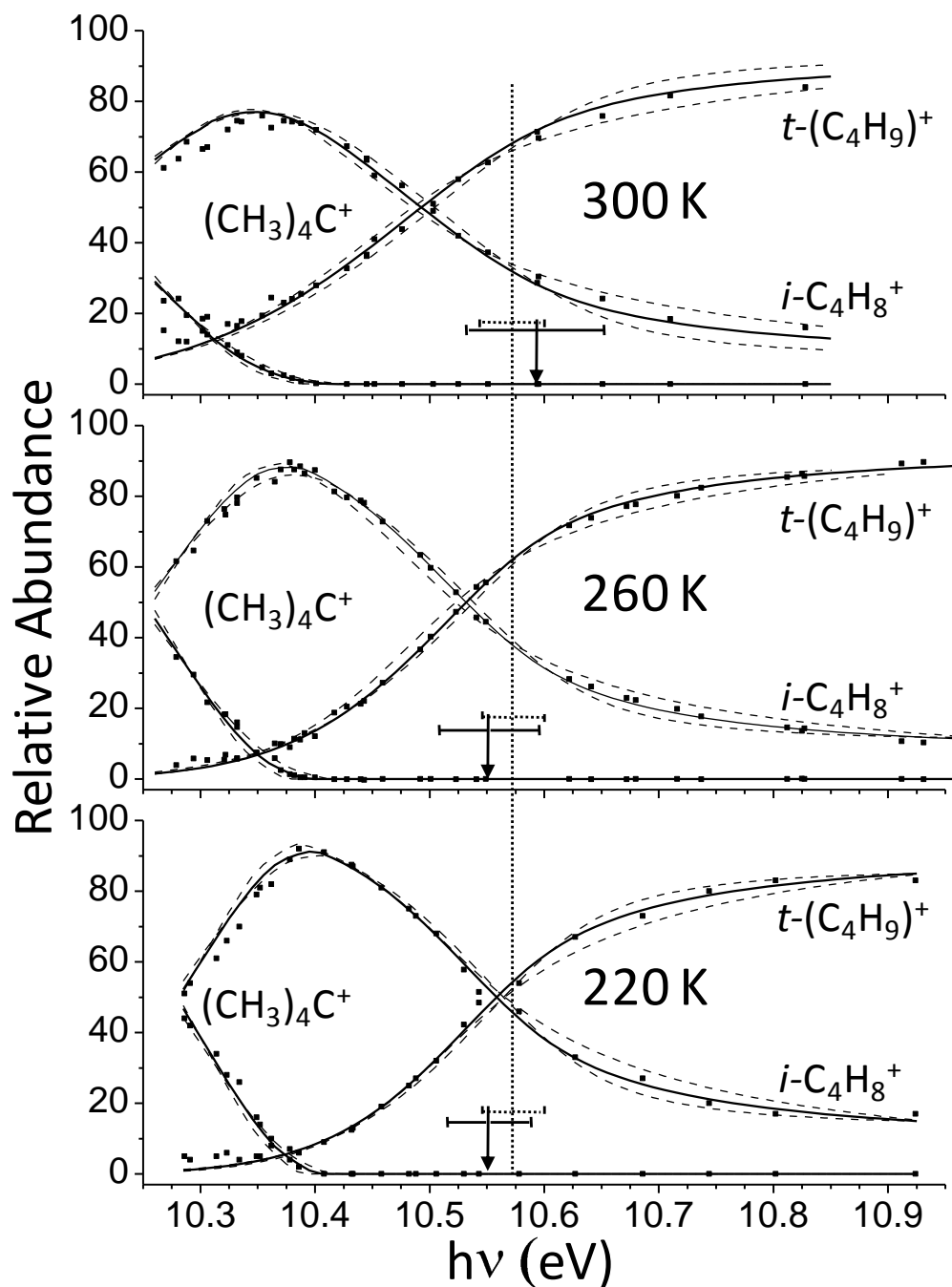
Figure 6-3 Breakdown Diagrams for neopentane acquired at 220 K, 260 K and 300 K. The arrows indicate the best fit E0(t-C4H9+) and the whiskers indicate their uncertainties. The dotted line indicates the weighted average of the three E0(t-C4H9+). The dashed lines represent the upper and lower limits of acceptability of the fit to the data.

is no feature in the breakdown diagram (e.g. the energy at which the parent ion disappears) from which the E_0 (t-$C_4H_9^+$) can be directly measured. Instead, the breakdown diagram reflects only the relative rates of the competing dissociation channels.[17] Using the statistical theory, the branching ratio at an ion energy, E, measured relative to the ground state ion, can be calculated using eqn. 6.3:

$$\frac{[C_4H_8^+]}{[t\text{-}C_4H_9^+]} = \frac{k_{C_4H_8^+}(E)}{k_{C_4H_9^+}(E)} = \frac{\sigma_{C_4H_8^+} N^{\ddagger}(E - E_{CH4} + IE)}{\sigma_{t\text{-}C_4H_9^+} N^{\ddagger}(E - E_0(t\text{-}C_4H_9^+) + IE)} \qquad (6.3)$$

where the IE is assumed to be 10.21 eV,[20] σ represents the reaction symmetry numbers, which are 3 and 1 for $C_4H_8^+$ and t-$C_4H_9^+$ formation, respectively, and $N^{\ddagger}$ is the transition state sum of states for the two dissociation pathways. Because the branching ratio is known over the experimental range, if $k(E)$ for $C_4H_8^+$ formation is known then, according to eqn. 6.3, the $k(E)$ over the same energy range for t-$C_4H_9^+$ is also known.

The best fit E_{CH4}'s were 10.396 ± 0.014, 10.391 ± 0.019 and 10.408 ± 0.021 eV with optimized temperatures of 280 ± 20 K, 300 ± 30 K and 370 ± 30 K for the nominal temperatures of 220 K, 260 K, and 298 K respectively. The uncertainties in the E_{CH4} were obtained by varying the assumed temperatures by the indicated amounts. The E_{CH4} and the assumed temperature are quite independent of each other in that changing E_{CH4} translates the modeled curve, while the temperature varies its slope. These uncertainties are somewhat larger than those obtained for the t-butyl iodide and t-butyl hydrogen peroxide because of the scatter in the parent ion abundance at low energies. However, we can reduce the uncertainty in the derived onset energy by treating the three experiments as independent. We obtain a weighted average value and uncertainty using equations 6.4a and 6.4b.[21]

$$\bar{x} = \frac{\sum_i x_i \sigma_i^{-2}}{\sum_i \sigma_i^{-2}} \qquad\qquad\qquad \text{(6.4a)}$$

$$\bar{\sigma} = \left(\sum_i \sigma_i^{-2}\right)^{\frac{1}{2}} \qquad\qquad\qquad \text{(6.4b)}$$

where x_i represents the experimental onset energy and σ_i is the uncertainty in that value.

The average value of 10.397 ± 0.010 eV, shown in Table 6-1, agrees very nicely with the

0K value of 10.39 eV of Steiner et al.[7], but differs considerably from the Traeger value of

10.48 ± 0.010 eV.[8]

The heats of formation of both $C_4H_8^+$[22,23] and methane[24] co-products are well

known from which we can calculate the thermochemical dissociation threshold to be 9.91

eV, which is well below the observed onset of 10.397 eV. The methane-loss channel

must have a significant reverse barrier, a conclusion supported by DFT calculations

(Figure 6-4). It is evident from this figure why the methyl reaction, which is in

competition with the lower energy methane loss reaction, will not have a sharply defined

onset. At its energy threshold, the number of open channels via the methane loss reaction

will be huge so that the methyl loss signal is negligibly small. Its threshold energy thus

requires fitting the breakdown diagram with eq. 6.3 for which we need to know the sum

of states for both channels. Although we do not have experimental information about the

absolute rates, we can calculate the methane loss reaction rate constant using RRKM

theory[25] if the transition state for this reaction can be established. The geometry of the

transition state at the top of this barrier was found using the STQN method at the

B3LYP/6-311++G(d,p) level. The vibrational frequencies for this tight transition state

were thus used to calculate $N^{\ddagger}(E)$ for the CH_4 loss reaction. It is possible for tunneling to

contribute significantly to the dissociation rate, including at higher energies where

887 kJ •mol⁻¹

870 kJ •mol⁻¹

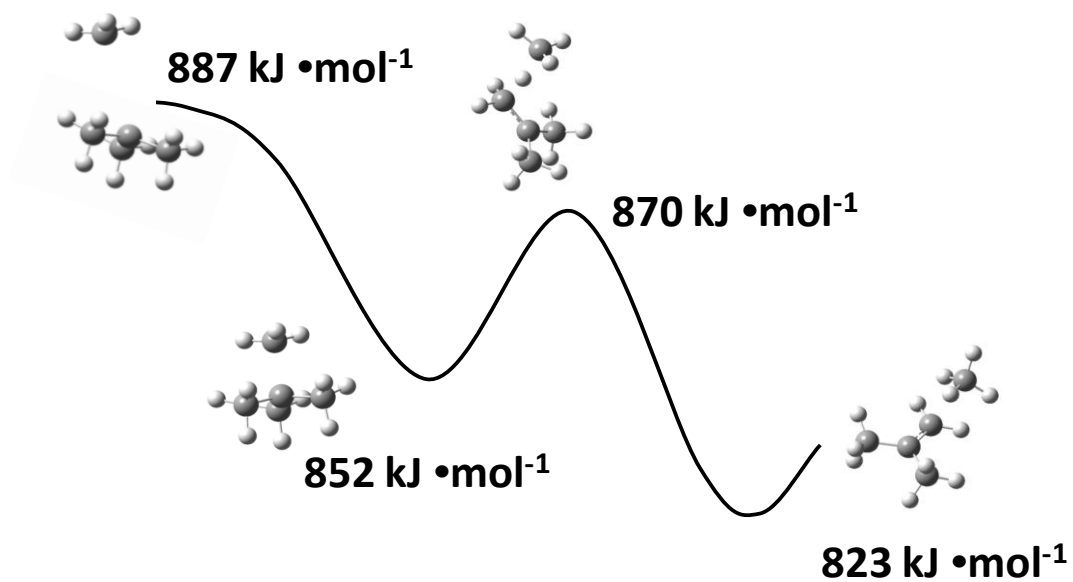**852 kJ •mol⁻¹**

823 kJ •mol⁻¹

Figure 6-4. Experimental energies and calculated structures of neopentane ion dissociation.

accurately modeling the $C_4H_8^+$ rate is critical to determining the $C_4H_9^+$ rate. We attempted to model the methane-loss channel including tunneling through an Eckart barrier treating critical frequency as an optimizable parameter,[25] however no acceptable fit to the data could be found except at conditions where the tunneling contribution was negligible. The calculated rate curve ignoring tunneling and using the calculated transition state frequencies appears in Figure 6-5. To account for uncertainty in the calculated frequencies, rate curves were calculated with the transition state frequencies scaled by 0.8 and 1.2 when determining the upper and lower limits of uncertainty in $E_0(t$-$C_4H_9^+)$.

With the methane loss reaction rate constant established, we can use the experimentally determined branching ratios to determine the methyl loss reaction rate using eqn. 6.3. In so doing, we must again take into account the full thermal energy distribution of the neopentane ion. The 0 K dissociation onset can then be obtained by extrapolating the methyl loss rate constant to its threshold energy. The formation of t-$C_4H_9^+$ occurs via homolytic bond cleavage without a barrier along its dissociation path. As a result, there is no fixed location and energy for the transition state that leads to t-$C_4H_9^+$. It has been shown[26,27] that the use of a fixed transition state with RRKM theory fails to accurately extrapolate to the E_0. More appropriate treatments are variational transition state theory[28,29] or the statistical adiabatic channel model,[25] however both require arduous calculation and ultimately, for larger molecules, require some sort of fitting parameter. An alternative is the simplified statistical adiabatic channel model (SSACM) which has recently been shown[26,27] to accurately model the specific rate curves of several barrierless ionic dissociations. Details of the model may be found
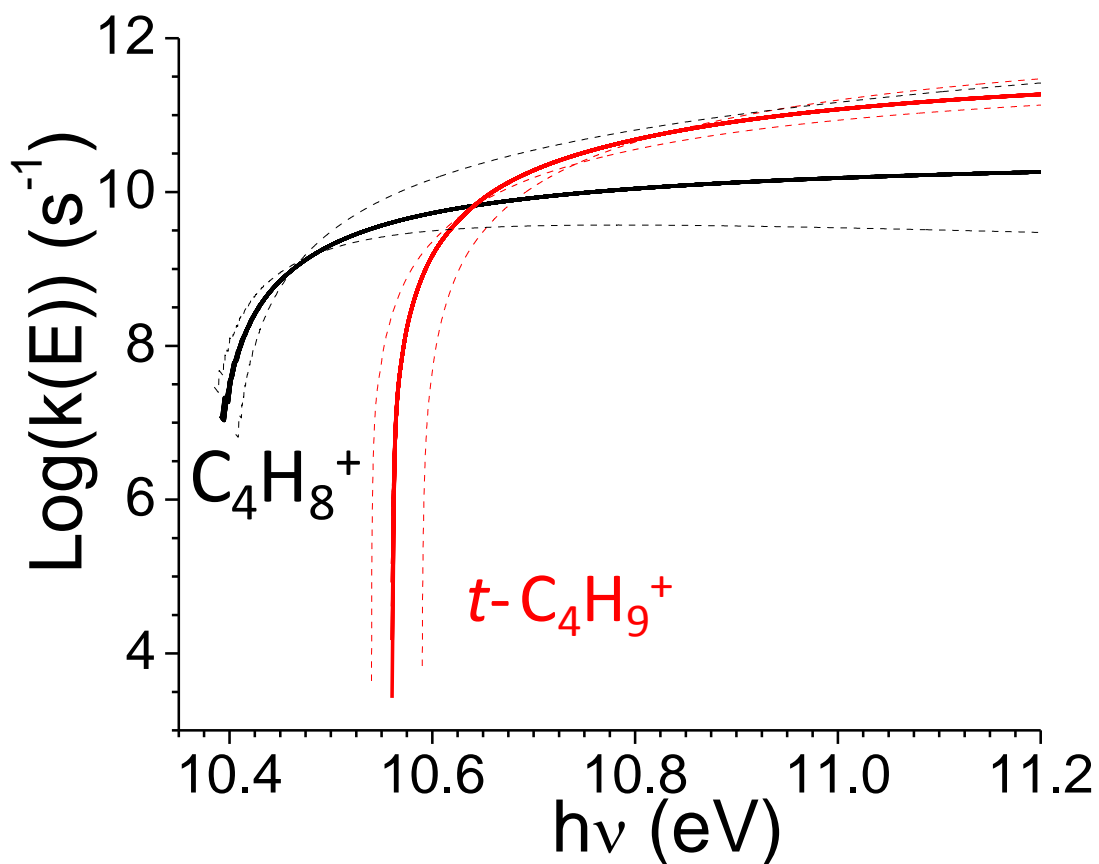
Figure 6-5 $k(E)$ for $C_4H_8^+$ and t-$C_4H_9^+$ formation from neopentane. The dotted lines represent the limits of uncertainty determined by fitting the experimental data. The transition state frequencies for $C_4H_8^+$ formation were scaled by 0.8 and 1.2.

elsewhere.[25] In brief, SSACM is a first-order correction to the orbiting transition state phase space theory, accounting for anisotropy along the reaction coordinate by scaling the number of states of the transitional modes by an energy dependent rigidity factor (f_{rigid}) and then convoluting this with the density of states of the rest of the molecule to get a total transition state sum of states.   Troe et al.[30] have suggested various forms for the rigidity factor including:

$$f_{rigid} = \left[1 + \left(\frac{E - E_0 + IE}{c}\right)\right]^{-\frac{2}{3}}$$

(6.5)

where c is a fitting parameter used to model the branching ratios. SSACM tends to underestimate dissociation rates at ion internal energies well above threshold;[19] the form of f_{rigid} used in (5) appears to mitigate this issue relative to other functional forms. Using the $N^{\ddagger}(E)$ defined by SSACM, the branching ratios can be calculated using eqn.6.3. $E_0(t\text{-}C_4H_9^+)$ and 'c' are varied to determine the best fit to the data.   To determine the overall uncertainty in the derived $E_0(t\text{-}C_4H_9^+)$, the temperature, E_{CH4}, and CH_4 loss transition state frequencies were all varied. The best fit E_0's for the three data sets were 10.560 ± 0.036 eV, 10.560 ± 0.043 eV, and 10.582 ± 0.059 eV, which, using equations 4a and 4b result in an average 0 K onset energy of 10.564± 0.025 eV. It is interesting that this value does not differ much from the previous determinations, in which the quoted error limits were smaller (see Table 6-1). However, the current value is much more trustworthy as it has been determined using the statistical theory with lower energy dissociation channels taken into account and error limits that reflect a more realistic uncertainty.

6.2.4   Derived t-C₄H₉⁺, t-C₄H₉I, and *t*-C₄H₉OOH heats of formation

The three 0 K onset energies for $t\text{-}C_4H_9^+$ formation from $t\text{-}C_4H_9I$, $t\text{-}C_4H_9OOH$, and $(CH_3)_4C$ can now be used in the thermochemical cycle below.

$$E_0\left(t\text{-}C_4H_9^+\right) = \Delta_f H_{0K}^o\left(t\text{-}C_4H_9^+\right) + \Delta_f H_{0K}^o(R) - \Delta_f H_{0K}^o\left(t\text{-}C_4H_9R\right)$$

$$(6.6)$$

The precision with which we can determine $\Delta_f H^o{}_{0K}(t\text{-}C_4H_9^+)$ using the neopentane cycle is better than the uncertainty in the heats of formation of $t\text{-}C_4H_9I$ and $t\text{-}C_4H_9OOH$. We will therefore use the $t\text{-}C_4H_9^+$ heat of formation determined from neopentane in the other 2 cycles to obtain better values for the *t*-butyl iodide and *t*-butyl hydroperoxide heats of formation.

The first task is to establish the 0 K heat of formation for neopentane. We must therefore determine $H_{298}\text{-}H_0$ for the constituents of the formation reaction. $H_{298}\text{-}H_0$ for the reactants, $C_{(s)}$ and $H_{2\,(g)}$, are reported by Chase.[24] Although the $H_{298}\text{-}H_0$ for neopentane is listed in the 1974 compilation of Scott[31] as 23.2 kJ/mol, there is no indication as to whether this is an experimental value or calculated on the basis of assumed vibrational frequencies. This is troubling because neopentane, as well as a number of other molecules in this study, has multiple methyl rotors, whose motion should be considered in terms of hindered rotors rather than vibrations. Karton et al.[16] recently reported a theoretical $H_{298}\,\text{-}H_0$ value corrected for internal rotations based on the method described by Ayala and Schlegel[32] which is 3 kJ/mol lower than the Scott value. This discrepancy must be primarily due to the assumed vibrational frequencies of neopentane because the hindered rotor correction is only 0.5 kJ/mol. The average deviation of the $H_{298}\text{-}H_0$

calculated by Karton *et al* from those reported by Scott for the other 16 linear and branched isomers of alkanes containing 4-8 carbon atoms was 0.25 kJ •mol^{-1}. Because we have no way of knowing on what basis the Scott conversion for neopentane was reported, and because other calculations in the same study by Karton *et al*. were shown to be quite reliable, we choose to adopt the theoretical $H_{298} - H_0$ value. The $\Delta_f H^o{}_{0K}((CH_3)_4C)$ is therefore -132.2 ± 0.8 kJ •mol^{-1}.

These 0 K heats of formation can now be used in Eqn. 6.6 to determine a $\Delta_f H^o{}_{0K}[t\text{-}C_4H_9{}^+]$ of 737.1 ± 2.5 kJ•mol^{-1}. Converting this value to 298 K requires the calculation of $H_{298} - H_0$ for the t-butyl ion, which we did using the same method as described by Karton *et al*., which yielded a 298 K value of 714.3 ± 2.5 kJ•mol^{-1}. We used the stationary electron convention in which the electron energy is 0 regardless of temperature. This t-butyl ion heat of formation is somewhat higher than the 1993 PEPICO study of t-butyl iodide,[10] which reported the generally accepted value for $\Delta_f H^o{}_{298K}(t\text{-}C_4H_9{}^+)$ of 711 ± 3.6 kJ•mol^{-1}. The new t-C$_4$H$_9{}^+$ heat of formation with realistic error limits, and which is firmly based on neopentane as an anchor, can now be employed to obtain the heats of formation of the t-butyl iodide and t-butyl hydroperoxide, which are listed in Table 6-2. The t-butyl iodide value of -68.5 ± 2.6 kJ•mol^{-1} is considerably lower than the Pedley value of -72.1 ± 3.3 kJ•mol^{-1}, although it falls within the combined error limits The heat of formation for the t-butyl hydroperoxide of -233.2 ± 2.5 kJ•mol^{-1} complements a 1964 heat of combustion measurement by Kozlov and Rabinovich[33] of -246. ± 5.0 kJ•mol^{-1}. The NIST Chemistry WebBook[34] lists a second value of -234.9 kJ•mol^{-1} with no error limits quoted by Khursan and Marten'yanov.[35] This value is taken from a compilation in preprint form by Komissarov, whose book we cannot find.

A new and preliminary value for IE_{ad} (t-C_4H_9) of 6.77 ±0.02 eV has been determined by Fischer et al[3] from a threshold photoelectron spectrum using supersonically cooled t-butyl radicals formed from the pyrolysis of di-$tert$-butyldiazine seeded in argon. This value is significantly higher than previous values (6.58[1] and 6.70 eV[2]), indicating perhaps that the radicals are colder than in the other experiments. However, when our new t-$C_4H_9^+$ heat of formation is combined with the accepted value for the radical $\Delta_f H^o_{298K}$(t-C_4H_9) of 51.5 ± 1.3 kJ•mol^{-1},[36] we predict an adiabatic IE of 6.87 ± 0.02 eV, which is a 0.10 eV (10 kJ/mol) higher still. What is clearly required is a vibrationally resolved PES of the t-butyl radical.

Table 6-2 Derived and Ancillary Thermochemical values. (kJ•mol^{-1})

	$\Delta_f H^o_{298K}$	$\Delta_f H^o_{0K}$	H_{298}-H_0
(CH$_3$)$_4$C	-168.0 ± 0.8[a]	-132.2 ± 0.8	20.3
	-166.0[b]		
t-C$_4$H$_9$I	-68.5 ± 2.8[c]	-40.5 ± 2.6	20.9
t-C$_4$H$_9$OOH	-233.2 ± 2.8[c]	-203.3 ± 2.8	24.3
t-C$_4$H$_9^+$	714.3 ± 2.5[c,f]	737.1 ± 2.5	19.0
OOH		15.2 ± 0.3[d]	
CH$_3$		149.9[d]	
I		107.2[d]	
H$^+$	1530.0[e,f]		
i-C$_4$H$_8$	-16.9 ± 0.9[d]		
$PA(i$-C$_4$H$_8^+)$	798.8 ± 2.5		

[a] Good, W. D. 1970;[15] [b]Karton, Gruzman, and Martin, 2009;[16] [c]These values were obtained in the current study; [d] Pedle 1994;[37] [e]Chase 1998[24]; [f]Obtained using the convention that excludes the enthalpy of the electron at room temperature.

6.3 Isodesmic Calculations of the t-C$_4$H$_9^+$ heat of formation

In support of the experimentally derived t-C$_4$H$_9^+$ heat of formation, we calculated the

G3 and CBS-APNO energies for the following isodesmic reactions:
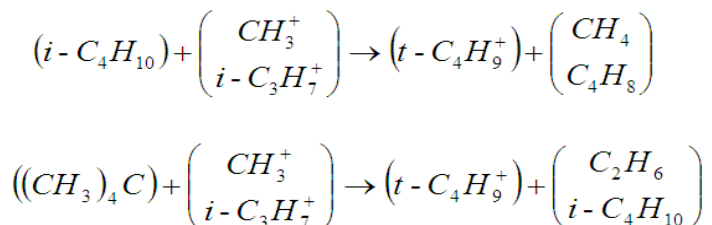
$$(i - C_4 H_{10}) + \begin{pmatrix} CH_3^+ \\ i - C_3 H_7^+ \end{pmatrix} \rightarrow (t - C_4 H_9^+) + \begin{pmatrix} CH_4 \\ C_4 H_8 \end{pmatrix}$$

$$((CH_3)_4 C) + \begin{pmatrix} CH_3^+ \\ i - C_3 H_7^+ \end{pmatrix} \rightarrow (t - C_4 H_9^+) + \begin{pmatrix} C_2 H_6 \\ i - C_4 H_{10} \end{pmatrix}$$

The t-C$_4$H$_9^+$ heat of formation is determined from the calculated reaction energy

and the experimental heats of formation for the other reaction constituents. The methane

heat of formation[38] and the corresponding $E_0(CH_4 \rightarrow CH_3^+ + H)$[39] are very well known

and provide a value of 1099.37 ± 0.1 kJ•mol^{-1} for $\Delta_f H°_{0K}(CH_3^+)$. Using $\Delta_f H°_{0K}(i$-

C$_3$H$_7$Cl)[37] and a recently measured photoionization onset for the isopropyl ion from i-

C$_3$H$_7$Cl of 11.065 ± 0.003 eV,[40] which is very close to a calculated value reported by

Brooks et al. of 11.061 eV,[41] the $\Delta_f H°_{0K}(i$-C$_3$H$_7^+)$ has been determined by us to be 824.1 ±

1.3 kJ•mol^{-1} . The heats of formation of the neutral hydrocarbons are all reported by

Pedley[37] to within 1 kJ•mol^{-1}.

Table 6-3shows the $\Delta_f H°_{0K}(t$-C$_4$H$_9^+)$ determined by calculations of the above

isodesmic reaction energies. The scatter in the G3 values is somewhat high, however the

average of 738.7 kJ•mol^{-1} is in excellent agreement with the experimental value of 737.1

± 2.5 kJ•mol^{-1}.   The higher level CBS-APNO method provides results that exhibit less

scatter and whose average value of 736.2 kJ/mol agrees equally with the experimental

value. When we take the average of the G3 and CBS-APNO values, we obtain *a*

$\Delta_fH^o{}_{0K}$(t-C$_4$H$_9$$^+$) = 737.5 kJ/mol. These calculated results thus provide strong support of the new experimental t-butyl ion heat of formation.

Table 6-3 $\Delta_fH^o{}_{0K}(t$-C$_4$H$_9$$^+)$ determined from *ab initio* isodesmic reaction energies. (kJ•mol^{-1})

		t-C$_4$H$_9$-**X** + **Y**$^+$ →t-C$_4$H$_9$$^+$ + **XY**			
	Y=	CH$_3$-G3	i-C$_3$H$_7$-G3	CH$_3$-CBS-APNO	i-C$_3$H$_7$-CBS-APNO
X=	H	740.0	735.8	736.6	734.8
	CH$_3$	741.5	737.6	737.4	736.1

6.4   Proton Affinity of isobutene

The proton affinity of isobutene and its use as an anchor for the proton affinity scale has played an important role in the history of the t-C$_4$H$_9$$^+$ heat of formation. Using the currently reported value of the $\Delta_fH^o{}_{298K}(t$-C$_4$H$_9$$^+)$ provides a value for $PA_{298K}(C_4H_8)$ of 798.8 ± 2.5 kJ•mol^{-1} This value is outside of the uncertainty of the previously accepted value of 801.7± 1.4 kJ•mol^{-1}.[8] However, it is probable that these uncertainties were significantly underestimated.

6.5   Conclusion

$\Delta_fH^o{}_{298K}(t$-C$_4$H$_9$$^+)$ has been determined to be 714.3 ± 2.5 kJ•mol^{-1} from measurement of the $E_0(t$-C$_4$H$_9$$^+)$ by modeling TPEPICO breakdown diagrams of neopentane at 220 K, 260 K, and 300 K. The higher than previously reported uncertainty reflects the true uncertainty in the value rather than sensitivity of fit as reported in PIMS measurements. Breakdown diagrams were also modeled for t-butyl iodide and t-butyl hydroperoxide and the $E_0(t$-C$_4$H$_9$$^+)$ was determined for both species. Using the currently determined value for $\Delta_fH^o{}_{298K}(t$-C$_4$H$_9$$^+)$, $\Delta_fH^o{}_{298K}(t$-C$_4$H$_9$I) and $\Delta_fH^o{}_{298K}(t$-C$_4$H$_9$OOH) were determined to be -68.5 ± 2.6 kJ•mol^{-1} and -233.2 ± 2.8 kJ•mol^{-1}, respectively. A

new proton affinity of isobutene is 798.8 ± 2.5 kJ•mol^{-1} . These new results do not remove the discrepancy between the well established t-C$_4$H$_9$$^\bullet$ radical heat of formation and its ionization energy. Two PES and one TPES measurement of this radical yield adiabatic IE's that are about 0.1 eV below the predicted value. This problem will probably not be resolved until a vibrationally resolved photoelectron spectrum is collected.

Reference List

1. Dyke, J.; Jonathan, N.; Lee, E.; Morris, A.; Winter, M. Vacuum Ultraviolet Photoelectron Spectroscopy of Transient Species: Part 8, the t-Butyl Radical, *Phys. Scr.* **1977,** *16* , 197-201.

2. Houle, F. A.; Beauchamp, J. L. Photoelectron spectroscopy of methyl, ethyl, isopropyl and tert-butyl radicals. Implications for the thermochemistry and structure of the radicals and their corresponding carbonium ions, *J. Am. Chem. Soc.* **1979,** *101* , 4067-4074.

3. Fischer, I. and Hemberger, P., University of Würzburg, TPES of supersonically cooled t-butyl radical using synchrotron radiation, Personal Communcation, 2009.

4. Smith, B. J.; Radom, L. Heat of formation of the tert-butyl radical 27, *J. Phys. Chem. A* **1998,** *102* , 10787-10790.

5. Karton, A.; Rabinovich, E.; Martin, J. M. L.; Ruscic, B. W4 theory for computational thermochemistry: In pursuit of confident sub-kJ/mol predictions, *J. Chem. Phys.* **2006,** *125* , 144108-1-144108/17.

6. Tajti, A.; Szalay, P. G.; Csaszar, A. G.; Kallay, M.; Gauss, J.; Valeev, E. F.; Flowers, B. A.; Vazquez, J.; Stanton, J. F. HEAT: high accuracy extrapolated ab initio thermochemistry, *J. Chem. Phys.* **2004,** *121* , 11599-11613.

7. Steiner, B. W.; Giese, C. F.; Inghram, M. G. Photoionization of alkanes. Dissociation of excited molecular ions, *J. Chem. Phys.* **1961,** *34* , 189-220.

8. Traeger, J. C. The absolute proton affinity for isobutene, *Rapid Comm. Mass. Spectr.* **1996,** *10* , 119-122.

9. Oliveira, M. C.; Baer, T.; Olesik, S.; Almoster Ferreira, M. A. The Dissociation energies and mechanism of energy selected bromo and iodo butanes, *Int. J. Mass Spectrom. Ion. Proc.* **1988,** *82* , 299-318.

10. Keister, J. W.; Riley, J. S.; Baer, T. The t-butyl ion heat of formation and the isobutene proton affinity, *J. Am. Chem. Soc.* **1993,** *115* , 12613-12614.

11. Park, S. T.; Kim, S. K.; Kim, M. S. Vacuum-ultraviolet mass analyzed threshold ionization spectra of iodobutane isomers: Conformer-specific ionization and ion-core dissociation followed by ionization, *J. Chem. Phys.* **2001,** *115* , 2492-2498.

12. McLoughlin, R. G.; Traeger, J. C. Heat of formation for tert-butyl cation in the gas phase, *J. Am. Chem. Soc.* **1979,** *101* , 5791-5792.

13. Lias, S. G.; Bartmess, J. E.; Liebman, J. F.; Holmes, J. L.; Levin, R. D.; Mallard, W. G. Gas Phase Ion and Neutral Thermochemistry, *J. Phys. Chem. Ref. Data* **1988,** *17 suppl. 1*.

14. Smith, B. J.; Radom, L. Assigning absolute values to proton affinities: A differentiation between competing scales, *J. Am. Chem. Soc.* **1993,** *115* , 4885-4888.

15. Good, W. D. The enthalpies of combustion and formation of the isomeric pentanes, *J. Chem. Therm.* **1970,** *2* , 237-244.

16. Karton, A.; Gruzman, D.; Martin, J. M. L. Benchmark Thermochemistry of the CnH2n+2 Alkane Isomers (*n*) 2-8) and Performance of DFT and Composite Ab Initio Methods for Dispersion-Driven Isomeric Equilibria, *J. Phys. Chem. A* **2009,** *113* , 8434-8447.

17. Baer, T.; Sztáray, B.; Kercher, J. P.; Lago, A. F.; Bodi, A.; Scull, C.; Palathinkal, D. Threshold photoelectron photoion coincidence studies of parallel and sequential dissociation reactions, *Phys. Chem. Chem. Phys.* **2005,** *7* , 1507-1513.

18. Kercher, J. P.; Stevens, W.; Gengeliczki, Z.; Baer, T. Modeling Ionic Unimolecular Dissociations from a Temperature Controlled TPEPCIO Study on 1-C_4H_9I ions, *Int. J. Mass Spectrom.* **2007,** *267* , 159-166.

19. Shuman, N. S.; Spencer, A. P.; Baer, T. Experimental Thermochemistry of SiCl3R; (R = Cl, H, CH3, C2H5, C2H3, CH2Cl, SiCl3, SiCl3+, and SiCl3), *J. Phys. Chem. A* **2009,** *113* , 9458-9466.

20. Jonas, A. E.; Schweitzer, G. K.; Grimm, F. A.; Carlson, T. A. The photoelectron spectra of the tetrafluoro and tetramethyl compounds of the group IV elements, *J. Electron Spectrosc. Relat. Phenom.* **1972,** *1* , 29-66.

21. Bevington, P. R.; Robinson, D. K. *Data Reduction and Error Analysis for the Physical Sciences;* McGraw Hill: Boston, 2003.

22. Traeger, J. C. Heat of formation for the 1-methylallyl cation by photoionization mass spectrometry, *J. Phys. Chem.* **1986,** *90* , 4114-4118.

23. Prosen, E. J.; Maron, F. W.; Rossini, F. D. *J. Res. NBS* **1951,** *46* , 106-112.

24. Chase, M. W. *NIST-JANAF Thermochemical Tables;* 4th ed.; American Institute of Physics: New York, 1998.

25. Baer, T.; Hase, W. L. *Unimolecular Reaction Dynamics: Theory and Experiments;* Oxford University Press: New York, 1996.

26. Stevens, W.; Sztáray, B.; Shuman, N.; Baer, T.; Troe, J. Specific Rate Constants k(E) of the Dissociation of the Halobenzene Ions: Analysis by Statistical Unimolecular Rate Theories, *J. Phys. Chem. A* **2009,** *113* , 573-582.

27. Troe, J.; Ushakov, V. G.; Viggiano, A. A. On the Model Dependence of Kinetic Shifts in Unimolecular Reactions: The Dissociation of the Cations of Benzene and n-Butylbenzene, *J. Phys. Chem. A* **2006,** *110* , 1491-1499.

28. Chesnavich, W. J. Multiple transition states in unimolecular reactions, *J. Chem. Phys.* **1986,** *84* , 2615-2619.

29. Hase, W. L. The criterion of minimum state density in unimolecular rate theory. An application to ethane dissociation, *J. Chem. Phys.* **1976,** *64* , 2442-2449.

30. Troe, J. Towards Simplified Thermal and Specific Rigidity Factors for Ion-Molecule Reactions and Ion Fragmentations, *Z. Phys. Chem.* **2009,** *223* , 347-357.

31. Scott, D. W. Chemical Thermodynamic Properties of Hydrocarbons and Related Substances. U.S. Bureau of Mines Bulletin No. 666; U.S. Government Printing Office: Washington, DC.,Available online at http://digicoll.manoa.hawaii.edu/techreports/PDF/USBM-666.pdf.

32. Ayala, P. Y.; Schlegel, H. B. Identification and treatment of internal rotation in normal mode vibrational analysis, *J. Chem. Phys.* **1998,** *108* , 2314-2325.

33. Kozlov, N. A.; Rabinovich, I. B. Thermodynamics of isopropylbenzene and tert-butyl hydroperoxides. I. Heat of combustion and the formation of hydroperoxides; energy of oxygen-oxygen bond, *Tr. Khim. Khim. Tekhnol.* **1964,** 189-193.

34. Lias, S. G.; Bartmess, J. E.; Liebman, J. F.; Holmes, J. L.; Levin, R. D.; Mallard, W. G. NIST Chemistry WebBook, NIST Standard Reference Database Number 69. Mallard, W. G., Linstrom, P. J., Eds.; National Institute of Standards and Technology: Gathersburg, MD, 2000. Available Online at webbook.nist.gov/chemistry

35. Khursan, S. L.; Martem'yanov, V. S. Thermochemistry of the recombination of peroxyl radicals, *Russ. J. Phys. Chem. (Engl. Transl.)* **1991,** *65* , 321-325.

36. Blanksby, S. J.; Ellison, G. B. Bond Dissociation Energies of Organic Molecules, *Acc. Chem. Res.* **2003,** *36* , 255-263.

37. Pedley, J. B. *Thermochemical Data and Structures of Organic Compounds;* Thermodynamics Research Center: College Station, 1994.

38. Ruscic, B.; Pinzon, R. E.; Morton, M. L.; Laszevski, G.; Bittner, S. J.; Nijsure, S. G.; Amin, K. A.; Minkoff, M.; Wagner, A. F. Introduction to Active Thermochemical Tables: Several "Key" Enthalpies of Formation Revisited, *J. Phys. Chem. A* **2004,** *108* , 9979-9997.

39. Weitzel, K. M.; Malow, M.; Jarvis, G. K.; Baer, T.; Song, Y.; Ng, C. Y. High-resolution pulsed field ionization photoelectron photoion coincidence study of CH_4: Accurate 0 K dissociation threshold for CH_3^+, *J. Chem. Phys.* **1999,** *111* , 8267-8270.

40. Stevens, W. R.; Bodi, A.; Baer, T. iPEPICO Determination of the Heat of Formation of the Isopropyl Cation, *in preparation* **2009**.

41. Brooks, A.; Lau, K.-C.; Ng, C. Y.; Baer, T. The $C(3)H(7)(+)$ appearance energy from 2-iodopropane and 2-chloropropane studied by threshold photoelectron photoion coincidence, *Eur. J. Mass Spectrom.* **2004,** *10* , 819-828.

CHAPTER 7: Conclusions

The work described in this dissertation deals with the dissociation energetics and dynamics of three types of ionic reactions, which include a case of a fast dissociation, two systems in which the dissociation rates are slow compared to the experimental time scale, and one case where competing dissociation paths required the use of detailed modeling of the reaction rates. The data for the fast dissociation of halogen loss from 2-propyl halide ions was one of the first experimental data sets determined at the new iPEPICO end station at the VUV beamline of the Swiss Light Source (SLS). These results have resolved a long standing conflict in the literature concerning the dissociative photoionization onsets. The slow dissociation of halobenzene ions were used to test various unimolecular dissociation rate theories. This required careful measurement of reaction rates over a range of 4-5 order of magnitude. A special effort was made to extend this range to very slow rates, to about 3×10^2 s^{-1}. These results have shown clearly that flexible transition state models such as VTST and SACM are required to reliably model the rates of homolytic bond cleavages. In chapter 5, SSACM was used to

extrapolate to the E_0 for the formation of phenyl ions from nitrosobenzene.   The E_0 was then used to determine more precise values for the ionization energy of the phenyl radical and the heat of formation of nitrosobenzene.   In chapter 6, RRKM wasappropriate for the CH_4 loss which occurs via rearrangement and SSACM was used for the homolytic CH_3 loss. The bond energy for CH_3 loss was then used to determine the heat of formation of the t-butyl ion which is used to anchor the gas phase proton affinity scale.

A different form of the rigidity factor was used in chapter 6 from the one in chapters 4 and 5. Both forms of the rigidity factor as well as a third have been previously reported in the literature by Troe.[1] The functional form is chosen based on which one best describes the data. Because the rigidity factor has little to no effect at low internal energies, changing the functional form of the rigidity factor results in a similar value for the extrapolated E_0 but with a larger uncertainty and worse fit to the data. However, a significant improvement to this model would be an *a priori* method of determining the most appropriate functional form of the rigidity factor.

Reference List

1. Troe, J. Towards Simplified Thermal and Specific Rigidity Factors for Ion-Molecule

Reactions and Ion Fragmentations, *Z. Phys. Chem.* **2009,** *223* , 347-357.